

Stirling Engines for Low-Temperature Solar-Thermal-Electric Power Generation

Artin Der Minassians



Electrical Engineering and Computer Sciences
University of California at Berkeley

Technical Report No. UCB/EECS-2007-172

<http://www.eecs.berkeley.edu/Pubs/TechRpts/2007/EECS-2007-172.html>

December 20, 2007

Copyright © 2007, by the author(s).
All rights reserved.

Permission to make digital or hard copies of all or part of this work for personal or classroom use is granted without fee provided that copies are not made or distributed for profit or commercial advantage and that copies bear this notice and the full citation on the first page. To copy otherwise, to republish, to post on servers or to redistribute to lists, requires prior specific permission.

Acknowledgement

This work was supported by University of California Energy Institute (UCEI) and National Science Foundation (NSF)

**Stirling Engines for Low-Temperature
Solar-Thermal-Electric Power Generation**

by

Artin Der Minassians

Karshenasi (Amirkabir University of Technology) 1996
Karshenasi Arshad (Amirkabir University of Technology) 1998

A dissertation submitted in partial satisfaction of the
requirements for the degree of
Doctor of Philosophy

in

Engineering - Electrical Engineering and Computer Sciences

in the

GRADUATE DIVISION
of the
UNIVERSITY OF CALIFORNIA, BERKELEY

Committee in charge:
Professor Seth R. Sanders, Chair
Professor Robert W. Dibble
Professor Roland Winston
Professor Albert P. Pisano

Fall 2007

The dissertation of Artin Der Minassians is approved:

_____	_____
Chair	Date
_____	_____
	Date
_____	_____
	Date
_____	_____
	Date

University of California, Berkeley

Fall 2007

**Stirling Engines for Low-Temperature
Solar-Thermal-Electric Power Generation**

Copyright © 2007

by

Artin Der Minassians

Abstract

Stirling Engines for Low-Temperature
Solar-Thermal-Electric Power Generation

by

Artin Der Minassians

Doctor of Philosophy in Engineering - Electrical Engineering and Computer Sciences

University of California, Berkeley

Professor Seth R. Sanders, Chair

This dissertation discusses the design and development of a distributed solar-thermal-electric power generation system that combines solar-thermal technology with a moderate-temperature Stirling engine to generate electricity. The conceived system incorporates low-cost materials and utilizes simple manufacturing processes. This technology is expected to achieve manufacturing cost of less than \$1/W. Since solar-thermal technology is mature, the analysis, design, and experimental assessment of moderate-temperature Stirling engines is the main focus of this thesis.

The design, fabrication, and test of a single-phase free-piston Stirling engine prototype is discussed. This low-power prototype is designed and fabricated as a test rig to provide a clear understanding of the Stirling cycle operation, to identify the key components and the major causes of irreversibility, and to verify corresponding theoretical models. As a component, the design of a very low-loss resonant displacer piston subsystem is discussed.

The displacer piston is part of a magnetic circuit that provides both a required stiffness and actuation forces. The stiffness is provided by a magnetic spring, which incorporates an array of permanent magnets and has a very linear stiffness characteristic that facilitates the frequency tuning. In this prototype, the power piston is not mechanically linked to the displacer piston and forms a mass-spring resonating subsystem with the engine chamber gas spring and has resonant frequency matched to that of the displacer. The fabricated engine prototype is successfully tested and the experimental results are presented and discussed. Extensive experimentation on individual component subsystems confirms the theoretical models and design considerations, providing a sound basis for higher power Stirling engine designs for residential or commercial deployments.

Multi-phase Stirling engine systems are also considered and analyzed. The modal analysis of these machines proves their self-starting potential. The start-up temperature, i.e., the heater temperature at which the system starts its operation, is derived based on the same modal analysis. Following the mathematical modeling, the design, fabrication, and test of a symmetric three-phase free-piston Stirling engine system are discussed. The system is designed to operate with moderate-temperature heat input that is consistent with solar-thermal collectors. Diaphragm pistons and nylon flexures are considered for this prototype to eliminate surface friction and provide appropriate seals. The experimental results are presented and compared with design calculations. Experimental assessments confirm the models for flow friction and gas spring hysteresis dissipation. It is revealed that gas spring hysteresis loss is an important dissipation phenomenon in low-power low-pressure Stirling engines, and should be carefully addressed during the design as it may hinder the engine operation. Further analysis shows that the gas hysteresis dissipation

can be reduced drastically by increasing the number of phases in a system with a little compromise on the operating frequency and, hence, the output power. It is further shown that for an even number of phases, half of the pistons could be eliminated by utilizing a reverser. By introducing a reverser to the fabricated system, the system proves its self-starting capability in engine mode and validates the derived expressions for computing the start-up temperature.

Professor Seth R. Sanders
Dissertation Committee Chair

*To my mother, Clara,
for teaching me the power of love, the significance of kindness, the
importance of education, and the value of hard work.*

*To the memory of my father, Sarkis,
with love and gratitude.*

*To my brother, Martin,
for being the perfect example of an in-depth engineer who has an
unquenchable thirst for learning.*

Contents

List of Figures	v
List of Tables	viii
Acknowledgments	x
1 Introduction	1
1.1 Photovoltaics	2
1.2 Thin-Film Photovoltaics	4
1.3 Concentrated Photovoltaics	7
1.4 Residential Water Heating	8
1.5 Solar Parabolic Trough	11
1.6 Solar Power Tower	14
1.7 Solar Dish-Engine Systems	16
1.8 Thesis Contribution and Structure	19
2 Low-Cost Solar-Thermal-Electric Power Generation	21
2.1 Introduction	21
2.2 System Topology	22
2.2.1 Market Available Collectors	23
2.2.2 Stirling Engines	24
2.3 System Efficiency	29
2.4 System Cost Analysis	30
2.5 Conclusions	32
3 Stirling Cycle and Non-Idealities	33
3.1 Introduction	33
3.2 Heat Exchangers	34
3.2.1 Fluid Flow Dissipation	34
3.2.2 Heat Transfer	41
3.2.3 Regenerator Effectiveness	44
3.3 Gas Spring Hysteresis	47
3.4 Clearance Seal Leakage	49
3.5 Conduction Loss	50
3.6 Conclusions	51

4	Single-Phase Stirling Engine Prototype	53
4.1	Introduction	53
4.2	Design and Thermodynamic Simulation	54
4.3	Design	56
4.3.1	Displacer Subsystem	56
4.3.2	Heat Exchangers	61
4.3.3	Power Piston	62
4.3.4	Electromagnetic Circuits	64
4.4	Experimental Assessment	68
4.4.1	Displacer Piston	68
4.4.2	Heat Exchangers	73
4.4.3	Power Piston	75
4.5	Engine Operation	77
4.6	Conclusions	82
5	Multi-Phase Stirling Engines	84
5.1	Introduction	84
5.2	Formulation	85
5.3	Linearization	88
5.4	Analysis	90
5.4.1	Symmetric Three-Phase System	91
5.5	Symmetric Three-Phase Stirling Prototype	97
5.5.1	Heat Exchangers	98
5.5.2	Diaphragm Pistons	100
5.5.3	Flexure	102
5.5.4	Actuator	103
5.6	Experimental Results	104
5.6.1	Fluid Flow Friction	105
5.6.2	Heat Pump Operation	107
5.6.3	Gas Spring Hysteresis	112
5.6.4	Engine Operation	114
5.7	Reverser Modeling and Analysis	116
5.8	Reverser Implementation	120
5.9	Conclusions	121
6	Conclusions	126
6.1	High Power Stirling Engine Design	128
6.2	Future Work	129
	Bibliography	132
A	Second Order Dynamical System	139
A.1	Dry Friction	139
A.2	Viscous Friction	142
B	Gas Spring Stiffness	145

C Symmetric Six-Phase Stirling System	147
D Technical Drawings for the Single-Phase Stirling Engine Prototype	151
E Technical Drawings for the Three-Phase Stirling Engine Prototype	168

List of Figures

1.1	Valence and conduction band positioning for (a) Direct band gap and (b) Indirect band gap materials.	4
1.2	Absorber plate of a typical flat-plate solar collector.	8
1.3	(a) Close-up view of an evacuated-tube collector. (b) A typical evacuated-tube collector system for residential water heating. Courtesy of Beyond Oil Solar.	9
1.4	CPC operation under different sunlight conditions: direct, dispersed, and skewed.	10
1.5	typical efficiency comparison of CPC and flat-plate collectors for 1000 W/m ² solar insolation. Courtesy of Prof. Roland Winston.	11
1.6	A solar trough plant in California (SEGS). Image courtesy of DOE.	12
1.7	Solar Two plant in Mojave Desert, California. Image courtesy of NREL.	15
1.8	Solar Dish-Stirling system. Image courtesy of Stirling Energy Systems (SES).	17
2.1	Schematic diagram of the solar-thermal-electric power generation system.	22
2.2	Stirling cycle p - V loop.	26
2.3	Three common mechanical configurations of Stirling engines: (a) Alpha, (b) Beta, and (c) Gamma. Images courtesy of Koichi Hirata.	27
2.4	Efficiency as a function of temperature for a representative system. The parameters used are $G = 1000$ W/m ² , $\eta_0 = 77.3\%$, $U_1 = 1.09$ W/m ² K, $U_2 = 0.0094$ W/m ² K ² , $T_{amb} = 27$ °C, $T_{cold} = 27$ °C, and $\epsilon_{Carnot} = 66\%$. The dot indicates the point of optimal system efficiency.	28
3.1	Nonlinear resistor model for fluid flow through heat exchangers.	35
3.2	Regenerator temperature profile with respect to the working fluid temperatures.	45
3.3	Energy balance diagram for a Stirling engine.	52
4.1	Complete assembly drawing of the single-phase free-piston Stirling engine design.	54
4.2	Simplified schematic diagram of the conceived Stirling engine.	55
4.3	Simulation results of the single-phase free-piston Stirling engine thermodynamic behavior. (a) Wall, instantaneous, and average temperatures on hot and cold sides. (b) Expansion space, compression space, and total engine chamber volume variations. (c) Pressure variation. (d) p - V loop of the thermodynamic cycle.	57
4.4	Schematic diagram of the displacer piston design.	58
4.5	(a) Fabricated displacer piston with embedded linear motion ball bearing and permanent magnet arrays. (b) Stationary magnetic array that provides the linear spring function for the displacer. Compare to Figure 4.4	59

4.6	FEM analysis result for the stiffness characteristic of the magnetic spring. The straight line represents a linear regression fit through the data points (circles).	60
4.7	Fabricated heat exchanger shown with the etched fins and copper tube inserts.	62
4.8	Fabricated power piston shown with the low carbon steel body and Nd-Fe-B permanent magnets attached to one end.	64
4.9	Simulated and measured waveforms of the displacer actuator EMF with no separation between the two windings. Refer to Figure 4.4	67
4.10	Simulated and measured waveforms of the displacer actuator EMF with the optimal separation (2 in.) between the two windings.	68
4.11	Ring-down characteristic of the displacer piston.	69
4.12	Equivalent electric circuit schematic and phasor diagram for the displacer energy balance experiment.	71
4.13	(a) Input voltage waveform (b) Input current waveform (c) Input voltage harmonic components (d) Input current harmonic components.	72
4.14	Ring-down characteristic of the displacer piston in the presence of the heater, cooler, regenerator, and the connecting pipes and fittings. Compare with Figure 4.11.	73
4.15	Ring-down characteristic of power piston while separated from the rest of the engine.	75
4.16	Gas hysteresis loss characteristic of the fabricated Stirling engine prototype.	77
4.17	The Stirling engine experimental setup.	78
4.18	Measured engine pressure and volume variations. Compare to Figure 4.3.	79
4.19	Measured p - V diagram of the engine.	80
5.1	Schematic diagram of a multi-phase Stirling engine system.	86
5.2	Simulated piston positions of the symmetric three-phase system. (a) Startup (b) Steady state.	88
5.3	Mass-spring equivalent of the multi-phase Stirling engine system in Figure 5.1. K_G represents the gas spring stiffness.	92
5.4	Relationship between a complex numbers, μ_1 , λ_1 , and λ'_1	93
5.5	Approximated effect of system dissipation on the eigenvalues. Compare to Figure 5.4.	96
5.6	Simulation of the symmetric three-phase Stirling engine system under asymmetric electric loading condition. All three engines maintain their internal viscous and gas spring hysteresis dissipations and an external third-order load is applied to one of the phases only (shown with solid line).	99
5.7	Fabricated heat exchanger frame and the screens.	100
5.8	(a) Liquid rubber is cast in printed wax molds to fabricate the diaphragms. (b) Top wax mold and corrugated diaphragm after being separated from the molds.	101
5.9	Close-up view of the fabricated diaphragm with one ring of corrugation.	102
5.10	Fabricated magnetic actuator (control circuitry not shown).	103
5.11	Fabricated three-phase Stirling engine system. Photograph taken before custom corrugated silicone diaphragms were fabricated and installed.	104
5.12	Ring-down characteristic of the nylon flexure.	106
5.13	Electric circuit analogue for the thermal model of the prototype while operating as heat pump.	108

5.14	Temperature variation of the hot and cold sides of one Stirling engine during the heat pump regime.	111
5.15	Gas spring hysteresis loss versus fractional volumetric variation. The graph is a quadratic regression through the measured points (shown in dots) taken from Table 5.6.	113
5.16	Progression of the eigenvalues of the symmetric three-phase Stirling engine system toward the unstable region as the hot side temperature increases. At $T_h = 175$ °C the system becomes self-starting.	115
5.17	Phasor diagram for three examples of multi-phase Stirling engine systems with four, six, and eight phases. Each vector represents position of one piston. Dashed vectors are representative of the pistons that can be eliminated by utilizing a reverser.	116
5.18	Schematic diagram of a multi-phase Stirling engine system that incorporates a reversing mechanism within piston r	118
5.19	Progression of the eigenvalues of three-phase Stirling engine with reverser toward the unstable region as the hot side temperature increases. At $T_h = 79$ °C the system becomes self-starting.	120
5.20	Simulated piston positions of the three-phase system with reverser. (a) Startup (b) Steady state.	121
5.21	Implementation of reverser mechanism within the fabricated three-phase Stirling engine prototype.	122
5.22	Recorded acceleration signals of the three phases in the revised three-phase Stirling engine system.	124
5.23	Fundamental frequency components of the three acceleration signals. Compare to Figure 5.20(b).	125
5.24	Acceleration signal of one piston at full-amplitude ascillation.	125
6.1	Energy balance diagram for the high-power Stirling engine. Compare to Figure 3.3.	129
A.1	Ring-down phase portrait of a second order mass-spring system with dry friction. For the simulated system, $m = 1$ kg, $K = 1$ kN/m, and $F_f = 50$ N.	141
A.2	Time-domain position for the ring-down of a second order mass-spring system with dry friction. For the simulated system, $m = 1$ kg, $K = 10$ kN/m, and $F_f = 50$ N.	142
A.3	Time-domain position for the ring-down of a second order mass-spring system with viscous friction. For the simulated system, $m = 1$ kg, $K = 10$ kN/m, and $D = 6$ Ns/m.	143
C.1	Progression of the eigenvalues of six-phase Stirling engine toward the unstable region as the hot side temperature increases. At $T_h = 79$ °C the system becomes self-starting.	148
C.2	Simulated piston positions of the six-phase system. (a) Startup (b) Steady state.	150

List of Tables

1.1	Cost of concentrated solar-thermal-electric technologies.	19
2.1	Comparison of market available STCs. Assumptions: $G=1000 \text{ W/m}^2$, $\epsilon_{Carnot} = 66\%$, $T_{amb} = 27 \text{ }^\circ\text{C}$. System costs are computed assuming engine cost is zero. All costs are approximated by discounted retail price of 500 m^2 collector area. Parentheses indicate presumed values.	25
2.2	Materials cost breakdown of Thermo Dynamics G Series STC.	31
3.1	Comparison of the calculated and measured fluid flow dissipations for the heat exchangers and tubing of the two fabricated Stirling engine prototypes. Two measurement methodologies are implemented: ring-down (RD) and energy-balance (EB) tests. Dissipations are expressed in Watts.	40
3.2	Comparison of calculated heat transfer behavior for the heat exchangers of the two fabricated Stirling engine prototypes.	43
3.3	Comparison of measured and calculated gas hysteresis (compression) losses in various conditions. The number in the left three columns indicate the fraction of corresponding heat exchanger screens that is in place.	49
4.1	Engine thermodynamic design parameters.	56
4.2	Comparison of the calculated component dissipations with the measurement-based estimations.	74
4.3	Power balance for the fabricated prototype at the operating point discussed in this paper. \dagger indicates a directly measured parameter. All other parameters are calculated based on energy balance principle and the measured values.	82
5.1	Three examples of common dissipation and loading functions. Parameters D , F_f , and L_P are, respectively, viscous friction factor, dry friction force, and loading factor, and $\mathcal{S}(\cdot)$ is the sign function.	87
5.2	Prototype three-phase Stirling engine parameters. Volume multipliers indicate the porosity of each section.	98
5.3	As-cured physical properties of the silicone diaphragm material.	101

5.4	Summary of the ring-down tests carried out on the prototype. On each row the cross sign indicates which components were included in the test. F, D, K, H, R, and C refer to flexure, diaphragm, cooler, heater, regenerator, and C-core (actuator laminated steel core shown in Figure 5.10), respectively.	107
5.5	Comparison of the measured flow friction data with designed values for heater and regenerator.	107
5.6	Comparison of measured and calculated gas spring hysteresis (compression) losses in various conditions. The number in the left three columns indicate the fraction of corresponding heat exchanger screens that is in place.	112
6.1	Engine design parameters.	131

Acknowledgments

My first and foremost words of appreciation go to my esteemed research advisor, Professor Seth R. Sanders. Since the first day I shook hands with him in Cory Hall, I have continuously benefited from his terrific disposition, enormous source of knowledge, outstanding expertise in both theoretical and practical matters, unmatched availability, unsurmountable patience, and assiduous encouragement throughout the past several years. I am truly privileged to be blessed with such a rare opportunity to observe and, hopefully, learn his unique approach to analyzing problems, entertaining and structuring new ideas, developing viable solutions, and putting them into practice. I sincerely hope that he enjoyed our collaboration as much as I did.

I am highly honored, also, for having Professors Albert P. Pisano, Roland Winston, and Robert W. Dibble in my dissertation committee. I would like to express my sincere gratitude to them for patiently reviewing the contents of this thesis and for their detailed and constructive remarks.

I could have never made it this far without the help and guidance of my revered mentors at Amirkabir University of Technology. I truly enjoyed every moment of working with Professors S. H. H. Sadeghi, Sh. M. Kouhsari, G. B. Gharehpetian, and R. Moini Mazandaran on various challenging and extremely fun projects. In addition, Professor H.

A. Toliyat of Texas A&M University has been a stupendous source of support to me, even before I moved to the United States. I express my heartfelt gratitude for all they did.

Who does not know Ruth Gjerde in Cory Hall? She has this amazing power of making everything so simple and convenient for graduate students that is almost unbelievable in UC Berkeley's bureaucratic system! Along the same line, Rosita Alvarez-Croft and Mary Byrnes have always been welcoming with their soothing smiles and willingness to help in various capacities, which is greatly appreciated.

Outstanding individuals assisted me in this journey. Thanks to Konrad H. Aschenbach for being the first graduate student to join me in this project. He was a fantastic match to the challenge as he questioned every single statement that came out of my mouth! In fact, all his questions were right to the point and constructive. I sincerely appreciate the invaluable consultation and help of Erik Steltz, Hyuck Choo, and Robert Wood for fabrication of the wax molds and casting of the rubber diaphragms for my three-phase Stirling engine prototype. Alvin Tai brought an enormous amount of positive energy to our lab during his tenure. He was there with his skateboard whenever I needed his help. Mike He joined this project three semesters ago and helped with the electromagnetic simulations and experimentation. He is going to continue working on the engines to take them to the next level. I wish him much success in his endeavor. Allan Chen volunteered his time and resources to prepare the technical drawings for the fabricated prototypes. His work was beyond expectation. Also, as summer interns, Engdu Workneh and Dave Estrada contributed to the design and fabrication of the controller for the multi-phase inverter. Thanks to all...

I would like to acknowledge Ben Lake, Joseph Gavazza, and Warner Carlisle of the

ERSO Machine Shop who played a crucial role in the fabrication of the two Stirling engine prototypes discussed in this thesis.

I would also like to thank my wonderful colleagues in Professor Sanders' research group for their friendship over the years. Perry Tsao, Jinwen Xiao, Angel Peterchev, Matthew Senesky, Gabriel Eirea, Jianhui Zhang, Jason Stauth, Michael Seeman, Evan Reutzel, Vincent Ng, and Kun Wang, made 143, 341, and 550 Cory fun places to work.

My "Berkeley experience" was not limited to the EECS department, though. Since my arrival at Berkeley, I was heavily involved in musical activities at the music department, particularly as a member of the University Chorus and Chamber Chorus. Professor Marika Kuzma, the brilliant director of both ensembles, has been yet another influential character in my life. Her musical knowledge and capacity, interpretation, demand for precision, discipline, and kind heart placed her above all the musicians in the Bay Area. I enjoyed every moment of singing in her first-rate choirs and learning the secrets of choral conducting in her workshops. All I learnt from her will stay with me for the rest of my life.

Throughout the past several years, I have enjoyed the support and friendship of Dr. Mona Afary, Dr. Bahram Afshari, Mr. Amin Aminzadeh Gohari, Ms. Katrin Arefy, Dr. Arnaud Boissière, Dr. Saied Bozorgui-Nesbat, Dr. Armen Der Kiureghian, Dr. Shahin Farshchi, Ms. Kristen Hiestand, Mr. Mohammad Hooshmand, Dr. Amir Jafari, Ms. Tannaz Jafarian, Mr. Babak Jamshidi, Dr. Payman Jula, Ms. Samira Kashani, Dr. Haideh Khorramabadi, Ms. Golnaz Mahmoodieh, Mr. Farhad Massoudi, Mr. Shahpour Matloob, Dr. Jaleh Pirnazar, Mr. Ehsan Saadat, Ms. Sara Saedinia, Mr. Farzin Shadpour, Mr. Hamid Shafiezadeh, Dr. Karim N. Toussi, and Ms. Chakameh Zahed. I cherish these friendships and never take them for granted. Dr. Christine Saroian has always showered

me with her support and she has been so kind to read and edit the first draft of this thesis.

I would like to thank my cousins, Gaguik and Anida, and their families. Gaguik was especially helpful and supportive during the period that I was applying to graduate schools. I express my ultimate gratitude to my beloved aunts, Nora and Zoia and her family, for treating me as their own son and for being so caring and so kind to me throughout my life.

Last but not least, I should confess that I am where I am because of my mother, Clara, my late father, Sarkis, and my brother, Martin. No words of thanks can do justice compared to their selfless efforts in cultivating my personality. I can only say how much I love them and that, for me, their love stands above all in the whole world.

Chapter 1

Introduction

The future belongs to those who can help solve two of our world's most pressing issues, energy and water.

-Ron Pernick

Of the two major world issues, the subject of this dissertation is closely linked to the energy problem with a specific focus on electricity generation using solar power. The energy derived from naturally replenished processes such as wind, tides and geothermal heat is known as renewable energy. In its various forms, renewable energy is derived directly from the sun, or from heat generated deep within the earth. Examples of renewable energy are electricity and heat generated from solar, wind, ocean, hydropower, biomass, geothermal resources, biofuels, and hydrogen derived from renewable resources.

It is astonishing when we realize that the earth receives more energy from the sun in just one hour than the world population uses in a whole year. The intensity of solar radiation outside the atmosphere is about $1,300 \text{ W/m}^2$. When sunlight passes through the earth's atmosphere, a portion is scattered or absorbed by haze, particles, or clouds. On a clear day in the Desert Southwest about 80% to 90% of the solar radiation entering the

atmosphere reaches the ground. The United States has some of the best solar resources in the world, and the intensity of solar radiation at ground level in areas such as Las Vegas can reach values as high as $1,100 \text{ W/m}^2$. For simplicity, the peak incoming solar radiation (insolation) is usually considered to be $1,000 \text{ W/m}^2$. None of these is quite the case in the places where all the people live, however.

The following sections will outline various existing solar technologies. Understanding of each technology and its associated challenges will provide a suitable basis to recognize advantages and drawbacks in each case in an appropriate way.

1.1 Photovoltaics

Photovoltaic (PV) is probably the first and, in some cases, the only technology that comes to mind while discussing the subject of solar electricity generation and utilization. The building block of PV technology is called a solar cell. A solar cell is a semiconductor material which converts sunlight directly into electricity through a solid-state electronic process [1]. PV modules are usually divided into two groups of monocrystalline and polycrystalline silicon. A monocrystalline silicon, is a crystalline in which the crystal lattice of the entire silicon sample is continuous and unbroken to the edges of the sample, with no grain boundaries. However, a polycrystalline silicon (also polysilicon or poly-Si) is made up of a number of smaller crystals known as crystallites. In this context, the word crystalline refers to both monocrystalline and polycrystalline technologies combined.

It does not involve any moving parts or emissions of any kind during operation. These features are attractive from operating, maintenance and environmental standpoints, and have positioned PV to be the preferred power technology for many remote applications,

both in space and on the ground. PV was invented at Bell Labs in the 1950s for powering space satellites. It was commercialized in the 1970s and showed significant growth rates (30% to 60%) since the mid-1990s. In 2001, the total annual manufacturing output of all solar PV companies was about 300 MW. In 2005, manufacturing output of the solar PV industry hit 1,500 MW of PV modules, and it surpassed 2,000 MW in 2006 [2, 3] with installed, unsubsidized costs, now coming close to \$0.20/kWh in the best applications while average electric rates from utilities are less than \$0.10/kWh.

Relative to conventional grid power, photovoltaic electricity is about three to five times more expensive. However, PV is now turning into a mainstream business with familiar names such as BP, GE, Sharp, and Shell [2]. Newer, potentially lower cost photovoltaic technology is emerging from ongoing industry-government research and development programs, and its use in commercial and demonstration applications is beginning. Although increasing use could occur more rapidly in some developing countries, grid-competitive photovoltaic electricity is probably ten to twenty years away in the developed world [4]. The average cost for PV technology in 2006 was roughly \$7 to \$10 per peak watt installed [2]. On the other hand, the average module cost is about \$4.84/W with the lowest monocrystalline and polycrystalline module prices being \$4.35/W and \$4.29/W, respectively [5]. SunPower corporation¹, a leader in PV industry, reported in 2006 that it reached 22% efficiency at the cell level. It currently offers PV modules at 18% peak efficiency. However, climatic effects such as dirt accumulation and temperature rise as well as aging, which causes a gradual increase of the device internal leakage conductance, lower the efficiency. Furthermore, the peak efficiency of a complete PV system that includes wiring and an inverter is lower than

¹<http://www.sunpowercorp.com>

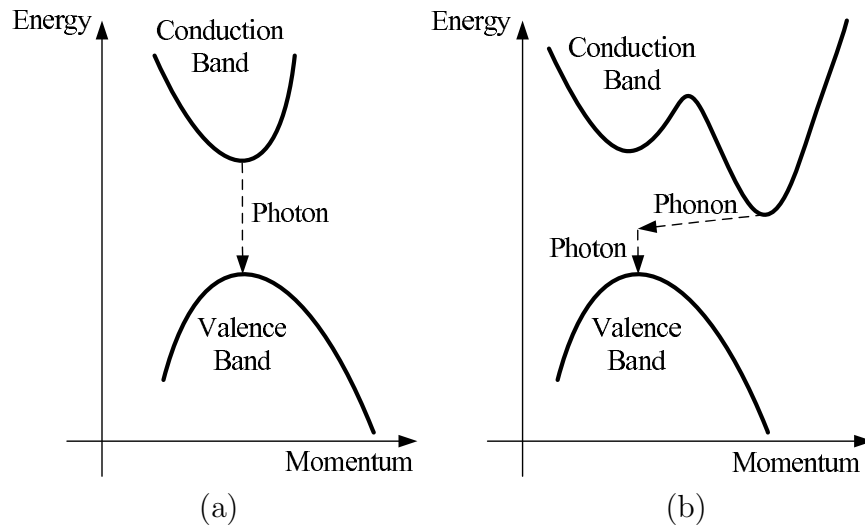


Figure 1.1: Valence and conduction band positioning for (a) Direct band gap and (b) Indirect band gap materials.

the reported figure.

1.2 Thin-Film Photovoltaics

Clearly, one of the biggest challenges and opportunities for entrepreneurs is getting the cost of solar PV to cost parity with conventional retail electricity. Since silicon is the major contributor to the cost of PV technology, it is believed that use of less silicon will have a substantial effect on the cost reduction of the PV technology. Silicon is a semiconductor with indirect band gap. In such semiconductors the minimum energy in the conduction band and the maximum energy in the valence band occur at different values of crystal momentum as illustrated in Figure 1.1. Therefore, photon energies much larger than the forbidden gap are required to give direct transitions of electrons from the valence band to the conduction band. Nevertheless, transitions can occur at lower energies by a two-step process involving not only photons and electrons but also a third particle known as phonon. A phonon is just a quantum or fundamental particle corresponding to the

coordinated vibration. As opposed to photons, phonons have low energy but relatively high momentum. Since the light absorption process in such materials involves an extra particle, the probability of light being absorbed by this process is much less than in the direct band gap case. Therefore, the absorption coefficient is low and light can pass a reasonable distance into the semiconductor prior to absorption [1].

Thin-film PV technologies utilize direct band gap semiconductors (e.g. Cu(In,Ga)Se_2 or CdTe). This increases the efficiency of solar energy conversion into electricity (i.e., more power per unit mass or more watts per kg of material) compared to the indirect bandgap semiconductor materials used for conventional PV technologies. For instance, a CIGS (short form of Cu(In,Ga)Se_2) film as thin as 1 micron produces a photoelectric effect equal to that of a crystalline silicon wafer that is 200-300 microns thick. In other words, CIGS cells use less than 1% of the semiconductor material required by crystalline silicon cells, which yields an inherent and sustainable cost advantage [6].

The CIGS photovoltaic effect was first discovered in the 1970s. Since then, government and university labs have dramatically advanced the understanding and efficiency of CIGS material, achieving 19.5% conversion efficiency at the Department of Energy's National Renewable Energy Lab (NREL). This level of efficiency is comparable to polycrystalline silicon solar cells, which represent the preponderance of the current production and installed modules in the solar industry. CIGS solar cells offer several advantages over crystalline silicon solar cells. In particular, CIGS cells are extremely lightweight, less expensive per unit of electric output power, more efficient in low-angle and low-light conditions, and flexible enough to conform to small-radius curves. CIGS has also proven to be stable in a field environment, with modules under test for more than fifteen years. CIGS has been

produced commercially in modest volumes for nearly a decade, but the industry has lacked a high-volume manufacturing technology to fully realize its potential [6].

CdTe has shown interesting features as well. Solar cells become less efficient at converting solar energy into electricity as their cell temperatures increase. However, the efficiency of CdTe is less susceptible to cell temperature increases, enabling CdTe solar modules to generate relatively more electricity under high ambient (and therefore high cell) temperatures [7]. CdTe also absorbs low and diffuse light and more efficiently converts it to electricity under cloudy weather and dawn and dusk conditions where conventional cells operate less efficiently. As a result, CdTe will generally produce more electricity under real world conditions than a conventional solar module with similar power ratings. In addition, CdTe permits simple device structures and processes, leading to low cost production. Its robustness enables relatively simple device structures and production processes. High performance modules are achieved with single junction, polycrystalline devices. Automated high throughput production processes have been employed successfully with CdTe, without the need for expensive clean rooms or other expensive specialty equipment [7]. Furthermore, CdTe is made by transforming cadmium and tellurium into a stable, inert semiconductor. Both elemental materials are produced as byproducts of mining processes (primarily zinc mining and copper refining) and present in abundant quantities to support multi-GWs of annual production.

Recent technical achievements reported highest device efficiency of 19.3% for CIGS and 16.5% for CdTe [8]. The cheapest thin-film PV module costs \$3.59/W [5]. Miasolé² is a startup company that promises to bring high-volume, thin-film manufacturing technology

²<http://www.miasole.com>

to the CIGS solar industry. First Solar³ is a publicly-traded company based on CdTe technology that is currently focused on serving customers engaged in the development of large-scale commercial projects and do not offer their module products for residential applications. First Solar is currently selling solar modules in the European market for \$2.10/W. CdTe module costs well below \$1.00/W have been predicted by NREL.

1.3 Concentrated Photovoltaics

Concentrated PV (CPV) technology is distinct from standard PV technology in that it replaces most of the PV cell area with a set of reflectors in order to reduce costs. This premise uses the theory that the reflectors are cheaper than the PV would have been. Concentrating systems may add an additional layer of complication: systems with high concentration ratios (above 5) are efficient when direct sunlight is reflected and, hence, the system must accurately track the sun at all times, which adds complexity and cost. Due to the complexity and expense of optics, trackers, and cooling, the overall cost-effectiveness is best when the highest efficiency (40%) cells are used. Hence, CPV systems tend to use non-silicon solar cells, such as triple-junction GaAs-Ge-GaInP₂, which are much more expensive and more efficient than standard silicon cells. A distinct advantage that CPV has over conventional “one sun” PV is the present bottleneck in the PV industry due to a scarcity of purified silicon, that will likely persist for several years. A CPV system with concentration ratio of 500 (or 500 suns) generally uses 1/500 the amount of PV cell surface area as does conventional PV, so the price of the PV cell constitutes a smaller cost

³<http://www.firstsolar.com>

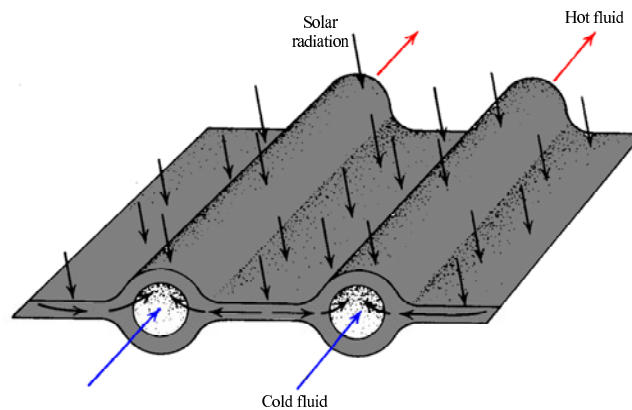


Figure 1.2: Absorber plate of a typical flat-plate solar collector.

consideration for CPV even if using expensive cells. Energy Innovations⁴ and SolFocus⁵ are two startup companies that are pursuing serious efforts in this field. SolFocus projects the cost of its Gen1 CPV system to become as low as \$1/W at 1 GW production level [9]. Further, SolFocus Gen2 systems are expected to achieve 26% efficiency and a record cost less than \$0.50/W.

1.4 Residential Water Heating

Domestic solar water heaters can be a cost-effective way to generate hot water for residential homes. Solar water heating systems include a well-insulated storage tank and solar collector modules. Solar collectors are the key component of solar-heating systems since they gather the sun's energy, transform its radiation into heat, then transfer that heat to water, heat transfer fluid, or air. The solar thermal energy can be used in solar water-heating systems, solar pool heaters, and solar space-heating systems. There are three types of solar collectors:

⁴<http://www.energyinnovations.com>

⁵<http://www.solfocus.com>

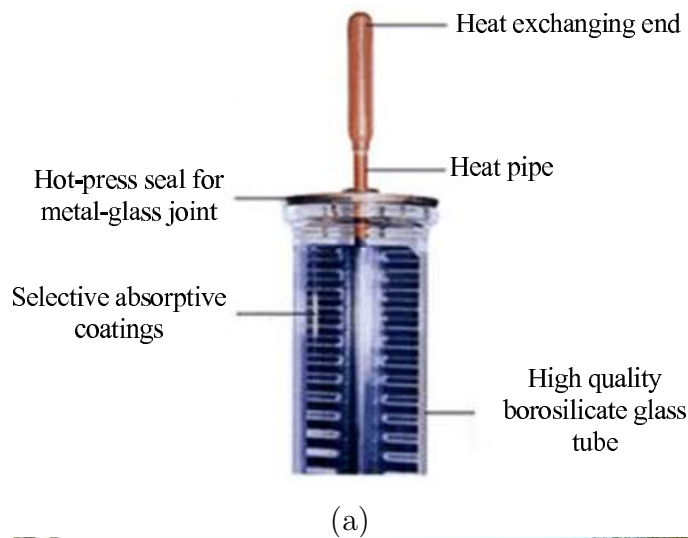


Figure 1.3: (a) Close-up view of an evacuated-tube collector. (b) A typical evacuated-tube collector system for residential water heating. Courtesy of Beyond Oil Solar.

Flat-plate collectors: Glazed flat-plate collectors are insulated, weatherproofed boxes that contain a dark absorber plate, Figure 1.2, under one or more glass or plastic (polymer) covers. Unglazed flat-plate collectors – typically used for solar pool heating – have a dark absorber plate, made of metal or polymer, without a cover or enclosure.

Evacuated-tube solar collectors: They feature parallel rows of transparent glass tubes. Each tube contains a glass outer tube and metal absorber tube, which acts as a heat pipe and it is attached to a fin as shown in Figure 1.3(a). The selective coating of the fin absorbs solar energy but inhibits radiative heat loss. These collectors are used more

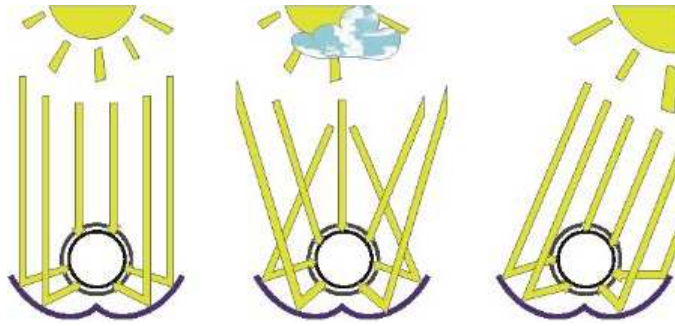


Figure 1.4: CPC operation under different sunlight conditions: direct, dispersed, and skewed.

frequently for U.S. commercial applications.

Compound Parabolic Collectors: Abbreviated as CPC, they are another family of collectors that enhance the efficiency of evacuated-tube collectors through nonimaging optics [10]. Figure 1.4 shows the cross-sectional view of a CPC and indicates how the collector can successfully operate in three different sunlight conditions. CPCs can achieve temperatures close to 232 °C without tracking [11] due to their wide acceptance angle.

All the mentioned solar collectors have simple components and can be manufactured by relatively easy processes compared to that of PV or thin-film technologies. Figure 1.5 compares the typical efficiency variation of flat-plate, evacuated-tube, and compound parabolic collectors versus temperature. A 25-tube evacuated-tube collector system with gross collector area of 2.6 m² could retail for about \$769 [12]. In chapter 2, where a low-cost solar-thermal-electric technology is introduced, material cost breakdown of a typical solar collector will be considered and analyzed as well.

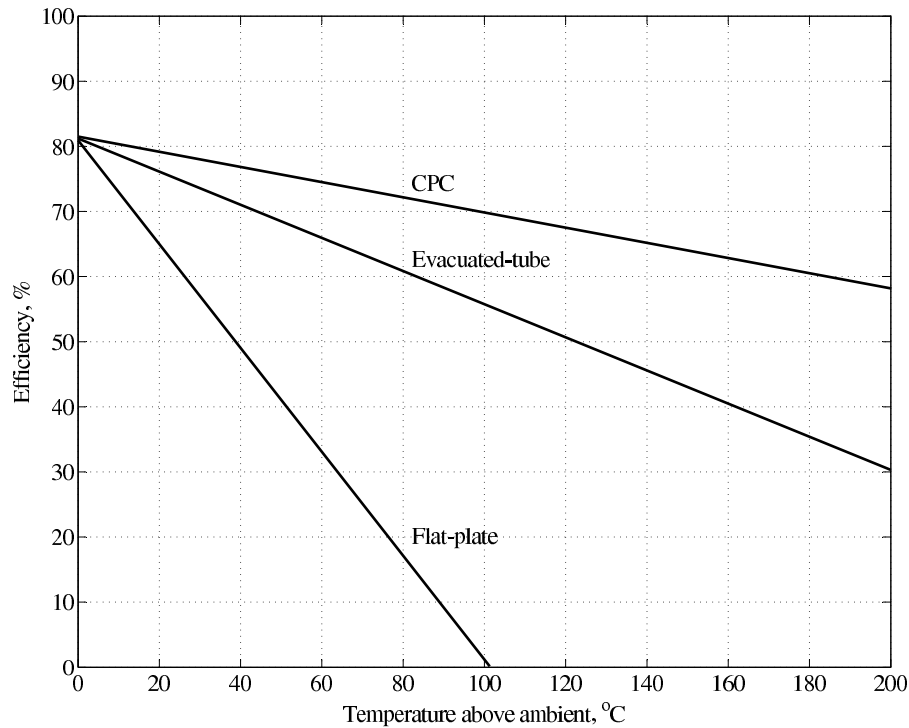


Figure 1.5: typical efficiency comparison of CPC and flat-plate collectors for 1000 W/m^2 solar insolation. Courtesy of Prof. Roland Winston.

1.5 Solar Parabolic Trough

In 1984, the first of the concentrating solar power plants began converting solar energy into electricity in California's Mojave Desert [13, 14]. It was a plant based on solar parabolic trough technology. These plants are large fields of single-axis collectors shaped as parabolic reflectors (mirrors) similar to a trough, Figure 1.6. The collectors are aligned on a north-south horizontal axis in parallel rows. They track the sun from east to west during the day to ensure that the sun's direct beam radiation is continuously focused on the absorber tubes that contain a heat transfer fluid. The receiver tubes are usually metallic and embedded into an evacuated glass tube to reduce heat losses. A special high-temperature coating additionally reduces radiation heat losses [15]. The collectors concentrate sunlight

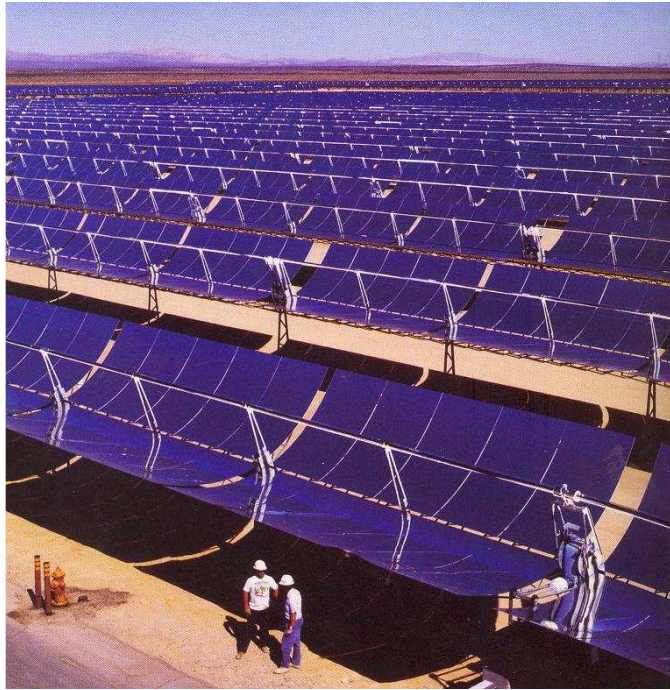


Figure 1.6: A solar trough plant in California (SEGS). Image courtesy of DOE.

30 to 60 times the normal intensity on the absorber, heating up the heat transfer fluid to temperatures as high as $390\text{ }^{\circ}\text{C}$. The receiver tubes are usually installed inside an evacuated glass tube. The vacuum provides a great thermal insulation at such high temperatures. The working fluid is then pumped through a series of heat exchangers to produce superheated steam which powers a conventional turbine/generator system (Rankine cycle) for electricity production. It is also possible to produce superheated steam directly using solar collectors. This obviates the intermediate working fluid and also reduces costs. However, direct steam generation is still in the prototype stage and more research is required to solve the thermo-mechanical issues related to working pressures above 100 bar and the presence of a two-phase fluid in the receiver tubes [15, 16, 17].

The solar parabolic trough is currently the most proven solar-thermal-electric technology due to the successful operation of nine large commercial-scale solar power plants with sizes ranging from 14 to 90 MW. Originally designed to be operated on solar alone,

currently they are hybridized with fossil-fueled plants to supplement the solar input during periods of low solar radiation. The efficiency of a solar thermal power plant is the product of the collector efficiency, the efficiencies associated with transferring heat to steam-cycle, and steam-cycle efficiency. The collector efficiency depends on the angle of incidence of the sunlight and the temperature in the absorber tube, and can reach values up to 75%. Thermal losses are usually below 10%. Altogether, solar thermal trough power plants can reach annual efficiencies of about 15% with a capacity factor of about 55% [15, 13].

The capacity factor of a power plant is the ratio of the actual output of a power plant over a period of time and its output if it had operated at full capacity over that time period. This is calculated by totaling the energy the plant produced and dividing it by the energy it would have produced at full capacity. There are two main reasons why a plant would have a capacity factor lower than 100%. The first reason is that it was out of service or operating at reduced output for part of the time due to equipment failures or routine maintenance. This accounts for most of the unused capacity of base load power plants. Base load plants have the lowest costs per unit of electricity because they are designed for maximum efficiency and are operated continuously at high output. Geothermal plants, nuclear plants, coal plants and biomass plants that burn solid material are almost always operated as base load plants. The second reason is that output is curtailed because the electricity is not needed or because the price of electricity is too low to make production economical. This accounts for most of the unused capacity of peaking power plants. Peaking plants may operate only a few hours per year or up to a several hours per day. Their electricity is relatively expensive. It is uneconomical, even wasteful, to make a peaking power plant as efficient as a base load plant because they do not operate enough to pay for the extra equipment

cost, and perhaps not enough to offset the embodied energy of the additional components. When it comes to solar power, wind power and hydroelectricity, there is a third reason for unused capacity. The plant may be capable of producing electricity, but its fuel, wind, sunlight or water, may not be available. A hydroelectric plant's production may also be affected by requirements to keep the water level from getting too high or too low and to provide water for fish downstream. However, solar, wind and hydroelectric plants do have high availability factors, so when they have fuel available, they are almost always able to produce electricity.

Ausra⁶, a startup company located in Palo Alto, CA, has recently attracted considerable amount of Venture Capital (VC) money for its proposed technology. Ausra's new technology is the Compact Linear Fresnel Reflector (CLFR), which utilizes a fixed pipe absorber and simple nearly flat rotating mirrors to dramatically reduce the cost of the power plant. The water boils to generate high-pressure steam, and from that point on, the process is the same as a conventional power plant as explained above. They are currently building a 30 MW power plant, and are in the process of scaling up to 2000 MW over the next 3 years.

1.6 Solar Power Tower

Solar power towers are commercially less mature than parabolic trough systems. However, a number of component and experimental systems have been field-tested around the world (Russia, Italy, Spain, Japan, France, and the United States) in the last 25 years with the output powers ranging from 0.5 to 10 MW [15, 14, 18]. In a solar power tower

⁶<http://www.ausra.com>



Figure 1.7: Solar Two plant in Mojave Desert, California. Image courtesy of NREL.

plant, shown in Figure 1.7, hundreds to thousands of two-axis sun-tracking mirrors called heliostats are installed around a tower, which could be as tall as a fifty-story building, where they focus sunlight with concentrations ranging from 100 to 10,000 suns. Various combinations of heat transfer fluids such as steam, air, liquid sodium, or molten nitrate salt are usually used to transport the heat from the absorber, which is located on the top of the tower, to a steam generator where superheated steam is produced to drive a conventional Rankine-cycle turbine/generator system. Thermal storage medias like water/steam, nitrate salt/water, sodium, oil/rock, and ceramic can be easily integrated with this type of solar systems to increase the annual capacity factor, which is about 25% without thermal storage, and to enhance the stabilization of the power output through fluctuations in solar intensity until the stored energy is depleted. In a molten-salt solar power tower, liquid salt at $290\text{ }^{\circ}\text{C}$ is pumped from a “cold” storage tank through the absorber where it is heated to $565\text{ }^{\circ}\text{C}$ and then on to a “hot” tank for storage [19, 20].

On the downside, solar power towers must take advantage of economies of scale and

can only be built cost effectively in 50 or 100 MW units. Also, they require the largest amount of space per unit of produced power compared to any concentrated solar power (CSP) technology. The efficiency of a solar-powered steam turbine/generator used in the power tower concept is a critical function of the absorber temperature, which is influenced not only by the incident energy but also by several factors including the heliostat optical performance, the mirror cleanliness, the accuracy of the tracking system, and wind effects.

Solar power tower plants can be hybridized with conventional fossil-fired plants. Many options are possible with natural gas combined-cycle and coal-fired or oil-fired Rankine plants. In hybrid plants, the solar energy can be used to reduce fossil fuel usage or boost the power input to the steam turbine.

The two solar power tower systems that were built in the US, as demonstration plants, were named Solar One (1982-1988) and Solar Two (1995-1999). The units operated successfully, but were decommissioned after the demonstration period. Though new power tower systems are not being actively pursued in the US, a new solar power tower, known as Solar Tres, is being constructed in Spain [21]. It is a 17 MWe plant with 15 hours of thermal energy storage and estimated 6500 hours of operation per year (i.e. 74% capacity factor).

1.7 Solar Dish-Engine Systems

A photo of a solar dish-engine system owned and operated by Stirling Energy Systems is shown in Figure 1.8. Such a system can be used to generate electricity in the kilowatts range. The ideal concentrator shape is a paraboloid of revolution which concentrates sunlight on the focus of paraboloid. Concentration ratio is typically over 2000 and, hence, the



Figure 1.8: Solar Dish-Stirling system. Image courtesy of Stirling Energy Systems (SES).

concentrator must track the sun in two axes. Tracking in two axes is accomplished in either azimuth-elevation tracking or polar tracking [15]. In azimuth-elevation tracking, used for larger systems, the dish rotates in a plane parallel to the earth (azimuth) and in another plane perpendicular to it (elevation). In the polar tracking method, used for the smaller systems, the collector rotates about an axis to the earth's axis of rotation. The collector rotates at a constant rate of $15^\circ/\text{hr}$ to match the rotational speed of the earth. The other axis of rotation, the declination axis, is perpendicular to the polar axis. Movement about this axis occurs slowly and varies by $\pm 23.5^\circ$ over a year. Tracking should be performed with a high degree of accuracy in order to achieve high efficiencies.

At the focus is a receiver which is heated up to over 700°C . The absorbed heat drives a thermal engine which converts the heat into motive energy and drives a generator to produce electricity [15, 22]. The solar-to-electric conversion efficiency of dish-engine systems can be as high as 30%, with large potential for low-cost deployment. For the moment, the

electricity generation costs of these systems are much higher than those for trough or tower power plants, Table 1.1. A number of prototype dish-engine systems are currently operating in Nevada, Arizona, Colorado, and Spain. High levels of performance have been established; durability remains to be proven, although some systems have operated for more than 10,000 hours [23, 24, 25].

Various thermodynamic cycles have been considered for dish-engine systems. Stirling and open Brayton (gas turbine) cycles have shown the best performances to date. Stirling engines have a potential for high efficiency and external heating makes them easily adaptable to solar dishes. Modern, high-performance Stirling engines use hydrogen or helium working gas at temperatures over 700 °C and pressures as high as 200 bar, resulting in thermal-to-electric conversion efficiencies of about 40%. The main disadvantage of these types of engines is their manufacturing cost, mainly determined by the materials used for the hot side heat exchanger (stainless steel, high-temperature alloys or ceramic materials) and by the design of the cooling system. In a dish-Brayton system, solar heat is used to replace or supplement the fuel at the entrance of the gas turbine. Current designs include pressure ratios of about 2.5, turbine inlet temperatures of about 850 °C, and recuperation of waste heat, with predicted efficiencies over 30%. Dish-Brayton systems are still at an early stage of development.

Infinia Corporation⁷ and Stirling Energy Systems, Inc. (SES)⁸ have been successful in attracting VC capital and long term agreements with utilities to design and construct solar dish-engine plants. SES power plants will be constructed in the Imperial Valley and Mojave Desert by 2012-2014 with capacities of 300 to 500 MW [25].

⁷<http://www.infiniacorp.com>

⁸<http://www.stirlingenergy.com/>

Table 1.1: Cost of concentrated solar-thermal-electric technologies.

	Solar Dish-Engine	Parabolic Trough	Solar Power Tower
Standard plant size, MW	2.5 to 100	100	100
Max efficiency, %	30	24	22
Specific power, W/m ²	200	300	300
Basic plant cost, \$/W	2.65	3.22	3.62
Total US installation, MW	0.118	354	10
Largest unit in the US, MW	0.025	80	10
Demonstrated system hours	80,000	300,000	2,000

1.8 Thesis Contribution and Structure

While the large companies continue to drive down the PV costs, other new ideas may totally change the situation with breakthrough technology and significantly lower pricing. Any current or emerging technology that can bring the cost of an entire solar PV system to around \$2 per peak watt will be in a very good position. Systems priced at this level would provide electricity at less than \$0.10/kWh. It is believed that someone will break this price barrier by 2015, paving the way for a low-cost, ubiquitous, solar future [2].

This thesis discusses the technical merits of a technology that combines the solar-thermal technology with moderate-temperature Stirling engine to generate electricity. The conceived system incorporates low-cost materials such as steel, aluminum, copper, glass, and plastics, and utilizes simple manufacturing processes. Therefore, as it will be shown, the proposed system has the potential to cost less than \$1/W. Hence, chapter 2 outlines a thorough description and analysis of the Low-Cost Solar-Thermal-Electric Power Generation technology proposed in this dissertation. Solar-thermal technology is relatively mature and there is no need for further elaboration in this dissertation. However, moderate-temperature Stirling engines are yet to be explored and optimized. Chapter 3 elaborates the inherent non-ideal effects of the main components in Stirling machines. Two prototypes,

one single-phase and one three-phase, were fabricated as part of this work to help us have a better understanding of the Stirling engine systems. Design, fabrication, and test results of the single-phase prototype are outlined in chapter 4. Multi-phase free-piston Stirling engines are of special interest for eliminating the displacer piston and incorporating only one moving piston per engine. Chapter 5 is dedicated to a detailed dynamical analysis of this special family of Stirling engines. Design, fabrication, and test results of the three-phase prototype are outlined in the same chapter for comparison of the theoretical predictions with prototype results. Finally, chapter 6 outlines a suitable Stirling engine design for solar-thermal-electric power generation and offers future scopes of the technology.

Chapter 2

Low-Cost Solar-Thermal-Electric Power Generation

2.1 Introduction

In this chapter, the technical and economic feasibility of a low-cost distributed solar-thermal-electric power generation technology is discussed, which is based on the use of a solar-thermal collector (STC) in conjunction with a free-piston Stirling engine. The solar-thermal collector is to be comprised of low-concentration nonimaging concentrators and absorbers with spectrally selective coatings. The Stirling engine converts moderate temperature heat to electricity by way of integrated electric generation. In spite of its relatively low conversion efficiency, the proposed system can be a cost-effective alternative to PV technology, as discussed in the sequel.

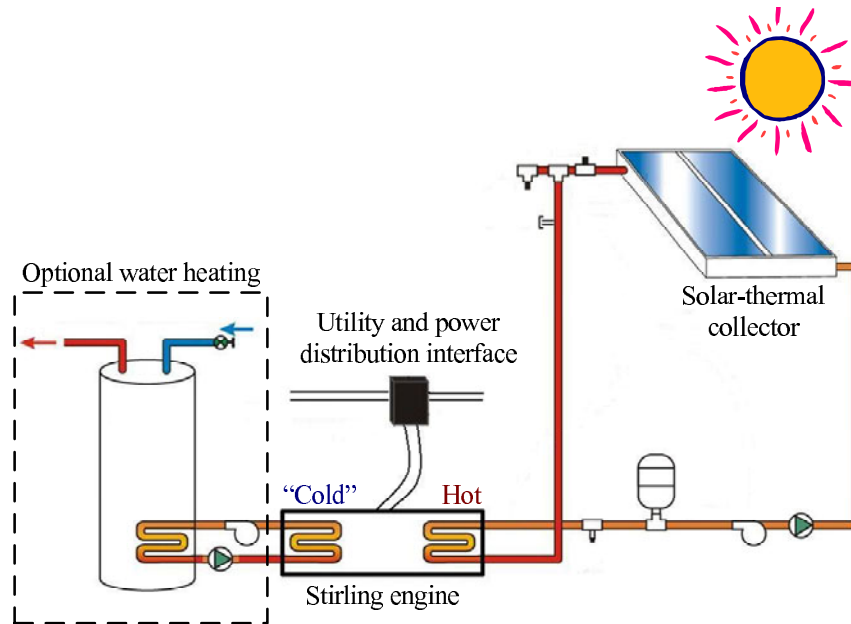


Figure 2.1: Schematic diagram of the solar-thermal-electric power generation system.

2.2 System Topology

The proposed energy conversion system is conceived to convert solar power into electricity in three stages: solar to thermal, thermal to mechanical, and mechanical to electric. The system is conceived to operate with collector temperatures in the range of 120 °C to 150 °C, which is consistent with the use of stationary solar thermal collectors employing low-concentration nonimaging reflectors [10, 26, 27]. A non-tracking system avoids the costs and maintenance issues associated with tracking collectors with high concentration ratios. Thus, a nonimaging solar collector is a very suitable component to serve as the first energy conversion stage of the proposed system. Figure 2.1 illustrates the schematic diagram of the proposed system.

A Stirling engine is utilized to convert the delivered heat by the solar collector into mechanical power. One potential advantage of the Stirling cycle is the possibility of using air as the working fluid, and thus avoiding issues with long-term containment of a working

fluid such as helium and the associated maintenance requirements. Further, recent success in demonstrating very low differential temperature engines is also compelling [28]. In the system conceived here, the Stirling engine converts moderate temperature heat to electricity by way of integrated electric generation. However, the use of low-temperature heat limits the theoretical maximum thermodynamic efficiency achievable by the heat engine, which limits the overall system efficiency. This disadvantage, however, can be compensated by lower costs in materials and in reduced maintenance. Cost effectiveness of solar-electric technologies should be judged by output power per dollar rather than by efficiency or other technical merits [29]. This view reflects the observation that there are vast, untapped siting opportunities in both urban and rural regions of the world. The proposed solar-thermal-electric system is designed for fabrication out of low-cost materials. A collector is built of glass, copper, selective coating, and insulation, while engines and generators are primarily steel, aluminum, copper, and plastics. In high-volume manufacturing, the cost of the proposed system will be determined by the weight of its bulk materials. This study of solar-thermal-electric systems involves searching for a more cost-effective balance between system efficiency and materials cost.

2.2.1 Market Available Collectors

Solar-thermal collectors generally consist of a transparent cover and a selective absorber surface, under which there is tubing to guide heat transfer liquid and insulation to reduce thermal losses. The solar hot water industry has improved upon flat-plate collectors by reducing optical and thermal losses by using high transmission covers and selective absorber materials. More recent designs have employed nonimaging compound parabolic

concentrator (CPC) reflectors and vacuum insulation to improve collector performance. For a small sacrifice in maximum collector efficiency due to imperfect reflector surfaces, CPCs effect a reduction in thermal losses in proportion to the concentration ratio. Furthermore, since the reflector can be much thinner and lighter than the absorber plate it obviates, the collector cost per unit area can be substantially reduced. The system is envisioned to use collectors based on low-cost truncated 2D CPCs with concentration ratio of about 1.5 or evacuated-tube collectors equipped with heat pipes. The large acceptance angle associated with a CPC will allow for sufficient hours of operation over all seasons without any tilt adjustments. The SOLEL CPC 2000 trough array [30] and Schott ETC 16 evacuated-tube [27] are examples of such collectors.

Table 2.1 compares the technical and economic performance of several commercially produced flat plate, CPC-based, and evacuated-tube solar-thermal collectors [26, 27, 31]. Parameters η_0 , U_1 , and U_2 specify the efficiency characteristic of a collector as defined in Eq. (2.1), T_m^{opt} , η_{STC}^{opt} , and η_{sys}^{opt} are, respectively, the calculated optimal operating temperature, the collector efficiency at the optimal temperature, and the overall solar-thermal-electric system efficiency at the optimal temperature. Although many of these collectors are already shown to be cost-effective at retail prices, the production cost of such collectors is undoubtedly much lower.

2.2.2 Stirling Engines

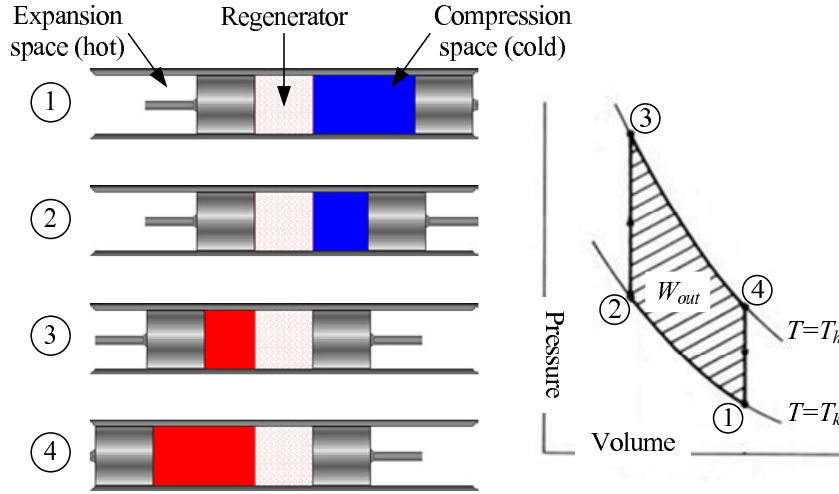
The Stirling Engine has been in existence for many years, spread over two centuries. The research and development on Stirling cycle machines has been documented in open literature such as references [33, 34, 35]. The Stirling engine converts heat to mechanical

Table 2.1: Comparison of market available STCs. Assumptions: $G=1000 \text{ W/m}^2$, $\epsilon_{Carnot} = 66\%$, $T_{amb} = 27 \text{ }^\circ\text{C}$. System costs are computed assuming engine cost is zero. All costs are approximated by discounted retail price of 500 m^2 collector area. Parentheses indicate presumed values.

Collector Model	η_0 %	U_1 $\text{W/m}^2\text{K}$	U_2 $\text{W/m}^2\text{K}^2$	T_m^{opt} $^\circ\text{C}$	η_{STC}^{opt} %	η_{sys}^{opt} %	Cost $\$/\text{m}^2$	Cost $\$/\text{W}$
Flat Plate Collectors								
Arcon HT (original)	75	2.69	0.0050	121	45.3	7.1	-	-
Arcon HT (improved [32])	82	2.44	0.0050	133	50.5	8.7	-	-
Arcon SI-250-N	69.2	3.057	0.0078	104	41.0	5.5	-	-
Solarnetix FC-25	85	4.840	(0)	105	47.2	6.43	150	2.33
Sonnenkraft GK6	88	5.487	(0)	99	48.5	6.2	145	2.34
HFE Solar Eurostart Sc	86	5.180	(0)	101	47.7	6.2	174	2.81
Thermo Dynamics G Series	73.8	5.247	(0)	91	40.2	4.7	194	4.12
CPC-Based Collectors								
SOLEL CPC 2000 1.2 \times	91	4.080	(0)	123	51.8	8.3	193	2.33
AOSOL CPC 1.5 \times	75	4.280	(0)	105	41.6	5.7	158	2.77
Evacuated-Tube Collectors								
Apricus	71.7	1.52	0.0085	132	46.3	7.9	100	1.27
Schott ETC 16	77.3	1.09	0.0094	142	52.3	9.6	-	-

power in a manner similar to other mechanical engines, that is, by compressing a working gas when it is cold, heating the compressed working gas, and then expanding it with a power piston to produce work.

The ideal Stirling cycle satisfies the Carnot requirements of reversibility and can be described with reference to Figure 2.2, where snapshots of four extreme positions of the Stirling engine pistons are depicted with corresponding thermodynamic cycle p - V characteristics. In this figure, one of the mechanical configurations for realizing the Stirling cycle is shown, being known as the dual piston arrangement, or more commonly as the Alpha arrangement. The regenerator, which is generally located between cold and hot sides of the engine, comprises a matrix of fine wires. Process 1-2 is the isothermal compression process during which the heat is removed from the engine at the cold sink temperature. Similarly,

Figure 2.2: Stirling cycle p - V loop.

process 3-4 is the isothermal expansion process during which heat is added to the engine at the hot source temperature. Processes 2-3 and 4-1 are the constant volume displacement processes in which the working gas is passed through the regenerator. During the process 4-1 the working gas gives its heat up to the regenerator matrix, to be recovered subsequently during the process 2-3. Thus, even though quite considerable quantities of heat are transferred during the displacement process, they are seen to be externally adiabatic, fulfilling the Carnot requirements for maximum attainable efficiency [33].

It is extremely difficult even to approach isothermal working spaces with conventional heat exchanger technology. Regenerators, on the other hand, can be designed to be highly effective. Thus separate heat exchangers for the heater and cooler are usually introduced. In the adiabatic model of the Stirling cycle, the ideal cycle is considered to have isothermal heater and cooler components, while the expansion and compression spaces (or working spaces) are considered to be adiabatic. In contrast, the isothermal model, which is the ideal cycle representing all Stirling engines, considers purely isothermal working spaces and ideal heat exchangers [33].

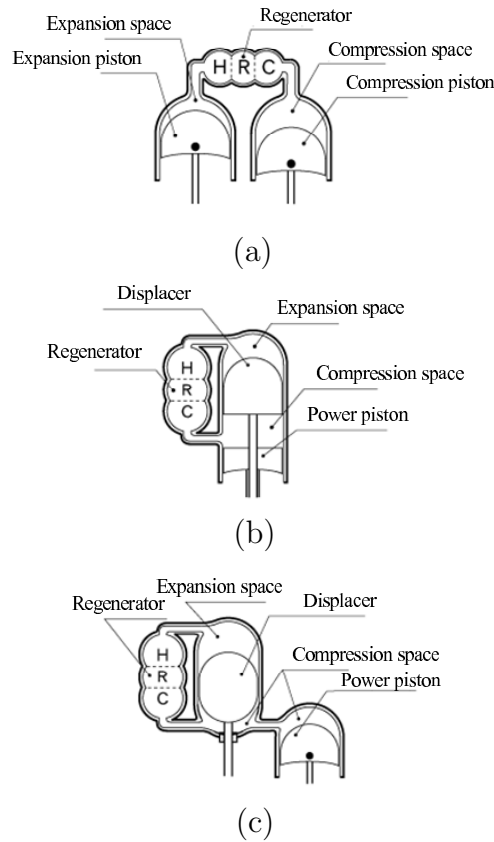


Figure 2.3: Three common mechanical configurations of Stirling engines: (a) Alpha, (b) Beta, and (c) Gamma. Images courtesy of Koichi Hirata.

The mechanical configurations of Stirling engines are generally divided into three groups, known as the Alpha, Beta, and Gamma arrangements as shown in Figure 2.3. Alpha engines have two pistons in separate cylinders which are connected in series by a heater, regenerator, and cooler. Both Beta and Gamma engines use displacer piston arrangements, the Beta engine having both the displacer and the power piston in the same cylinder while the Gamma engine uses separate cylinders.

This dissertation will focus on free-piston Stirling engines rather than machines incorporating conventional crank mechanisms and, of course, free-piston machines that directly drive electrical generation devices. Removal of the mechanical crank mechanism reduces

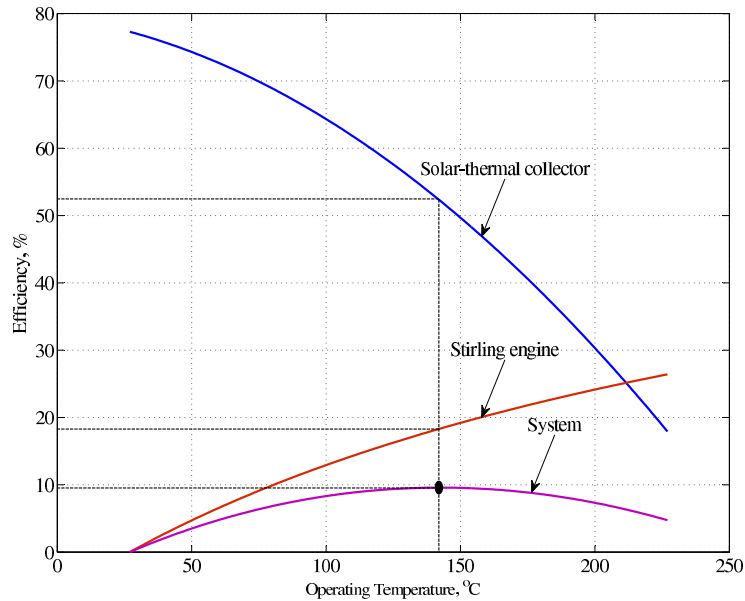


Figure 2.4: Efficiency as a function of temperature for a representative system. The parameters used are $G = 1000 \text{ W/m}^2$, $\eta_0 = 77.3\%$, $U_1 = 1.09 \text{ W/m}^2\text{K}$, $U_2 = 0.0094 \text{ W/m}^2\text{K}^2$, $T_{amb} = 27 \text{ }^\circ\text{C}$, $T_{cold} = 27 \text{ }^\circ\text{C}$, and $\epsilon_{Carnot} = 66\%$. The dot indicates the point of optimal system efficiency.

frictional losses, complexity, and associated maintenance requirements. With this arrangement, there is no need for any mechanical coupling from the moving elements to the outside of the pressurized container. Thus, there is no emphasis on difficult sealing requirements that have plagued conventional crank mechanisms in Stirling designs. A further advantageous feature of the machine is that the power piston could be realized with a flexible diaphragm or clearance seal, rather than with a sliding piston to eliminate leakage around the piston and any potential need for lubrication.

2.3 System Efficiency

The efficiency of a solar-thermal collector, η_{STC} , as measured experimentally, is given by,

$$\eta_{STC} = \eta_0 - \frac{U_1}{G} (T_m - T_{amb}) - \frac{U_2}{G} (T_m - T_{amb})^2 \quad (2.1)$$

where η_0 is the maximum collector efficiency, U_1 and U_2 are the thermal loss coefficients, G is the power density of incident sunlight, T_m is the mean temperature of the collector in the Kelvin scale (K), and T_{amb} is the ambient temperature in K. Assuming there is no drop in temperature from the collector to engine, the efficiency of the heat engine, η_{eng} , is given by,

$$\eta_{eng} = \epsilon_{Carnot} \left(1 - \frac{T_{cold}}{T_m} \right) \quad (2.2)$$

where ϵ_{Carnot} is the fraction of the theoretical Carnot efficiency that the engine achieves and T_{cold} is the “cold side” working temperature of the Stirling engine in K. The system conversion efficiency, η_{sys} , is then given by,

$$\eta_{sys} = \eta_{STC} \cdot \eta_{eng} \quad (2.3)$$

For a representative system, the efficiencies of the collector, engine, and system are plotted as a function of temperature in Figure 2.4. To minimize cost per watt of output electricity, it is desirable to operate a system of given cost at the temperature corresponding to peak system efficiency. This temperature is a function of collector properties as well as ambient temperature and intensity of sunlight. The heat engine can be designed to regulate its loading to maintain optimum collector temperature and system efficiency. Figure 2.4 shows

that the system efficiency is rather flat over a range of temperatures near the extremum.

An operating temperature of 142 °C permits a maximum thermodynamic (Carnot) efficiency of 31.6%, assuming the sink temperature is 27 °C. We might reasonably expect the Stirling engine and generator to achieve a thermal-electric efficiency of about 20.8%, roughly 66% of the Carnot efficiency, while the collector operates at a thermal efficiency of about 52.3%. Thus, the estimated overall efficiency of the system would be about 9.6%.

2.4 System Cost Analysis

The system cost per watt (CPW) of peak electricity output is an important figure of merit for judging cost effectiveness of investment in an electrical generation system. Since investors (system owners) prefer a short period after which the revenue from energy sold offsets the initial investment, the output power of the system should be maximized for a fixed capital cost. The cost per unit peak output power of the proposed system, CPW_{sys} , is given by,

$$CPW_{sys} = CPW_{eng} + \frac{CPA_{STC}}{G_{peak} \cdot \eta_{sys}^{opt}} \quad (2.4)$$

where CPW_{eng} is the engine cost per watt, CPA_{STC} is the collector cost per area (CPA), G_{peak} is the peak solar insolation, and η_{sys}^{opt} is the optimal efficiency of the entire solar-thermal-electric system.

PV modules currently retail for as low as \$4.29 per watt of peak output electrical power [36]. Solar-thermal collectors are primarily comprised of evacuated glass tubes, copper heat pipes and manifold, and thermal insulation. One can expect that the cost of collectors and Stirling engine machines will be limited only by material cost in large

Table 2.2: Materials cost breakdown of Thermo Dynamics G Series STC.

Collector Material	Mass, kg/m ²	Specific Cost, \$/kg	Cost, \$/m ²
Low-Iron Cover Glazing	7.8	1.87	14.60
Sheet Aluminum	2.75	6.00	16.50
Sheet Copper	1.26	6.35	8.00
Fiberglass Insulation	1.2	0.83	1.00
Total	13	N/A	40.10

volume manufacturing. In mature, cost-optimized large-volume industries such as those manufacturing electric motors, automotive parts and other industrial products, the cost of products is proportional to the weight of materials used. Since collectors will dominate the mass of the system, they will dominate the cost of the system in large-scale manufacturing. Assuming that CPW_{eng} is negligible, $G_{peak} = 1000 \text{ W/m}^2$, and $\eta_{sys}^{opt} = 10\%$, the collectors for our system must retail for less than $\$340/\text{m}^2$ to match the present day price of PV technology. A market survey (see Table 2.1) of stationary collectors for solar heat reveals that several models retail in quantities of 500 m^2 for less than $\$200/\text{m}^2$, independent of performance [31]. Furthermore, the materials cost breakdown for the most expensive system, shown in Table 2.2, indicates that a representative collector for hot water can easily undercut this cost requirement considering economies of scale. Note that specific cost of metals is taken from reference [37] in 2003. Based on the materials cost breakdown in Table 2.2 and a complete system efficiency of 9.6%, the estimated collector material cost is roughly $\$0.42/\text{W}$. Also, considering that the manufacturing cost of an evacuated-tube collector is less than $\$3$ per tube for a Chinese product [38], the same figure could be confirmed assuming 0.075 m^2 input aperture for each tube.

The cost of the Stirling engine may be estimated by calculating the mass of materials

used in a prototype design (see sections 5 and 4). Based on fabricated prototypes, the estimated cost for a 2 to 3 kW engine can easily be \$0.20/W or even less, considering economies of scale. Simple design changes can reduce the amount of copper used. The metals content of the engine can be reduced by replacing most metallic parts with plastics, which will further reduce the contribution of the engine to the overall system cost. Further, power density can be increased, resulting in additional cost reduction. Thus, an argument can be made for a complete system cost (collector and engine) in the range of \$0.80/W.

2.5 Conclusions

A promising case was outlined for the use of distributed solar-thermal-electric generation, based on low temperature-differential Stirling engine technology in conjunction with state-of-the-art solar thermal collectors. Although the predicted efficiencies are modest, the estimated cost in \$/W for large scale manufacturing of these systems is quite attractive in relation to conventional photovoltaic technology.

Nonimaging CPC collectors have the potential to provide temperatures of about 220 °C at 50% solar to thermal efficiency [38]. This temperature can raise the overall system efficiency up to 14%. The modular nature of such collectors could drastically reduce the installation costs that is a serious hurdle for PV industry. In addition, by sacrificing a little bit of efficiency, the Stirling engine can reject heat at 50-60 °C and produce hot water without a large capital cost for residential applications.

Chapter 3

Stirling Cycle and Non-Idealities

3.1 Introduction

A Stirling engine cycles through four main processes: cooling, compression, heating and expansion. Ideally, the thermodynamic cycle will be equivalent to a Carnot cycle and will achieve the highest possible thermodynamic efficiency. However, the actual cycle diverts from its ideal model and exhibits lower output power and lower efficiency due to non-idealities in engine components such as heat exchangers (heater, cooler, and regenerator), and in the main processes such as expansion and compression. With a firm understanding of all the major non-idealities, one can design an engine that operates as close to the Carnot cycle as possible by minimizing the non-ideal effects.

Non-idealities of heater, cooler, and regenerator will be discussed in this chapter as the three essential components of Stirling engines. Gas spring hysteresis loss (or compression loss) will be discussed as well. Gas spring hysteresis loss may prove to be a serious complication and may impede the successful operation of low-pressure and low-temperature

Stirling engines. Enthalpy loss through the clearance seals of a reciprocating piston will also be discussed, followed by the effect of thermal conduction on engine performance.

3.2 Heat Exchangers

“Heat exchanger” is a broad name for the heater, cooler, or regenerator in Stirling engine. The heater is responsible for transferring heat from outside of the engine chamber to the working fluid, whereas the cooler transfers the thermal power in the opposite direction. The regenerator, however, absorbs heat from the working fluid when the fluid flows from heater to cooler, and releases heat during the reverse process. Fluid flow through heat exchangers is an irreversible phenomenon that requires “pumping power” to overcome the viscous friction involved. The required pumping power is supplied as a fraction of the available mechanical output power and, hence, is a source of loss. Heat exchangers also contribute to the dead volume of the engine which, in turn, reduces the nominal output power by reducing the compression ratio.

3.2.1 Fluid Flow Dissipation

Unidirectional Flow

The unidirectional flow regime is the classical approach for studying the pressure drop across heat exchangers and corresponding flow dissipation as discussed in [39, 40]. In this approach, the pressure drop, Δp , is computed as,

$$\Delta p = \frac{\rho}{2} f \frac{L}{D_h} u^2 = \frac{\rho}{2A_o^2} f \frac{L}{D_h} \dot{V}^2 \quad (3.1)$$

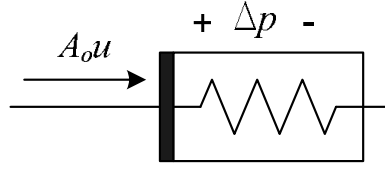


Figure 3.1: Nonlinear resistor model for fluid flow through heat exchangers.

where ρ is the fluid density, f is friction factor, L is length of the heat exchanger measured along the flow direction, D_h is hydraulic diameter of the heat exchanger, u is the fluid velocity, A_o is the open area of the heat exchanger through which the fluid flows, and \dot{V} is its volumetric flow rate. Both hydraulic diameter and friction factor are functions of the heat exchanger geometry. Friction factor data is usually obtained by empirical methods. It is presented either as a graph or as a mathematical expression of the form,

$$f = \frac{C_{sf}}{Re} + C_{fd} \quad (3.2)$$

where C_{sf} and C_{fd} are, respectively, the *skin friction* and *form drag* correlation constants and Re is the Reynolds number; a dimensionless quantity which combines the flow characteristics (velocity) with heat exchanger geometry (hydraulic diameter) and fluid properties (viscosity) and is defined as,

$$Re = \frac{\rho}{\mu} D_h u = \frac{1}{\nu} D_h u \quad (3.3)$$

where μ is dynamic viscosity of the fluid and ν is its kinetic (or kinematic) viscosity.

As shown in Figure 3.1, fluid flow dissipation can be modeled as a nonlinear resistor. In this model, the pressure drop and volumetric flow rate are analogue to voltage and current,

respectively. Combining Eqs. (3.1)-(3.3) we have,

$$\Delta p = \frac{1}{2} \left(\mu C_{sf} \frac{u}{D_h^2} + \rho C_{fd} \frac{u^2}{D_h} \right) L \quad (3.4)$$

Therefore, fluid friction dissipation (viscous dissipation or fluid pumping power), \dot{W}_{flow} , is simply calculated as,

$$\dot{W}_{flow} = \Delta p \dot{V} = \Delta p A_o u = \frac{A_o}{2} \left(\mu C_{sf} \frac{u^2}{D_h^2} + \rho C_{fd} \frac{u^3}{D_h} \right) L \quad (3.5)$$

Equation (3.5) highlights the relationship between fluid flow dissipation and design parameters such as flow velocity, heat exchanger hydraulic diameter, and its length. In Stirling engines, fluid flow through the heat exchangers is laminar which corresponds to low Reynolds numbers. Therefore, both velocity and hydraulic diameter have quadratic effect on fluid flow dissipation.

Oscillatory Flow

In a Stirling engine, the displacer piston shuttles a certain volume of working fluid known as swept volume, V_{sw} , back and forth through all the heat exchangers at frequency of $\omega = 2\pi/T$. In other words,

$$V(t) = \frac{V_{sw}}{2} \sin(\omega t) + V_0 \quad (3.6)$$

where V_0 represents the unswept or dead volume. Assuming no phase delay between volumetric flow rate (or fluid velocity) and pressure drop across the heat exchanger, $\Delta p(t)$, we

have,

$$\Delta p(t) = \Delta p_{max} \cos(\omega t) \quad (3.7)$$

and mean flow dissipation in an oscillatory flow regime is calculated as,

$$\overline{\dot{W}_{flow}} = \frac{1}{T} \int_T \Delta p(t) dV(t) = \frac{A_o}{2} \Delta p_{max} u_{max} \quad (3.8)$$

where u_{max} is the peak fluid velocity defined as,

$$u_{max} = \frac{1}{A_o} \dot{V}_{max} = \frac{1}{A_o} \frac{V_{sw}\omega}{2} \quad (3.9)$$

Unlike unidirectional flow, there is no classical approach for calculating pressure drop across heat exchangers in an oscillatory flow regime to replace Eq. (3.7). All published correlations, i.e., formulations for friction factor, f , under oscillatory flow, are based on empirical data and the implemented methodologies are not quite similar to one another [41, 42, 43, 44, 45]. The cycle-averaged pressure drop of the oscillatory flow is usually four to six times higher than that of a unidirectional steady flow at the same Reynolds number based on the cross-sectional mean velocity [43].

Since the regenerator often has the highest contribution of fluid flow dissipation in a Stirling machine (compared to heater and cooler), all the referenced publications narrowed their focus down to this element. However, since they incorporate characteristic dimensions such as hydraulic diameter and dimensionless quantities such as Reynolds number, their methodologies could be extended to other heat exchangers as well. A range of correlations are compared in [46] and updated in [47]. Tanaka et al. [41] studied oscillatory

flow through stacks of wire screens, sponge metal, and sintered metal as possible choices for the regenerator material of a Stirling engine [41]. They chose air as the working fluid and conducted a series of experiments on fluid flow friction at room temperature, various frequencies, and a range of mean working pressures. Tanaka's methodology is very similar to the classical approach for unidirectional steady flow and his suggested correlations are reported to produce conservative results. In his approach, maximum pressure drop, Δp_{max} , is calculated as,

$$\Delta p_{max} = \frac{\rho}{2} f_{max} \frac{L}{D_h} u_{max}^2 = \frac{\rho}{2A_o^2} f_{max} \frac{L}{D_h} \dot{V}_{max}^2 \quad (3.10)$$

where

$$f_{max} = \frac{C_{sf}}{Re_{max}} + C_{fd} \quad (3.11)$$

$$Re_{max} = \frac{\rho}{\mu} D_h u_{max} = \frac{1}{\nu} D_h u_{max} \quad (3.12)$$

Appropriate substitutions in Eqs. (3.10)-(3.12) result in the maximum pressure drop as below,

$$\Delta p_{max} = \frac{1}{2} \left(\mu C_{sf} \frac{u_{max}}{D_h^2} + \rho C_{fd} \frac{u_{max}^2}{D_h} \right) L \quad (3.13)$$

Hence, the mean flow dissipation is computed as,

$$\overline{\dot{W}_{flow}} = \frac{A_o}{4} \left(\mu C_{sf} \frac{u_{max}^2}{D_h^2} + \rho C_{fd} \frac{u_{max}^3}{D_h} \right) L \quad (3.14)$$

Tanaka's empirical formulation suggests $C_{sf} = 175$ and $C_{fd} = 1.6$ for stacks of screens. According to reference [39], the average values for C_{sf} and C_{fd} in a unidirectional flow are 172 and 2, respectively.

Zhao, however, has a different approach in evaluation of pressure drop through a pack

of woven screens in an oscillatory flow [43]. He defines

$$f_{max} = \frac{A_o D_h}{V_{sw}} \left(\frac{C_{sf}}{Re_\omega} + C_{fd} \right) \quad (3.15)$$

where Re_ω is the kinetic Reynolds number which is defined as,

$$Re_\omega = \frac{\rho}{\mu} D_h^2 \omega \quad (3.16)$$

Therefore, the maximum pressure drop in his approach is,

$$\Delta p_{max} = \frac{1}{2} \left(\mu \frac{C_{sf}}{2} \frac{u_{max}}{D_h^2} + \rho \frac{C_{fd}}{2} u_{max} \omega \right) L \quad (3.17)$$

By comparing Eqs. (3.13) and (3.17) one can expect that the coefficient C_{sf} in Zhao's formulation to be about twice as large as its counterpart in Tanaka's formulation.

Based on the above discussion, the mean flow dissipation in Zhao's approach is,

$$\overline{\dot{W}_{flow}} = \frac{A_o}{4} \left(\mu \frac{C_{sf}}{2} \frac{u_{max}^2}{D_h^2} + \rho \frac{C_{fd}}{2} u_{max}^2 \omega \right) L \quad (3.18)$$

for which Zhao suggests $C_{sf} = 403.2$ and $C_{fd} = 1789.1$.

As mentioned, both Tanaka and Zhao focused on regenerator materials (i.e., screens) in their studies. For heater and cooler, however, various arrangements of tubes, ducts, finned tubes, or plate-fin surfaces are appropriate candidates. For such geometries, in this dissertation, Tanaka's methodology is implemented to estimate maximum pressure drop along heat exchanger and associated tubing by replacing f_{max} in Eq. (3.10) with the friction factor data published in [39] and [40] that correspond to Tanaka's definition of

Table 3.1: Comparison of the calculated and measured fluid flow dissipations for the heat exchangers and tubing of the two fabricated Stirling engine prototypes. Two measurement methodologies are implemented: ring-down (RD) and energy-balance (EB) tests. Dissipations are expressed in Watts.

Heat exchanger type	D_h m	ω rad/s	A_o m ²	L m	Calculated			Measured	
					Tanaka	Zhao	Artin	RD	EB
Single-phase Stirling engine prototype $V_{sw}=9.88\text{E-}4 \text{ m}^3$									
Connector/Tube	2.0E-2	18.85	6.5E-4	0.76	-	-	1.3	1.6	1.8
Heater/Duct	6.2E-4	18.85	7.1E-3	0.008	-	-	0.15	-	-
Cooler/Duct	4.9E-4	18.85	5.9E-3	0.008	-	-	0.10	-	-
Regenerator/Screen	2.0E-4	18.85	1.6E-2	0.006	0.78	0.98	-	-	-
All heat exchangers	-				1.03 – 1.23			1.1	0.49
Three-phase Stirling engine prototype $V_{sw}=1.6\text{E-}4 \text{ m}^3$									
Heater/Screen	7.7E-4	47.12	5.2E-3	0.01	0.05	0.4	-	0.07	-
Regenerator/Screen	1.6E-4	47.12	4.3E-3	0.01	1.16	1.66	-	0.15	-
Heater/Screen	7.7E-4	74.77	5.2E-3	0.01	0.15	1.5	-	0.07	-
Regenerator/Screen	1.6E-4	74.77	4.3E-3	0.01	3.1	4.8	-	0.65	-

Re_{max} given in Eq. (3.12). The effect of abrupt contraction and expansion is also included in this model as recommended in [39].

The design, fabrication, and assessment results of two Stirling engine prototypes are discussed in chapters 4 and 5. For the single-phase engine of chapter 4, finned tubes are implemented as heater and cooler, whereas a stack of wire screens is utilized as regenerator. However, for the three-phase engine of chapter 5, wire screens are utilized as heater, cooler, and regenerator. Table 3.1 summarizes the estimated flow friction dissipation at the heat exchangers of each prototype and compares them with the measurements. Measurements are based on either ring-down (RD) or energy-balance (EB) tests, which are described in the corresponding chapters. The swept volume is set by the prototype dimensions and is specified for each machine. As seen above, fluid flow dissipation is a function of the heat exchanger hydraulic diameter D_h , operating frequency ω , open area A_o , and length L , which are specified for each component in Table 3.1. Experiments for the single-phase prototype are carried out at its 3 Hz operating frequency, whereas the three-phase

prototype is tested at two frequencies of 7.5 Hz and 11.9 Hz. The tabulated data show that Tanaka's formulation estimates higher fluid flow dissipations as compared to measured data and Zhao's methodology is even more conservative. Table 3.1 further shows (one data point only) that the adopted methodology (Artin) for "non-screen" heat exchangers could generate estimations very close to the measured data and it could be a good practice to scale the estimated values up by a factor of 1.5 when utilizing the latter methodology to avoid undesired surprises.

3.2.2 Heat Transfer

In addition to low viscous dissipation, a good heat exchanger should provide enough surface area to transfer the required heat to the working fluid with the least possible temperature drop. The difference between heat exchanger wall temperature, T_w and the temperature of the working fluid that passes through the heat exchanger, T , is expressed in terms of transferred thermal power, \dot{Q} , forced convection heat transfer coefficient, h , and total wetted area, A_w , as,

$$\Delta T = T_w - T = \frac{\dot{Q}}{A_w h} \quad (3.19)$$

The heat transfer coefficient is computed as,

$$h = \frac{Nu \cdot k}{D_h} \quad (3.20)$$

where k is the thermal conductivity of the working fluid and Nu is a dimensionless quantity known as the Nusselt number. Like the friction factor, the Nusselt number is measured experimentally and presented either as a graph or as an algebraic expression for various

heat exchanger geometries. The heat transfer coefficient is reported to be significantly higher in an oscillating flow regime as compared to in an unidirectional flow [42].

The mean Nusselt number is usually expressed as,

$$Nu = \left(C_1 + C_2 (Re_{ave} Pr)^{C_3} \right) (1 - C_4 (1 - \varepsilon)) \quad (3.21)$$

where C_1 , C_2 , C_3 , and C_4 are constant quantities which are calculated based on experimental results, ε is the screen porosity, Pr is the Prandtl number, and,

$$Re_{ave} = \frac{\rho}{\mu} D_h u_{ave} = \frac{1}{\nu} D_h u_{ave} \quad (3.22)$$

$$u_{ave} = \frac{2}{\pi} u_{max} = \frac{1}{A_o} \frac{V_{sw} \omega}{\pi} \quad (3.23)$$

The Prandtl number is another dimensionless quantity which approximates the ratio of momentum diffusivity (viscosity), ν , and thermal diffusivity, α , and is defined as,

$$Pr = \frac{\nu}{\alpha} = \frac{\mu/\rho}{k/(\rho c_p)} = c_p \frac{\mu}{k} \quad (3.24)$$

where c_p is the specific heat at constant pressure. Prandtl number is approximately 0.7 for air and many other gases.

Tanaka's experiments, which are based on instantaneous temperature measurements in one cycle, suggest the following values for the coefficients in Eq. (3.21):

$$C_1 = C_4 = 0, \quad C_2 = 0.42, \quad C_3 = 0.67 \quad (3.25)$$

Table 3.2: Comparison of calculated heat transfer behavior for the heat exchangers of the two fabricated Stirling engine prototypes.

Heat exchanger type	D_h m	ω rad/s	A_o m ²	A_w m ²	ε , % %	Calc. h , W/m ² K		
						Tanaka	Thomas	Artin
Single-phase Stirling engine prototype $V_{sw}=9.88\text{E-}4 \text{ m}^3$								
Heater/Duct	6.2E-4	18.85	7.1E-3	3.5E-1	27	-	-	292
Cooler/Duct	4.9E-4	18.85	5.9E-3	3.7E-1	23	-	-	369
Regenerator/Screen	2.0E-4	18.85	1.6E-2	1.4	63	119	236	-
Three-phase Stirling engine prototype $V_{sw}=1.6\text{E-}4 \text{ m}^3$								
Heater/Screen	7.7E-4	47.12	5.2E-3	1.5E-1	64	89	135	-
Regenerator/Screen	1.6E-4	47.12	4.3E-3	6.1E-1	53	169	281	-
Heater/Screen	7.7E-4	74.77	5.2E-3	1.5E-1	64	121	176	-
Regenerator/Screen	1.6E-4	74.77	4.3E-3	6.1E-1	53	230	348	-

Isshiki reports experimental data which are in accord with Tanaka's results [44]. However, in reference [47] Bernd Thomas states that, compared to other empirical correlations he investigated, Tanaka's methodology results in the lowest Nusselt number. Therefore, reference [47] suggests,

$$C_1 = 1.010, C_2 = 0.790, C_3 = 0.662, C_4 = 0.845 \quad (3.26)$$

which are based on Gedeon's experiments reported in [48]. Thomas' correlation gives an upper bound (as high as 2.5 times that of Tanaka's correlation) for the Nusselt number and, hence, should be utilized with caution.

There is no heat transfer data in the literature that is suitable for geometries other than woven screen or metal felts in an oscillatory flow regime. To estimate the convective heat transfer coefficient of the heater and cooler, Tanaka's methodology is implemented in this dissertation by replacing Nu in Eq. (3.20) with the corresponding data published in [39] and [40] that correspond to Re_{ave} defined in Eq. (3.22).

Table 3.2 summarizes the calculated heat transfer coefficients for the heat exchangers

of both the single-phase and the three-phase prototypes. Note that the heat transfer coefficient for the regenerators may appear to be smaller than the heat exchangers but the regenerators have considerably larger wetted areas which scale up the overall heat transfer characteristic of these components and increase their effectiveness, as discussed in the sequel.

3.2.3 Regenerator Effectiveness

The regenerator is a counterflow heat exchanger. However, unlike conventional heat exchangers, it does not involve two distinct working fluids as “hot stream” and “cold stream.” In addition, heat transfer from the hot stream to the regenerator material and then to the cold stream does not happen simultaneously. During the first half of the cycle, the hot stream (i.e., the working fluid coming from the heater) enters the regenerator at a high temperature, $T_{h,in}$, and leaves at much lower temperature, $T_{h,out}$. During this process, the regenerator temperature profile is slightly lower than the hot stream temperature profile. Hence, the regenerator absorbs some heat and stores it for the next half of the cycle. During the second half of the cycle, the cold stream (i.e., the working fluid coming from the cooler) enters the regenerator at a low temperature, $T_{k,in}$. The regenerator temperature profile is slightly higher in this case allowing the regenerator material to return most of the stored heat to heat up the working fluid and raise its temperature to $T_{k,out}$ as it leaves the heat exchanger. Figure 3.2 depicts the regenerator temperature profile with respect to the working fluid temperature for a complete operating cycle.

The regenerator effectiveness, ϵ , compares the actual heat transfer rate, \dot{Q} , to the maximum possible heat transfer rate, \dot{Q}_{max} , as would be realized only in a counterflow

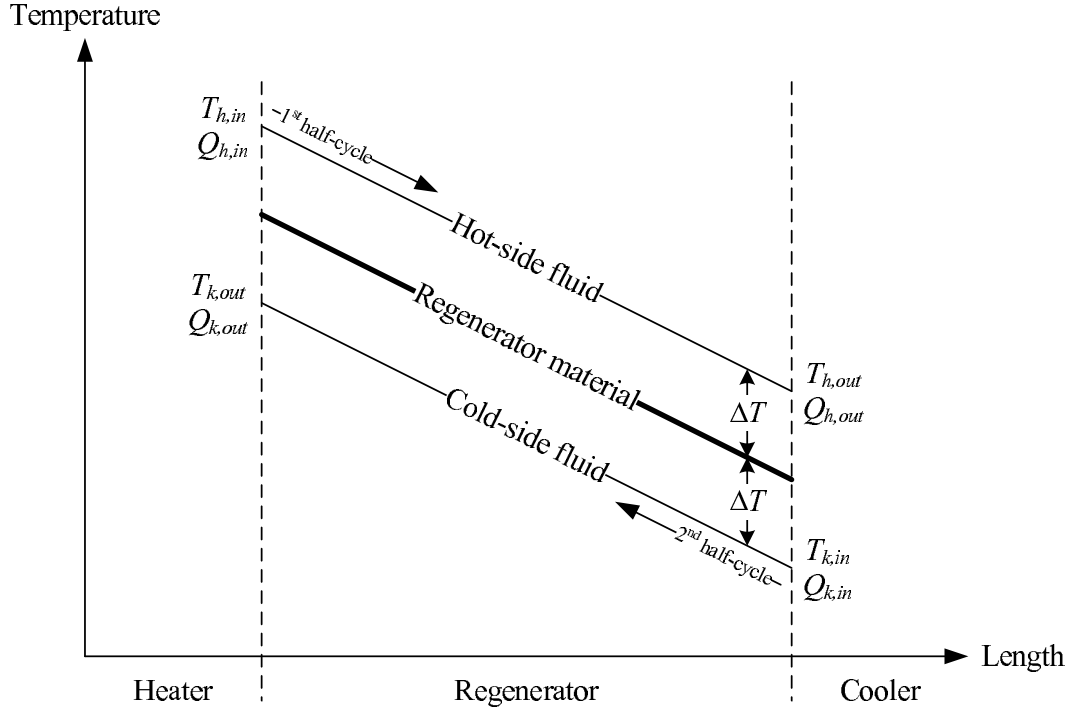


Figure 3.2: Regenerator temperature profile with respect to the working fluid temperatures.

heat exchanger of infinite heat transfer area [39]. Therefore,

$$\epsilon = \frac{\dot{Q}}{\dot{Q}_{max}} = \frac{\dot{Q}_{h,in} - \dot{Q}_{h,out}}{\dot{Q}_{h,in} - \dot{Q}_{k,in}} = \frac{C_h (T_{h,in} - T_{h,out})}{C_{min} (T_{h,in} - T_{k,in})} = \frac{C_k (T_{k,out} - T_{k,in})}{C_{min} (T_{h,in} - T_{k,in})} \quad (3.27)$$

where C_h and C_k are, respectively, the bulk heat capacities of the hot stream and cold stream fluids, C_{min} is the smaller of the C_h and C_k magnitudes, and all other parameters are specified on Figure 3.2. For the Stirling engine regenerator we have $C_h = C_k$ and Eq. (3.27), which defines thermodynamic effectiveness, reduces to the thermal effectiveness, as follows,

$$\epsilon = \frac{T_{h,in} - T_{h,out}}{T_{h,in} - T_{k,in}} = \frac{1}{1 + 2\Delta T / (T_{h,in} - T_{h,out})} \quad (3.28)$$

For an adiabatic regenerator, the change in enthalpy of the hot stream is equal to the transferred heat from the hot stream to the regenerator material. Referring to Figure 3.2

and Eq. (3.19), this fact is expressed by the following simple identity:

$$\dot{m}_{ave}c_p(T_{h,in} - T_{h,out}) = A_w h \Delta T \quad (3.29)$$

where \dot{m}_{ave} is the average mass flow rate and is calculated as,

$$\dot{m}_{ave} = \rho A_o u_{ave} \quad (3.30)$$

To simplify the final expression for the regenerator effectiveness, a dimensionless quantity is introduced which is known as Number of Transfer Units,

$$NTU = \frac{A_w h}{\dot{m}_{ave}c_p} = \frac{T_{h,in} - T_{h,out}}{\Delta T} \quad (3.31)$$

By combining Eqs. (3.28)-(3.31), the regenerator effectiveness is expressed as,

$$\epsilon = \frac{NTU}{NTU + 2} \quad (3.32)$$

The regenerator ineffectiveness exercises an additional thermal burden on the heater and cooler. This additional heat is known as the regenerator heat transfer loss, \dot{Q}_{loss} , and can be quantified as the difference between the heat of inflow and the heat of outflow at the regenerator cold end [41].

$$\dot{Q}_{loss} = \dot{Q}_{h,out} - \dot{Q}_{k,in} = (1 - \epsilon)(\dot{Q}_{h,in} - \dot{Q}_{k,in}) = (1 - \epsilon)c_p \dot{m}_{ave} \Delta T_{r,ave} \quad (3.33)$$

where $\Delta T_{r,ave}$ is the average temperature difference across the regenerator.

3.3 Gas Spring Hysteresis

The Stirling thermodynamic cycle undergoes both pressure and volume variations. Since it is a closed cycle, the Stirling engine chamber functions as a gas spring to the power piston (Beta-type and Gamma-type engines) or both displacer and power pistons (Alpha-type engine). Since the thermodynamic process that occurs in a gas spring is not perfectly reversible, there is a certain amount of pV work dissipated over each cycle which is known as gas spring hysteresis loss and is a function of the viscous and temperature gradient effects present in the engine chamber. The viscous effects do not contribute in a significant way and are usually neglected [33]. This loss manifests itself as a reduction in engine pV work and an increased heat rejection (not necessarily from the cooler) and is numerically equal to the heat transfer across the engine chamber walls. Reference [33] offers an approximate but accurate calculation for gas spring hysteresis loss.

Assuming sinusoidal variations for the Stirling engine chamber volume,

$$V_{tot} = V_o + V_m \sin(\omega t) \quad (3.34)$$

the average gas spring hysteresis loss, $\overline{\dot{W}_{hys}}$, is approximated by the following expression,

$$\overline{\dot{W}_{hys}} \simeq \sqrt{\frac{1}{32} \omega \gamma^3 (\gamma - 1) T_w p_{mean} k} \left(\frac{V_m}{V_o} \right)^2 A_w \quad (3.35)$$

where $\gamma = c_p/c_V$ is the ratio of the gas specific heat at constant pressure to the gas specific heat at constant volume, T_w is the chamber wall temperature that is assumed to be constant (constant temperature boundary condition), p_{mean} is the mean chamber pressure, and A_w

is the wetted area, i.e., the area in contact with the enclosed gas.

To minimize the gas spring hysteresis loss, the fractional volumetric variation, $\frac{V_m}{V_o}$, and the wetted area should be kept small. Note that the output power of a Stirling engine is proportional to the mean pressure of the working fluid. However, the gas spring hysteresis dissipation is proportional to the root of that pressure. Therefore, increasing the working fluid pressure is a good strategy to decrease the relative dissipation of the gas spring hysteresis. On the other hand, by increasing the engine dimensions (e.g., piston diameters and their excursions), the areas and volumes will increase at quadratic and cubic rates, respectively. This suggests another good strategy to tackle the gas spring hysteresis, since the output power of the cycle is proportional to the displacer swept volume and the gas spring hysteresis loss is proportional to the engine chamber area. Therefore, for most large machines (1 kW and above) the gas spring hysteresis loss is usually negligible when compared with the output power [33].

The damping effect of gas spring hysteresis loss is modeled as a linear damping dissipation. For a piston that oscillates at angular velocity of ω , amplitude of x_m , and has cross sectional area of A_P , we have,

$$V_m = A_P x_m \quad (3.36)$$

Therefore, the linear damping factor associated with gas spring hysteresis, D_{hys} , is calculated as,

$$D_{hys} = \sqrt{\frac{1}{8} \omega^{-3} \gamma^3 (\gamma - 1) T_w p_{mean} k} \left(\frac{A_P}{V_o} \right)^2 A_w \quad (3.37)$$

The fabricated three-phase prototype (chapter 5) has been tested to verify the gas hysteresis dissipation model. The system was tested at the frequency of the pure compres-

Table 3.3: Comparison of measured and calculated gas hysteresis (compression) losses in various conditions. The number in the left three columns indicate the fraction of corresponding heat exchanger screens that is in place.

Heater	Cooler	Regen.	f , Hz	Piston stroke, mm	Calc. $\overline{\dot{W}}_{hys}$, W	Meas. $\overline{\dot{W}}_{hys}$, W
0%	0%	0%	28.2	12	2	2.3
50%	50%	0%	29.2	12	2.6	2.6
100%	100%	0%	29.6	13	3.7	3.7
50%	50%	50%	30	6	0.7	0.7

sion mode which is about 30 Hz. Four different conditions are considered and tested as tabulated in Table 3.3. In each case, a slightly different resonant frequency is observed for the compression mode that is due to the different volume of enclosed gas within the engine chamber. In Table 3.3 the measured gas spring hysteresis loss is compared with the model suggested in Eq. (3.35). This result confirms the accuracy of the model and provides a reliable basis for estimation of the gas hysteresis losses.

3.4 Clearance Seal Leakage

For reciprocating pistons of a Stirling engine, a clearance seal is a good alternative to conventional ring type seals. A clearance seal obviates rubbing surfaces and lubrication requirements. Obviously, due to the inherent clearance, this type of seal will leak to some degree. Therefore, thermodynamic effects of this leakage are important to the design. Clearance seals are usually placed on the cold side of the Stirling engine to avoid undesirable temperature-related effects. Consider a piston that is surrounded by a seal with clearance of g . If the instantaneous pressures on either side of the piston are p_a and p_b , the instantaneous mass flow rate, \dot{m}_l , is calculated as [33],

$$\dot{m}_l = \pi D \frac{p_a + p_b}{4RT_g} \left(\dot{x}_{Pg} - \frac{g^3}{6\mu} \frac{p_b - p_a}{L} \right) \quad (3.38)$$

where D is the mean clearance diameter, T_g is the gas temperature which would be near constant at the wall temperature, L is the seal length, and x_P is the instantaneous piston position. Note that Eq. (3.38) incorporates both pressure-driven and shear-driven leakages. In addition to leakage, Eq. (3.38) can be utilized to predict instantaneous or mean enthalpy transfer through the seal using,

$$\dot{H}_l = \dot{m}_l c_p T \quad (3.39)$$

where T is the conditional nodal temperature at the point of application, depending on the gas flow direction.

3.5 Conduction Loss

Conduction is another loss mechanism that will be discussed in this chapter. Since Stirling engines incorporate a hot side (heater and expansion space) and a cold side (cooler and compression space), there are chances of direct conductive heat flow from the hot side to the cold side that should be identified and minimized. As a result of direct heat conduction, there is an increased thermal burden upon heater and cooler, which in turn, decreases the overall efficiency of the Stirling engine. The conduction loss, Q_{cond} , in its simple form, is calculated as,

$$\dot{Q}_{cond} = k \frac{A}{L} \Delta T \quad (3.40)$$

where k is the conductivity of the material through which heat conduction occurs, A is the effective cross sectional area normal to the heat flow path, L is the effective length of heat conduction path, and ΔT is the temperature difference across the conduction path.

Since there is a substantial temperature difference across displacer piston, this element

could provide a substantial heat leakage path, if not designed properly. Regenerator is subject to almost the same temperature difference as displacer piston. However, since it is made of porous material (woven screens, metal felts, etc.) the effective heat conduction area is considerably small, causing a minimal direct heat flow through regenerator. Any other direct path between hot side and cold side of the engine (e.g., heat exchanger housing) can be a potential source of heat loss and should be addressed properly.

3.6 Conclusions

In this chapter, the most significant non-ideal phenomena that can degrade the performance of a Stirling engines were highlighted and discussed. Fluid flow dissipation at heat exchangers, temperature drop at heater and cooler, the regenerator ineffectiveness, gas spring hysteresis loss, clearance seal leakage, and direct conduction were among parasitic losses that were presented. In each case, appropriate mathematical models were introduced which could be incorporated in design spreadsheets or computer simulations. Figure 3.3 summarizes the discussion of this chapter and depicts the energy balance diagram of a typical Stirling engine showing how each parasitic loss affects the output power or efficiency of the engine.

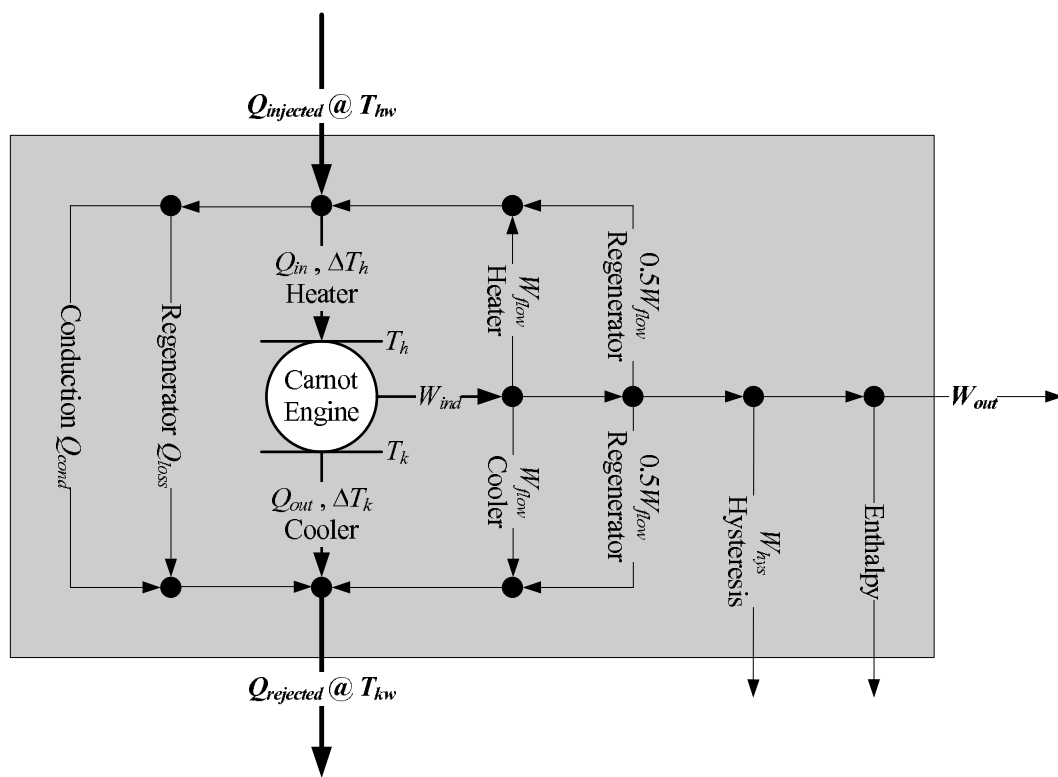


Figure 3.3: Energy balance diagram for a Stirling engine.

Chapter 4

Single-Phase Stirling Engine

Prototype

4.1 Introduction

Design, fabrication and test results of a gamma-type free-piston Stirling engine are discussed in this chapter. The design of a very low-loss resonant displacer piston, the heat exchangers, and the power piston, as the key components, is elaborated. This prototype is a low-power engine that utilizes ambient pressure air as its working fluid. It is designed to assess the details of Stirling cycle operation and to confirm the design models of all the key components and to assess the possible manufacturing procedures.

First, the description of the overall engine design will be delineated through simulation results. Design of the displacer piston and the heat exchangers are presented next and are compared with measurements in detail. The final section describes the assessment of the fabricated prototype engine while in operation. The data supports the models and

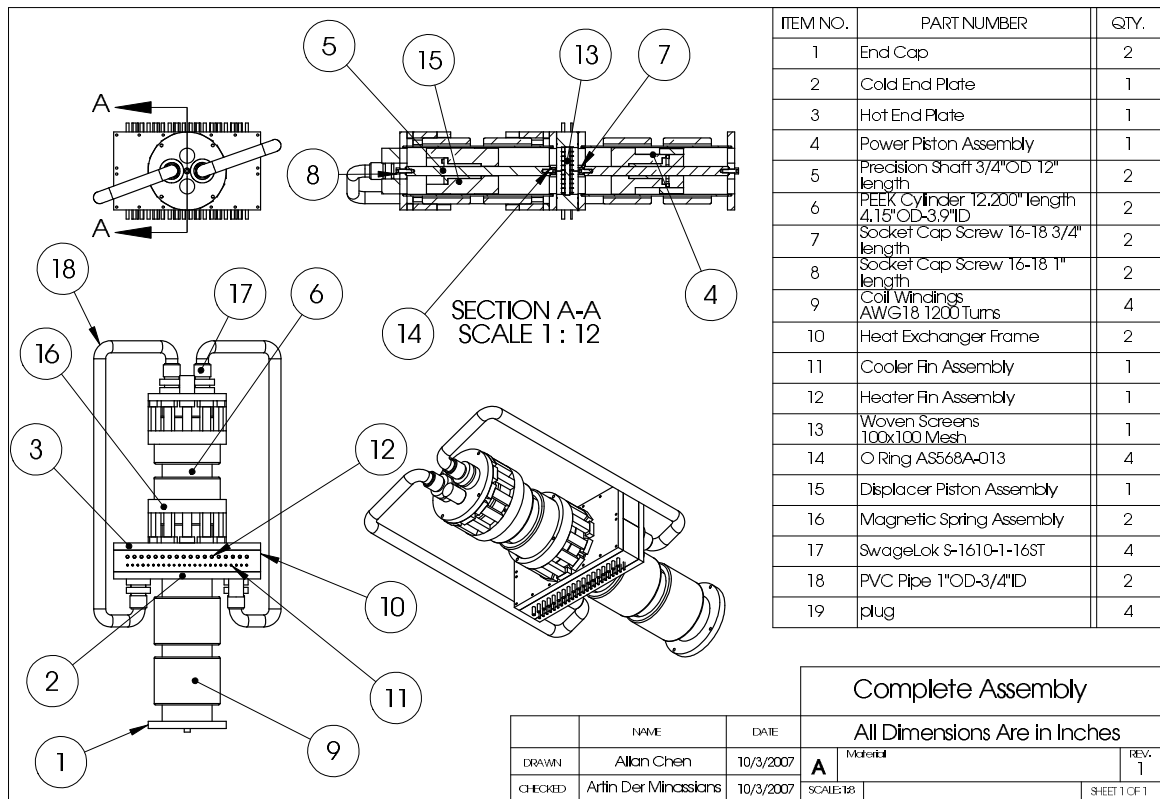


Figure 4.1: Complete assembly drawing of the single-phase free-piston Stirling engine design.

assumptions.

4.2 Design and Thermodynamic Simulation

Figure 4.1 illustrates the complete assembly drawing and the components of the conceived single-phase free-piston Stirling engine design and Figure 4.2 depicts the simplified schematic diagram of the engine representing the pistons and heat exchanger configuration of the system. The gas circuit of the displacer subsystem is closed by means of tubing in order to provide a closed engine chamber. Both displacer and power piston have identical dimensions. In single-phase operation, the power piston interacts with ambient pressure on one side and engine chamber pressure on the other. To facilitate tight clearance sealing,

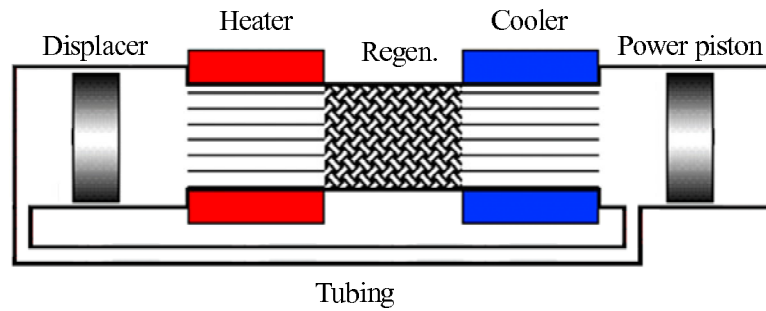


Figure 4.2: Simplified schematic diagram of the conceived Stirling engine.

and thus minimal enthalpy loss, the power piston is located on the cold side of the engine.

The engine design parameters are tabulated in Table 4.1. The displacer piston shuttles the working fluid, ambient pressure air, between expansion and compression spaces at the operating frequency of 3 Hz. Furthermore, the mass of the power piston has been chosen such that it resonates with the gas spring approximately at the operating frequency. When loaded, the power piston behaves as a low- Q resonating system. Thus, it does not require high precision in tuning of its resonant frequency. A dynamical simulation has been carried out using the Stirling engine adiabatic model [33]. Figure 4.3 shows the simulation results in terms of temperature and volume variations of the compression and expansion spaces as well as pressure variation of the engine chamber and the p - V diagram of the Stirling cycle. Based on this simulation, with 150 °C difference between hot and cold side average temperatures, the indicated output power of the engine is about 26.9 W at 9.4% thermal efficiency.

In the sequel, the design of the displacer piston, the heat exchanger, and the power piston subsystems are discussed in detail with an emphasis on the loss contribution of each element.

Table 4.1: Engine thermodynamic design parameters.

Operating temperatures	T_h^{ave} : 175 °C T_k^{ave} : 25 °C
Indicated powers	Schmidt analysis Input: 75.1 W Output: 25.2 W Adiabatic model Input: 253.6 W Output: 23.8 W
Heater	Housing volume: 210 cm ³ × 27.5% Hydraulic diameter: 0.6 mm Wetted area: 0.35 m ²
Cooler	Housing volume: 210 cm ³ × 23% Hydraulic diameter: 0.5 mm Wetted area: 0.37 m ²
Regenerator	Housing volume: 260 cm ³ × 63.4% Hydraulic diameter: 0.2 mm Wetted area: 1.9 m ²
Pistons	Diameter: 10 cm Stroke: 15 cm
Tubing	Volume: 500 cm ³ Hydraulic diameter: 19 mm

4.3 Design

4.3.1 Displacer Subsystem

The displacer is designed as a reciprocating piston that moves along a shaft with stroke of 15 cm. It is in contact with hot gas (as high as 200 °C) at one end and cold gas (about 30 °C) at the other as shown in Figure 4.4. Thus, in addition to enduring the higher temperature, the displacer body material should minimize the heat leakage path between hot and cold spaces. In order to fulfill both requirements, among high-

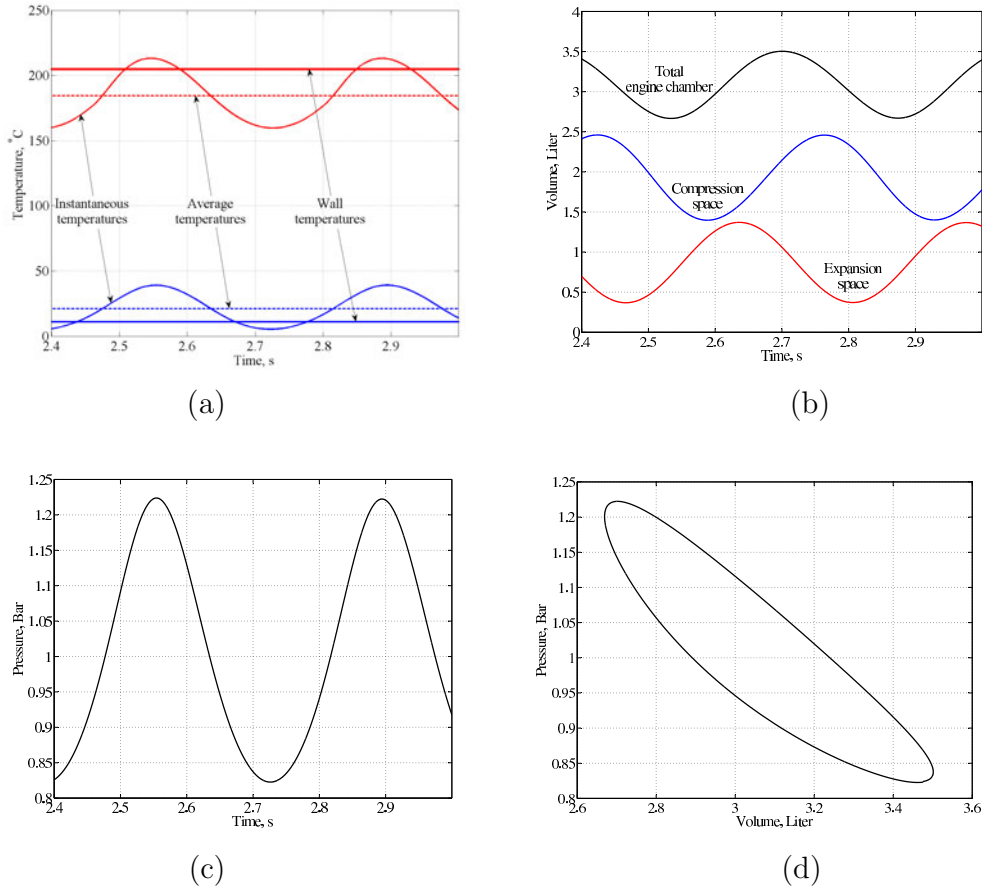


Figure 4.3: Simulation results of the single-phase free-piston Stirling engine thermodynamic behavior. (a) Wall, instantaneous, and average temperatures on hot and cold sides. (b) Expansion space, compression space, and total engine chamber volume variations. (c) Pressure variation. (d) p - V loop of the thermodynamic cycle.

temperature plastics, Teflon (Polytetrafluoroethylene) and PEEK (Polyetheretherketone) appear to be good candidates. Both materials endure temperatures of up to 250 °C, and have a low thermal conductivity (0.25 W/mK). The heat leakage through the displacer piston is expected to be about 2 W, if fabricated from either of these plastics. For its superior machinability properties and higher tensile strength, PEEK is selected as the material of choice for fabrication of the displacer piston prototype.

The displacer piston is designed to resonate with a linear spring at the design frequency of operation (i.e., 3 Hz). Considering the limited life of mechanical springs and other

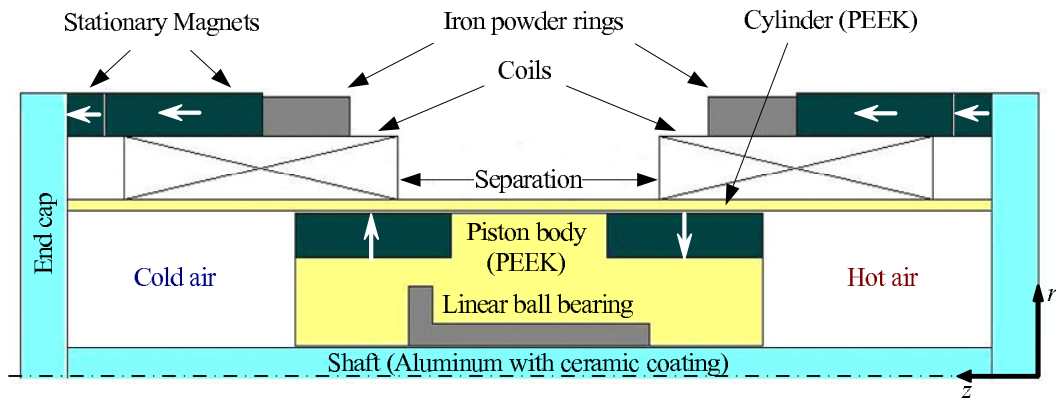


Figure 4.4: Schematic diagram of the displacer piston design.

challenges presented by these components, a design is carried out that utilizes magnetic springs to obviate mechanical failures and ensure long operation life. Permanent magnet arrays have been incorporated within the displacer piston to enable two magnetic functions: a magnetic spring and a linear motion magnetic actuator. To meet the above-mentioned thermal conditions, high coercivity 28/30 grade Sm-Co magnets have been designed to provide thermal stability. Sm-Co permanent magnets can typically be used up to 300 °C, and have coercivity temperature coefficient of -0.2% per °C.

As depicted in Figure 4.4, the displacer magnet array interacts with two stationary magnetic arrays to provide a linear spring function, which sets the mass-spring resonant frequency equal to the indicated frequency of operation. The displacer magnet array also interacts with a pair of stationary actuating coils to provide the actuation force required to control and sustain the resonant motion at its full excursion. The linear actuator is designed by mounting two rings of radially magnetized permanent magnets at each end of the piston and by placing two stationary coils with 1,200 turns each on the outer surface of the cylinder, outside of the thermodynamically active chamber. The axial positions of the coils can be adjusted along the length of the cylinder after system assembly, Figure 4.4,

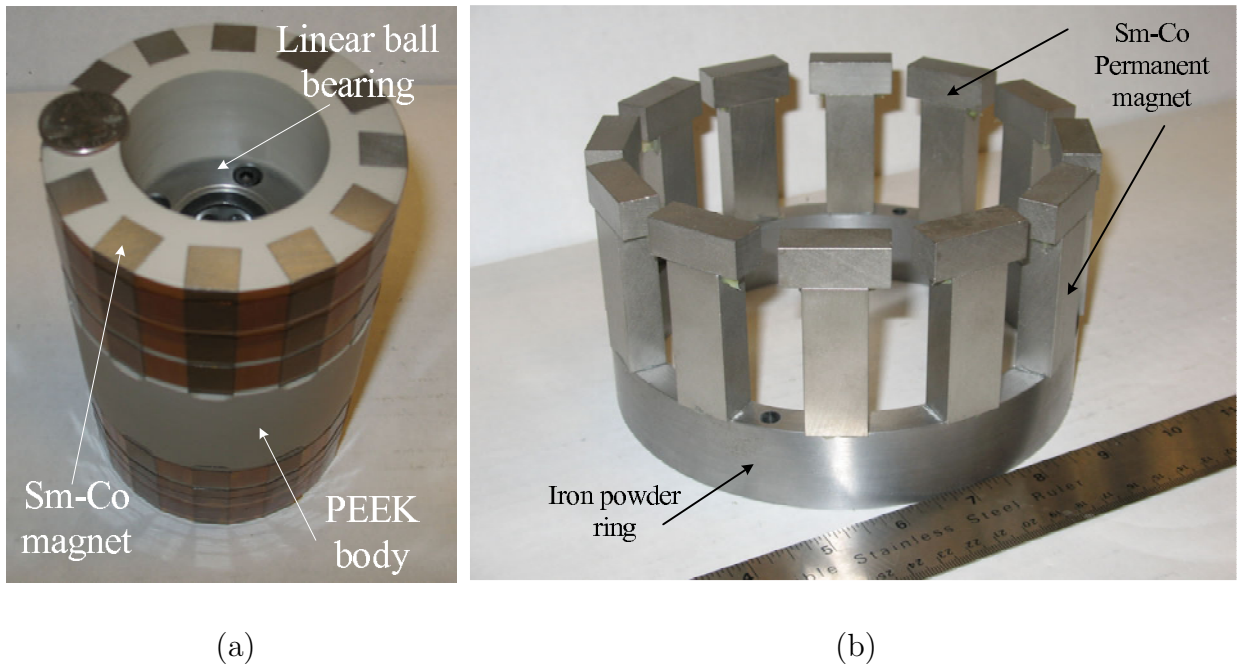


Figure 4.5: (a) Fabricated displacer piston with embedded linear motion ball bearing and permanent magnet arrays. (b) Stationary magnetic array that provides the linear spring function for the displacer. Compare to Figure 4.4

and final positions will be determined so as to maximize the actuator efficiency.

Due to the relative motion of the displacer piston with respect to the stationary cylinder and magnetic arrays, the piston and stationary components are exposed to alternating magnetic fields. Such magnetic fields generate eddy currents in any electrically conducting material, and hence, can significantly increase system losses. The choice of a non-conductive material completely obviates this phenomenon in the displacer body. Also, the high resistivity iron-powder ring is a proper solution as a component of the stationary magnet arrangement. On the contrary, Sm-Co magnets have high conductivity. Therefore, to minimize eddy losses, each magnet array is realized by separate block magnets in a circular pattern to prevent the formation of large eddy currents, mitigating corresponding potential losses. The realization of these arrangements is shown in Figure 4.5.

Magnetic spring designs are mostly made for very small strokes (e.g., 0.5 cm) [49, 50,

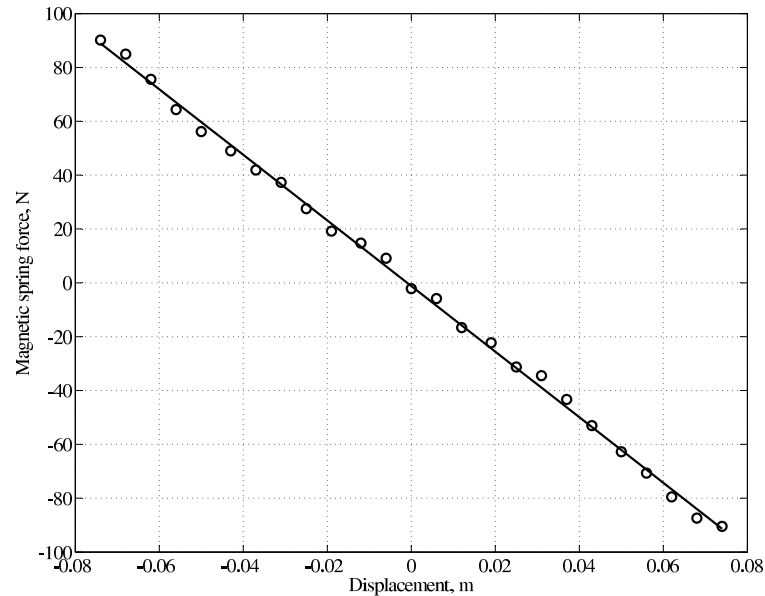


Figure 4.6: FEM analysis result for the stiffness characteristic of the magnetic spring. The straight line represents a linear regression fit through the data points (circles).

51]. All reported stiffness characteristics deviate from linear behavior at the two extremes of the stroke. In a nonlinear mass-spring system the resonant frequency is a function of the oscillation amplitude and may present serious challenges in tuning. Hence, in order to avoid complex tuning strategies, a stronger magnet section is added at the two end pieces of the stationary magnet setup to preserve the linear stiffness characteristic throughout the displacer piston stroke. Figure 4.5 shows how this idea is realized by implementing T-shaped magnets for wider magnets to provide more magnetic flux. A nonlinear finite-element analysis program, COMSOL¹, is utilized to determine the forces on different components of this system. Figure 4.6 shows the computed force-displacement characteristic. The correlation coefficient of a linear regression fit to the data points is 0.999, which indicates a very linear behavior throughout the extent of the displacer stroke.

An embedded linear motion ball bearing enables a low friction and smooth piston

¹<http://www.comsol.com>

motion. However, exposure of steel bearing balls to the surrounding magnetic fields impedes rolling. Hence, steel balls are replaced by non-magnetic ceramic (Silicon Nitride) balls. An average coefficient of friction for a linear motion ball bearing is between 0.002 and 0.004. This means an average power dissipation of 0.05 – 0.1 W for the nominal horizontal operating conditions of the displacer with a mass of about 2.9 kg.

The displacer cylinder has been fabricated out of PEEK as well. In addition to eliminating any potential eddy loss and allowing for minimal thermal leakage between hot and cold spaces, it is a good match with the piston in terms of thermal expansion considerations. As a result of the small pressure difference between the two ends of the displacer piston, due to fluid flow pressure drop through heat exchangers and tubing, clearance sealing is an appropriate way of separating the hot and cold air. At a relatively large clearance of 0.010 in. for the displacer piston, the average enthalpy loss is less than 4 W for a nominal temperature differential of 150 °C. This is negligible compared to 300 W of required engine input heat. The enthalpy loss may be further reduced by considering a tighter displacer clearance, if necessary, as described in section 3.4.

4.3.2 Heat Exchangers

Heater and cooler geometry, in this design, is based on a fin-tube structure that is fabricated by press-fitting tubes through stacks of etched metal fins, Figure 4.7. With hydraulic diameter of about 0.5 mm, the design is optimized for lower frequencies with pumping power in the range of 0.2-0.8 W for the heater and cooler combined, and a temperature drop of 2-3 °C for each at nominal input thermal power of about 300 W. The regenerator is a stack of woven wire screens with circular cross-section wire. With hydraulic diameter

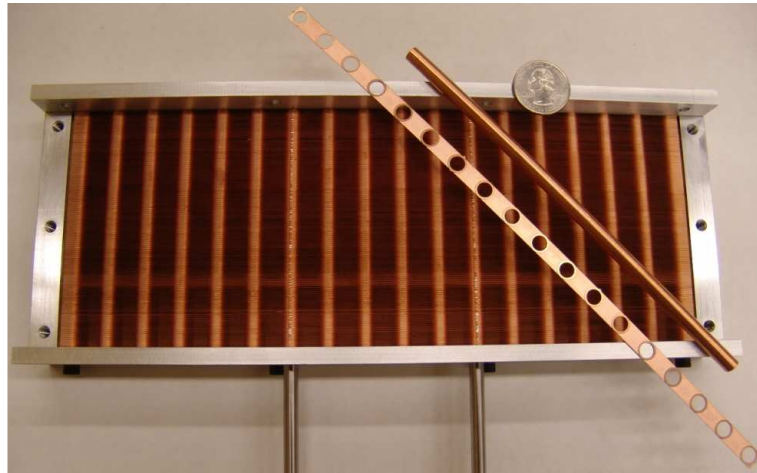


Figure 4.7: Fabricated heat exchanger shown with the etched fins and copper tube inserts.

of about 0.2 mm, the design requires a pumping power of about 0.8-1 W for the regenerator. The tubing and fittings are analyzed analogously to the heater and cooler. The corresponding fluid flow dissipation is evaluated using the mean cross-sectional velocity of the fluid and correlations outlined in chapter 3.2.1. Consequently, these losses contribute an additional 0.5-2 W to the total flow friction dissipation. Total displacer power loss is estimated to be in the range of 2.05-5.4 Watts.

4.3.3 Power Piston

Since this engine is designed to have the potential of being expanded into a multiphase system, the power piston dimensions (diameter, length, and stroke) are made identical to those of the displacer dimensions. By enforcing such an arrangement, one can easily remove the tubing and convert this system into an alpha-type Stirling engine that is the most convenient arrangement for a multiphase Stirling engine system, as discussed in chapter 5.2.

In this design, the power piston is located on the cold side of the engine. This eliminates any heat leakage in the form of thermal conduction through the piston body and facilitates

tighter clearance sealing that is crucial in this case as the pressure difference across the power piston may achieve 0.2 Bars, as seen in Figure 4.3. Like the displacer, the power piston slides along a shaft that passes through a linear motion ball bearing with non-magnetic balls that is embedded in the piston.

The power piston is the moving component of a magnetic circuit, similar to the displacer, which converts the output power of the thermodynamic cycle into electricity. The power piston is fabricated out of low-carbon steel with strong Nd-Fe-B permanent magnets installed on one end, Figure 4.8. With a mass of 6.4 kg, the power piston resonates with the gas spring at the designated operating frequency. Although there is no need for additional springs, a small spring helps set the piston resting position in the middle of the shaft. By using a steel shaft that goal is achieved in this design. The steel shaft, in this case, becomes part of the power piston magnetic circuit and interacts with the power piston itself to minimize the reluctance along the magnetic field. This behavior introduces a small spring effect that tends to keep the power piston at the mid-point along the shaft. Since the power piston delivers power to the load, it forms a heavily damped (low quality factor) component. Therefore, a slight deviation of the power piston gas spring resonant frequency does not hinder the operation of the engine.

The linear motion ball bearing surface friction and eddy loss in the power piston body are the dissipation sources associated with this component. We rely on the friction factor that is experimentally obtained for the displacer ball bearing in the following section. The power piston weighs about 6.4 kg and, hence, the corresponding friction loss at full excursion is estimated to be about 1.25 W. Eddy losses are due to the variable magnetic field that is generated by the load current flowing through the coils. There is no precise



Figure 4.8: Fabricated power piston shown with the low carbon steel body and Nd-Fe-B permanent magnets attached to one end.

estimation for eddy losses at this stage but they are proven to be very small due to the relatively small load currents. If eddy currents were significant, piston would have to be manufactured from a material with low electric conductivity or from electrically insulated laminations.

Due to the pressure differential across power piston, the working fluid will leak in and out through the clearance seal. Calculations predict no more than 1 W dissipation through the wall clearance.

4.3.4 Electromagnetic Circuits

The electromagnetic performance of the displacer piston actuator and the power piston generator is characterized by the finite-element method (FEM) and numerical analysis. COMSOL is the FEM engine which is used to determine magnetic flux density data. A two dimensional axial-symmetric model is considered for both pistons, which assumes ring mag-

nets for the magnetic poles. However, as explained before, the magnetic poles are realized by block magnets in the prototype to eliminate corresponding eddy losses. Therefore, the magnet poles of the fabricated prototype will have lower surface area than the simulated model. Hence, to compensate for this effect, appropriate reduction factors are applied to the remanent flux density data in COMSOL. Since the motion of the displacer piston relative to stationary ferromagnetic components produces different spatial fields at different points along its trajectory, finite-element simulations are repeated for several different positions spanning the full excursion of the piston to obtain a complete picture. The magnetic flux density data is then interpolated over independent spatial dimensions to generate a finer data set appropriate for further calculations.

Numerical computation utilizes the flux density data from the FEM analysis to produce the electro-motive force (EMF) data. The EMF generated by each piston is calculated based on the change in flux linkage, λ , i.e.,

$$\text{EMF} = -\frac{\partial \lambda}{\partial t} = -\frac{\partial \lambda}{\partial z_P} \frac{\partial z_P}{\partial t} \quad (4.1)$$

where the flux linkage is a function of the piston position, z_P . In order to produce a full waveform, the EMF is calculated by this method over one period of the nominal piston trajectory, which is considered to be a single-frequency sinusoid as below,

$$z_P = z_m \sin(\omega t) \quad (4.2)$$

where z_m and ω are, respectively, the amplitude and angular velocity of the piston oscillation. The i -th wire loop of the winding is identified by its radial, r_i , and axial, z_i , distances

from the origin, designated as the neutral resting position of the piston. Therefore, the flux linkage of each wire loop is calculated by numerical integration over the relevant enclosure area, then summed over all wires in the winding configuration. For the concentric winding configuration in the prototype, only axially oriented flux density, B_z , is relevant. Therefore, assuming that each winding has N turns, the flux linkage, $\lambda(z_P)$, is calculated as,

$$\lambda(z_P) = \sum_{i=1}^N \int_0^{r_i} B_z(z_P, z_i, r) 2\pi r dr \quad (4.3)$$

where $B_z(z_P, z_i, r)$ is the axial flux density at position (r, z_i) while the piston is positioned at z_P .

Since EMF data obtained thus far is discrete, frequency domain analysis (the Fourier Series, in this case) is the most effective method to determine the output power of the generator or the required input power of the actuator. At each harmonic frequency, the corresponding equivalent electric circuit is solved based on the loading and EMF component at that particular frequency. For the displacer piston, the fundamental frequency component of the EMF gives an indication of the power developed into useful kinetic energy, while the power contained in all higher harmonics contributes to losses in the windings. For the power piston, the power in the fundamental frequency component gives an indication of the useful power developed at the Stirling engine operating frequency. Note that if the output is rectified, the total RMS power is a more appropriate metric.

The results produced by numerical analysis are verified by a ring-down test. In the ring-down test, the EMF sinusoidal signal has a decaying envelope (refer to appendix A). Therefore, only the measured EMF during the first half-period is expected to closely approx-

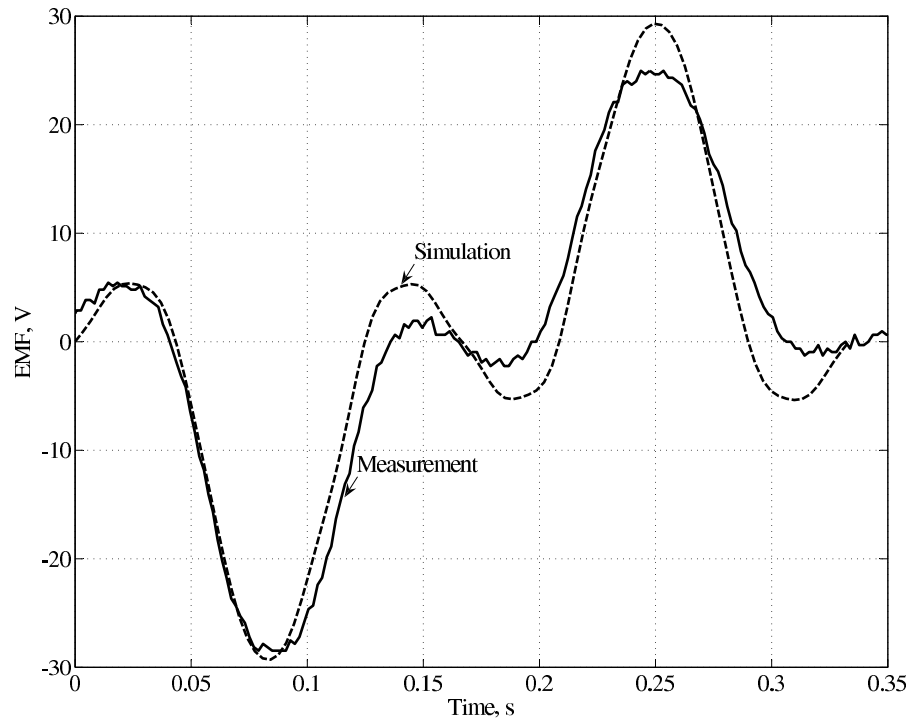


Figure 4.9: Simulated and measured waveforms of the displacer actuator EMF with no separation between the two windings. Refer to Figure 4.4

imate the numerically simulated waveform. The calculated and measured EMF waveforms for this displacer are depicted in Figure 4.9, for the case where there is no spacing between the two windings. For the fabricated prototype, the position of the windings is optimized to achieve the best electromagnetic performance for the displacer and power pistons magnetic circuits. The optimum spacing of the two windings is 2 inches and corresponding simulated and measured EMF waveforms are illustrated in Figure 4.10. Although the fundamental frequency component of EMF is smaller in the optimal case, its harmonic distortion is the smallest in this case which, in turn, generates the lowest copper loss and the highest actuator efficiency.

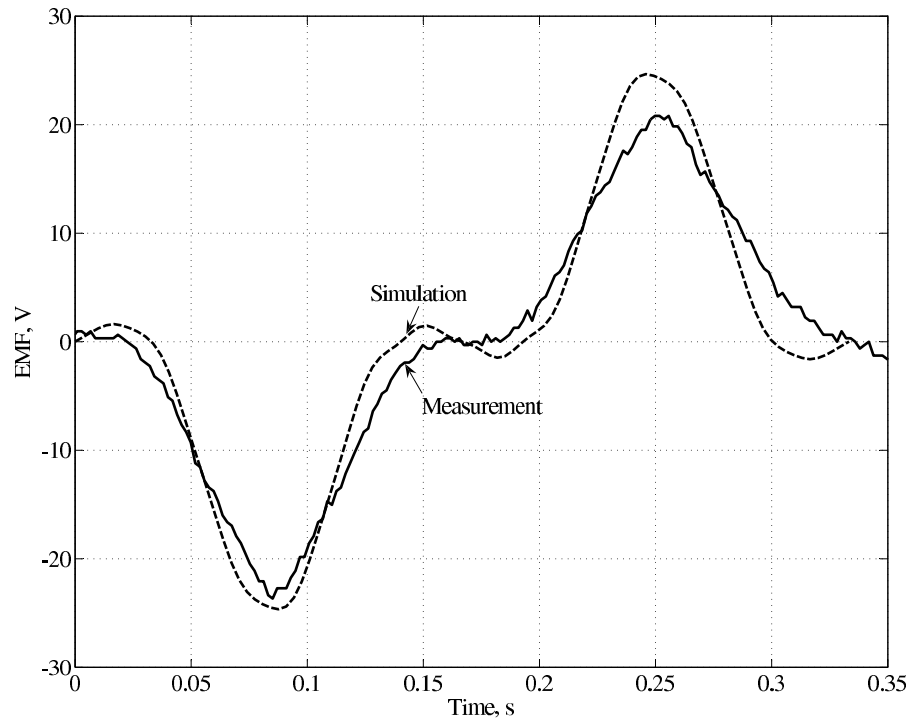


Figure 4.10: Simulated and measured waveforms of the displacer actuator EMF with the optimal separation (2 in.) between the two windings.

4.4 Experimental Assessment

4.4.1 Displacer Piston

The only anticipated sources of dissipation in the displacer piston are the friction between the linear motion ball bearing and the shaft, and minor eddy losses in the permanent magnets and the iron powder rings. A ring-down test, among others, is an appropriate way for estimating the power dissipation of this system. The system is displaced from its equilibrium and is released. By observing the rate and type of the oscillation envelope (exponential for viscous friction or linear for dry friction,) one can translate it into important system parameters such as natural frequency, quality factor, and damping factor which are used to estimate the power loss.

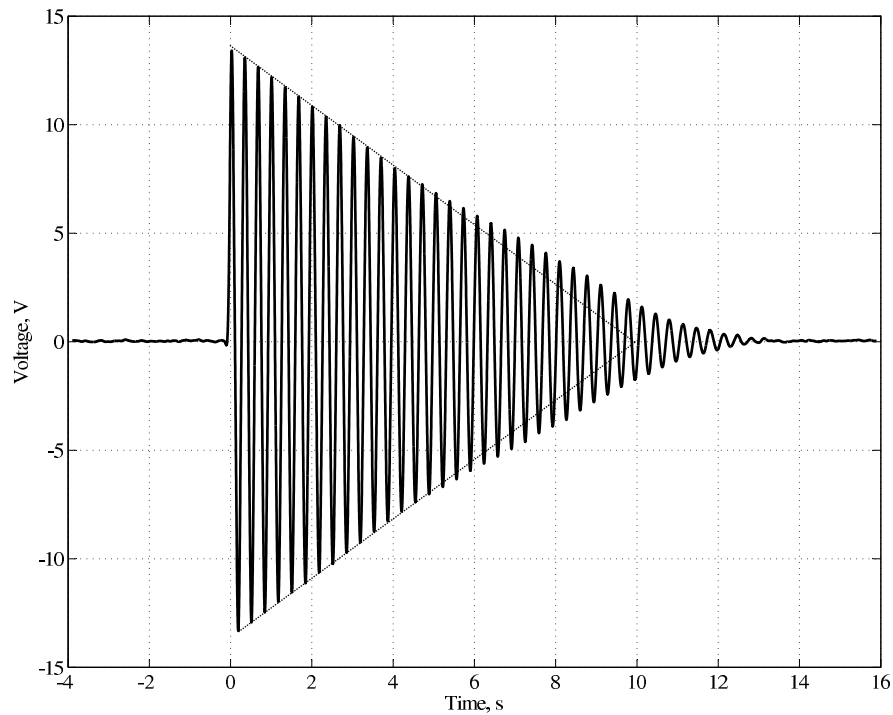


Figure 4.11: Ring-down characteristic of the displacer piston.

Figure 4.11 shows the ring-down characteristic of the displacer piston by displaying open circuit actuator winding voltage. The very first peak corresponds to the maximum velocity of the piston (about 1.4 m/s). This test successfully confirms the expected 3 Hz resonant frequency and low power dissipation of the system. The behavior of this system is to be analyzed at the largest amplitudes as these are representative of the actual operating conditions. The ring-down envelope for larger amplitudes is clearly a straight line that signifies dry friction as the main source of loss. Note that the eddy loss is quadratically proportional to the corresponding eddy current. Eddy current flow is linearly proportional to the rate of change of the magnetic flux density, i.e., it is proportional to the magnitude and to the frequency of the piston oscillation. This implies that the eddy loss could be modeled as a linear damping and would be characterized with an exponential envelope in

a ring-down test. The estimated attenuation rate of the ring-down characteristic is about 0.14 (m/s)/s which corresponds to a friction force of 0.6 N and about 0.5 W of power dissipation. This translates into a surface friction coefficient of 0.02 considering that the displacer piston weighs about 2.9 kg. The average friction coefficient for linear motion ball bearings is expected to be 0.002-0.004 [52], about 5 to 10 times less than the measured friction coefficient. The reason of this discrepancy is unresolved but it could be attributed to the disassembly of the linear motion ball bearing for the replacement of its magnetic ball bearings. To reduce friction, the engine could be aligned with piston axis vertical. In this case, however, the displacer weight would force the resting position of the piston away from the center of the shaft, reducing the stroke.

In order to verify the estimated power dissipation of the displacer piston, the energy-balance approach is implemented. Utilizing only two phases of a three-phase inverter (DC to AC power converter,) alternating voltage is applied to the displacer actuating coils (see Figure 4.4). Both amplitude and frequency of the alternating voltage can be adjusted by varying the inverter DC voltage or switching frequency. The frequency is adjusted to exactly match the resonant frequency obtained from the ring-down test and the DC voltage is increased until the nominal stroke is reached. The equivalent electric circuit of this experiment is depicted in Figure 4.12 with corresponding phasor diagram.

By observing the terminal voltage and input current waveforms, one can calculate the displacer piston mechanical power, P_{mech} , which is the aggregate of surface friction, eddy loss, and fluid flow friction if present, by subtracting the coil copper loss, P_{Cu} , from input

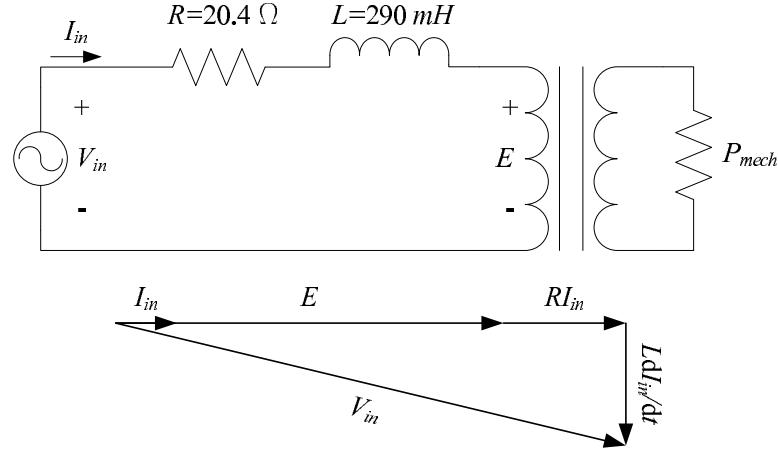


Figure 4.12: Equivalent electric circuit schematic and phasor diagram for the displacer energy balance experiment.

power, P_{in} . Each power component is calculated according to the following expressions:

$$P_{in} = \frac{1}{T} \int_0^T V_{in} I_{in} dt \quad (4.4)$$

$$P_{Cu} = \frac{1}{T} \int_0^T R I_{in}^2 dt \quad (4.5)$$

$$P_{mech} = P_{in} - P_{Cu} \quad (4.6)$$

where T is the period of the actuating signals. Measured resistance and inductance of each coil is about 10.2Ω and 145 mH , respectively.

Figure 4.13 depicts the input voltage and current waveforms together with their harmonic contents when the displacer is tested in absence of the heat exchangers and connecting tubes. The six-step voltage generates current and, hence, copper loss at $6k \pm 1$ harmonic orders. However, the magnetic circuit of the displacer piston subsystem generates a back EMF that is rich in third harmonic. Since the input terminal appears as a short circuit at this frequency due to the small third harmonic component present at the input voltage, a large third harmonic current flows through the electric circuit and increases the

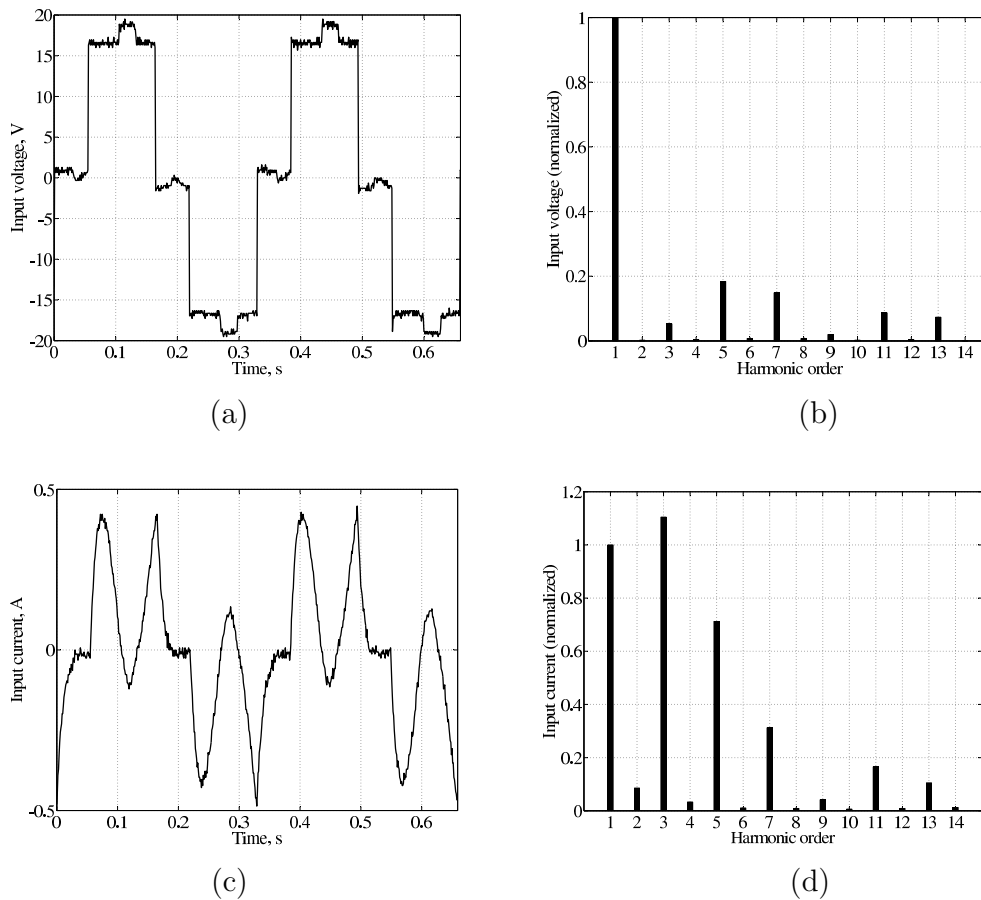


Figure 4.13: (a) Input voltage waveform (b) Input current waveform (c) Input voltage harmonic components (d) Input current harmonic components.

copper loss significantly. In this case, the calculated input power and copper loss are 1.75 W (fundamental frequency power factor is 0.99) and 0.99 W, respectively. Consequently, it is inferred that 0.76 W supplies the losses in the displacer piston. This corresponds to a mediocre actuation efficiency of 43.4%. The actuator performance can be improved by a magnetic circuit design that generates a back EMF with higher fundamental frequency component and no or minimal harmonic distortion or by applying a pure sinusoidal input voltage to the actuator terminals.

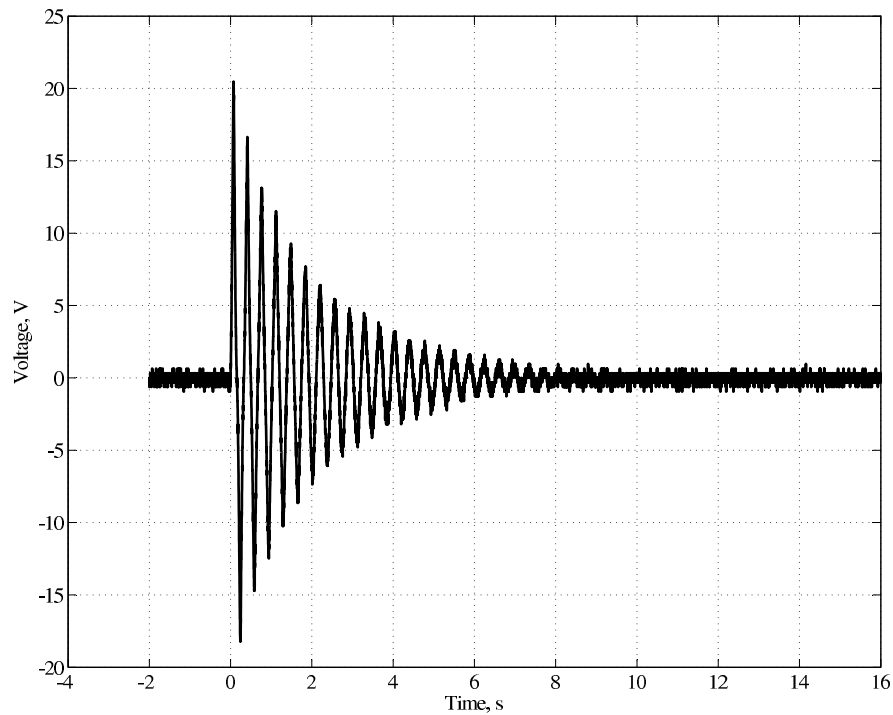


Figure 4.14: Ring-down characteristic of the displacer piston in the presence of the heater, cooler, regenerator, and the connecting pipes and fittings. Compare with Figure 4.11.

4.4.2 Heat Exchangers

Fluid Flow

Both ring-down and energy-balance tests are appropriate methods to assess the fluid flow friction losses through the heat exchangers and the tubing. Figure 4.14 shows the ring-down characteristic of the displacer piston in the presence of all the heat exchangers and tubing. The exponential envelope of the ring-down is a clear indication of the dominant viscous losses. This test yields an estimated power dissipation of 3.2 W at the nominal operating conditions. The energy-balance method indicates about 3.1 W of dissipated power for the same conditions.

Table 4.2 summarizes the estimated losses of the displacer, heat exchangers, and tub-

Table 4.2: Comparison of the calculated component dissipations with the measurement-based estimations.

Component	Calculated, W	Ring-down, W	Energy-balance, W
Piston only	0.05 – 0.1	0.5	0.76
Heat exchangers	1.5 – 3.3	1.1	0.49
Pipes and fittings	0.5 – 2	1.6	1.85
Total	2.05 – 5.4	3.2	3.1

ing and compares them with the design calculations. There is a strong agreement between calculations and estimated values for the fluid flow friction losses which validates the adopted methodologies and computations. The computations for the heat exchangers are conservative, as expected. This may very well compensate for the unknown losses in other components, such as those due to bearing friction.

Heat Transfer

To verify the heat transfer characteristics of the fabricated heat exchangers, 0 °C water (coolant) was circulated at a flow rate of about 1.8 m/s through the cooler copper tubes as shown in Figure 4.17. Since, according to Table 4.3, the fabricated prototype engine successfully produced the indicated output power of about 27 W, it is feasible that the rejected heat by the cooler should be about the corresponding indicated value of 225 W. At this power level, the coolant temperature is expected to rise by 3 °C from the cooler inlet to its outlet. The coolant temperature rise from the source of ice-water to the heat exchanger inlet is about 0.5 °C. Therefore, the coolant average temperature is considered to be 2.0 °C. In addition, due to the limited wetted area provided by the copper tubes, a temperature difference of 15.5 °C is required to reject 225 W from the cooler tubes to the liquid coolant, which means that temperature of the cooler copper tubes is estimated to be 17.5 °C.

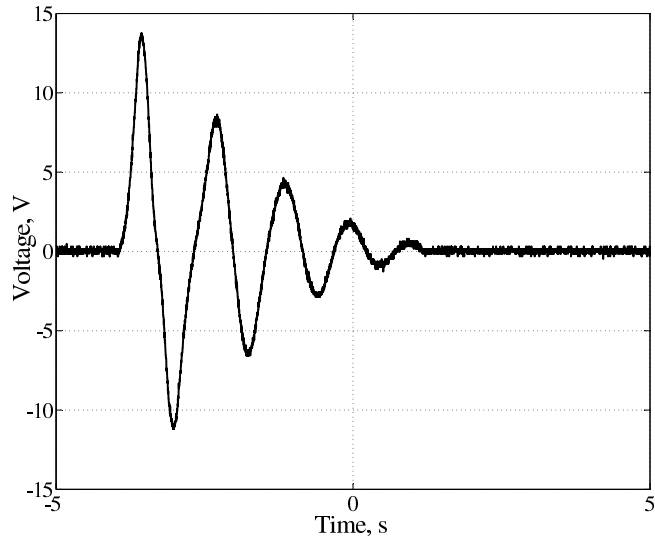


Figure 4.15: Ring-down characteristic of power piston while separated from the rest of the engine.

A thermocouple is placed inside the fabricated engine, very close to the cooler. This thermocouple measures the temperature of the working fluid (air) as it enters or exits the cooler. The thermocouple module reads $22\text{ }^{\circ}\text{C}$, which indicates a $4.5\text{ }^{\circ}\text{C}$ temperature rise from the copper tubes to the working fluid. This figure is very close to the expected $2\text{ }^{\circ}\text{C}$ and it confirms the utilized methodology to estimate heat transfer characteristic of the cooler. Uncertainties in rejected heat and thermal resistance between the copper tubes and the liquid coolant can easily explain this discrepancy.

4.4.3 Power Piston

A ring-down test for the power piston while connected to the engine chamber confirms that the power piston resonates with the gas spring at a frequency of about 2.94 Hz . A ring-down test in which the power piston is separated from the rest of the engine, and hence, is only linked to a weak magnetic spring of its steel shaft enables estimation of the

frictional losses. The recorded ring-down characteristic is shown in Figure 4.15. For this test, the ring-down oscillation frequency is low (about 0.8 Hz), and more uncertainties may prevail in the estimation. The frictional loss for the power piston is estimated to be 2.8 W in this test.

As discussed in section 3.3, gas hysteresis loss can be a significant source of dissipation for free-piston Stirling engines. In order to characterize the gas hysteresis loss for the fabricated prototype, a compression test is performed by actuating the power piston at its operating frequency. The actuation voltage is varied to achieve various piston strokes and, hence, compression ratios or fractional volumetric variations. At each operating point, using the energy-balance approach, one can estimate the power that is dissipated as gas hysteresis loss. Furthermore, the gas hysteresis loss can be estimated by calculating the area enclosed by the measured p - V loop at each operating point as well. The latter approach, adopted in this dissertation, includes the power piston seal leakage in the estimated value, which is expected not to exceed 1 W due to the tight clearance. Figure 4.16 depicts the experimental results of the compression test for the fabricated Stirling engine prototype. As expected from the theoretical model of the gas hysteresis phenomenon, a quadratic function fits nicely to the measured data. As long as the distance of the heat exchanger passages to the outside world is much larger than the thermal skin depth at the operating frequency, the heat exchanger wetted area does not contribute to the gas spring hysteresis dissipation. Therefore, the main contributions to the gas spring hysteresis dissipation comes from the open spaces such as the piston faces, cylinder areas and so on. For the fabricated prototype, the total engine chamber surface area is 0.45 m². However, the measured gas hysteresis dissipation data suggests a wetted area of about 0.78 m². The measured characteristic is

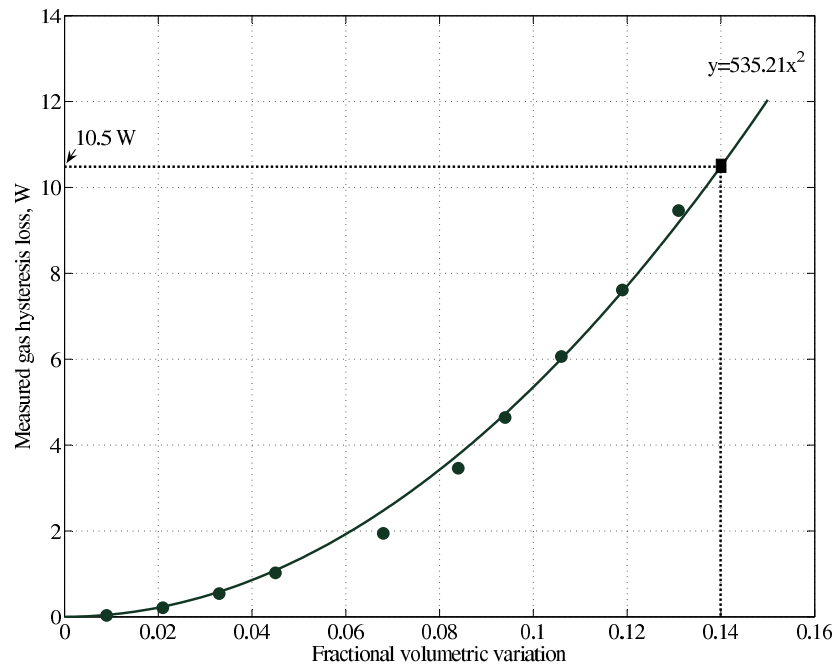


Figure 4.16: Gas hysteresis loss characteristic of the fabricated Stirling engine prototype.

used in the following section to estimate the gas hysteresis loss at the engine operating point.

4.5 Engine Operation

Figure 4.17 depicts the assembled Stirling engine test rig. The heater is heated by a voltage-controlled electric heater. The heating element passes through all the heater tubes. By varying the supply voltage of the heating element, one can adjust the input heat and hot side temperature. The engine is designed to operate at ambient temperature (27 °C) on the cold side. If ambient air were to circulate through the cooler tubes as the coolant, due to the limited wetted area provided by the tubes, its flow rate would be extremely high to provide a small temperature difference between the coolant and the copper tubes.

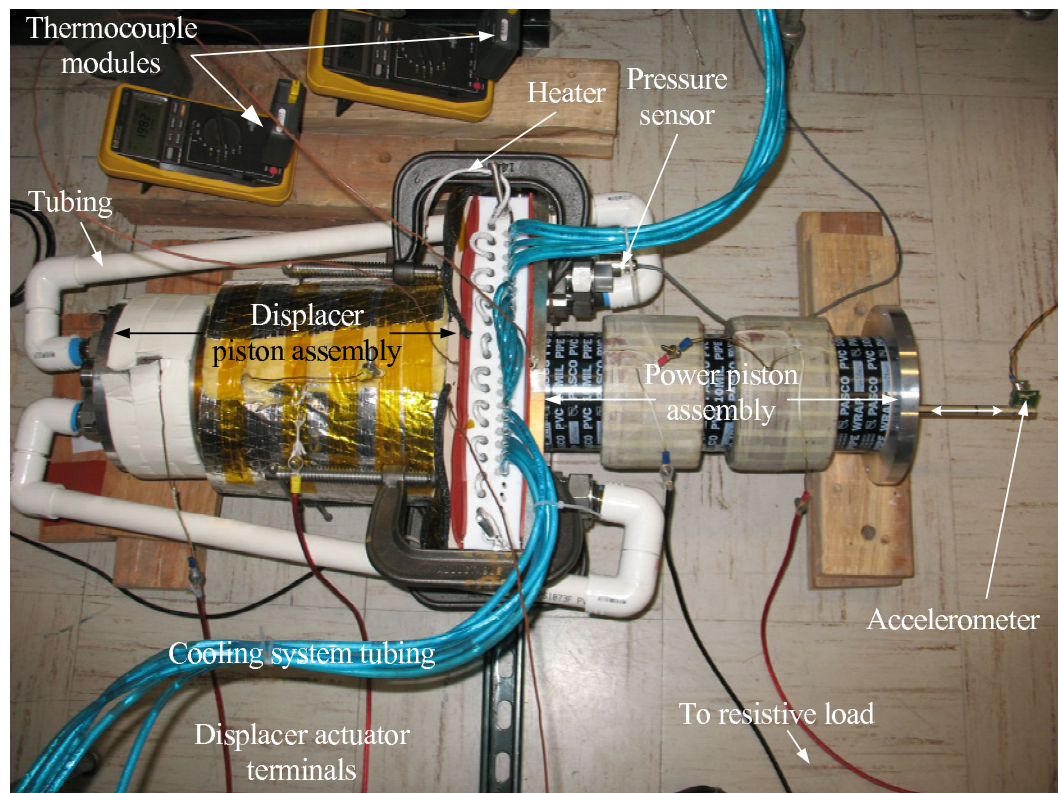


Figure 4.17: The Stirling engine experimental setup.

Therefore, water is chosen as the coolant. For its larger specific heat and density, even at low flow rates, water can absorb significant amount of heat from the cooler at much smaller temperature differences. As mentioned above, the temperature difference between the cooling water and the copper tubes is about $15.5\text{ }^{\circ}\text{C}$ for rejecting 225 W of heat in this case. Therefore, ice-water appears to be a good choice to flow through the copper tubes to keep the compression space temperature close to that of ambient. Furthermore, such a cooling mechanism provides a possible mechanism for transferring thermal power from a solar-thermal collector to the heater of the Stirling engine.

As mentioned before, the displacer is driven by an inverter with adjustable frequency and amplitude. In order to minimize the required driving power, the displacer is driven at its resonant frequency. The voltage amplitude, on the other hand, is adjusted to drive the

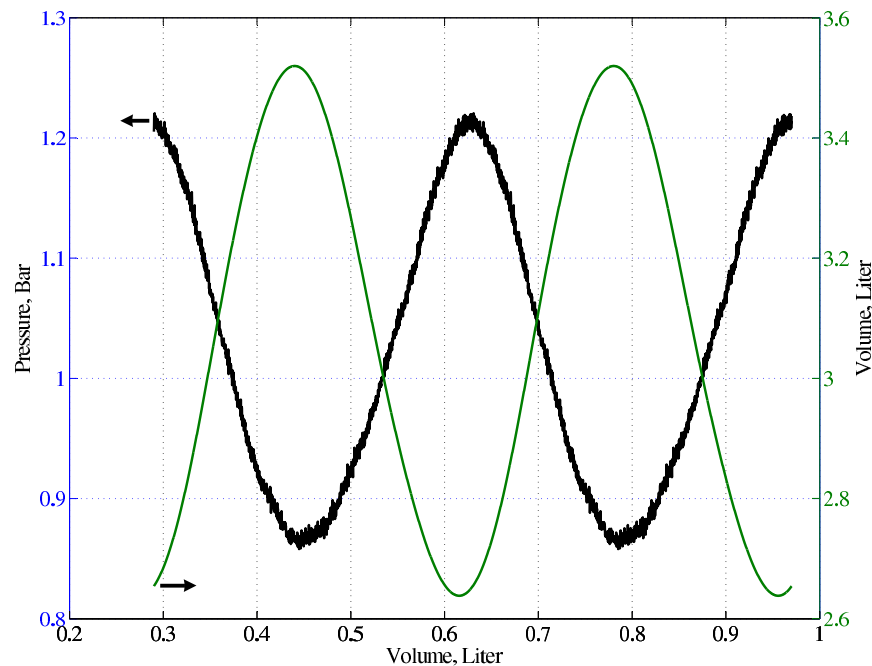


Figure 4.18: Measured engine pressure and volume variations. Compare to Figure 4.3.

displacer at its full stroke.

The chamber pressure and power piston acceleration are monitored by appropriate sensing devices. By processing the acceleration data, one can obtain the power piston velocity and displacement signals. Displacement data will yield volume variation as all the dimensions are exactly known from the design. Combining the pressure and volume signals, the p - V diagram of the thermodynamic cycle is obtained, which then characterizes the produced work.

The electric output of the power piston generator is connected to a resistive load. The voltage and current of the load are monitored as well. Therefore, the energy balance approach may be implemented here to assess the generated power.

Figures 4.18 and 4.19 show the measured pressure and volume variations as well as the p - V characteristic of the engine while the thermocouples measure the working fluid

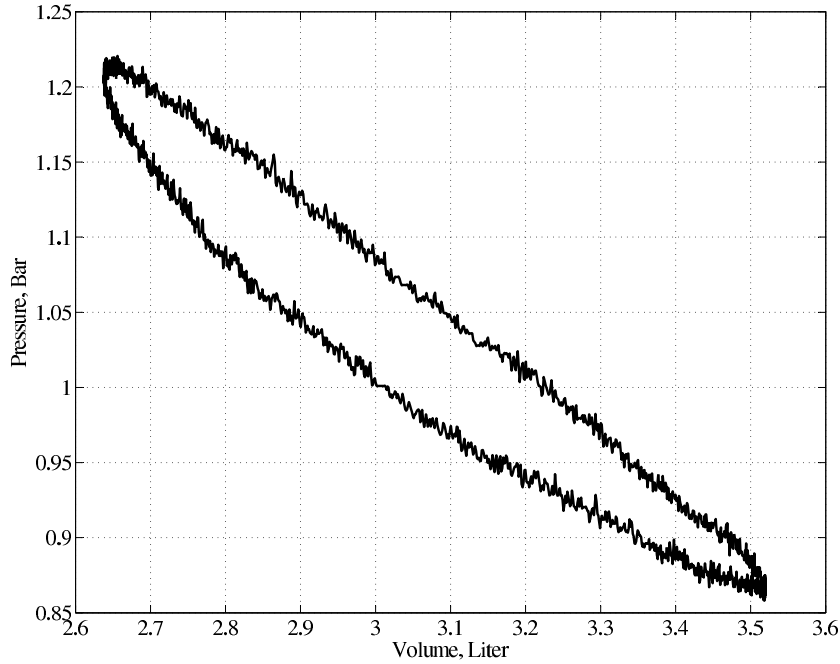


Figure 4.19: Measured p - V diagram of the engine.

temperatures of 184 °C and 22 °C in the vicinity of the heater and cooler, respectively, inside the engine chamber. The displacer piston operates at its full stroke while the power piston stroke is about 11.7 cm. The thermodynamic cycle output work based on the measured p - V characteristic is 15.9 W. Electrical measurements further confirm that about 9.3 W is delivered to the resistive load and 5.2 W is dissipated in the power piston coils. Therefore, one can conclude that about 1.4 W is dissipated as the power piston frictional and eddy losses. Comparison of the measured data with simulation results, Figure 4.3, indicates a good match for the pressure and volume amplitude variations.

As the power piston oscillates, the engine volume varies as a function of the power piston position. Fractional volumetric variation (FVV) is defined as,

$$\text{FVV} = \frac{V_{max}}{V_o} - 1 \quad (4.7)$$

where V_{max} indicates the maximum volume of the chamber and corresponds to the outmost position of the power piston and V_o is the mean value of the volume variation which corresponds to the resting position of the power piston. The FVV for the above operating conditions is about 0.14. The gas hysteresis characteristic of the engine, Figure 4.16, suggests that 10.5 W of the output pV work is spent for the gas hysteresis loss. In addition, a small portion of the indicated output power is dissipated as enthalpy loss through the power piston clearance seal as well which, as mentioned before, is included in the gas hysteresis characteristic.

Note that the thermocouples in the experimental setup are located very close to the heat exchangers and they measure the working fluid temperature as it exits (or enters) the heat exchangers. Due to the heat leakage in the system, especially through the thin cylinder walls, the measured temperatures are probably higher than the actual average fluid temperatures that govern the thermodynamic cycle. This results in a higher output power prediction based on both isothermal and adiabatic models [33]. Therefore, it is concluded that the remaining 0.5 W of the dissipated power must be in the form of enthalpy loss through the expansion space walls.

A summary of the above discussion is tabulated in Table 4.3. The isothermal Stirling engine model predicts 26.9 W mechanical output work. However, the recorded p - V loop (Figure 4.19) indicates an output work of 15.9 W. The compression test, on the other hand, revealed that 10.5 W is dissipated as gas spring hysteresis. Therefore, the power balance principle suggests only 0.5 W difference which is well within the measurement uncertainty, or it can be attributed to the enthalpy loss through the expansion space walls. On the electric side, 9.3 W is delivered to the load as electric power and 5.2 W is dissipated as copper

Table 4.3: Power balance for the fabricated prototype at the operating point discussed in this paper. † indicates a directly measured parameter. All other parameters are calculated based on energy balance principle and the measured values.

Indicated power (isothermal analysis)	26.9 W
Gas hysteresis loss [†]	10.5 W
Expansion space enthalpy loss	0.5 W
Cycle output work [†]	15.9 W
Bearing friction and eddy loss	1.4 W
Coil resistive loss [†]	5.2 W
Power delivered to electric load [†]	9.3 W

loss in the windings. Hence, the remaining 1.4 W (including measurement uncertainties) is dissipated as linear ball bearing friction and eddy loss in the power piston body that is solid low-carbon steel.

4.6 Conclusions

Design, fabrication, and measurement results of a single-phase free-piston Stirling engine were presented in this chapter. The low-power prototype was designed and fabricated to act as a test rig to provide a clear understanding of the Stirling cycle operation. It helped to identify the key components and the major dissipation sources and to verify the theoretical models.

A very low-loss resonant displacer piston was designed for the system using a magnetic spring. Incorporating an array of permanent magnets, the magnetic spring had a very linear stiffness characteristic within the range of the displacer stroke. The power piston was not mechanically linked to the displacer piston and formed a mass-spring resonating subsystem with the gas spring and had resonant frequency matched to that of the displacer. The displacer piston, cylinders, and heat exchangers frame was fabricated by plastic materials. The design of heat exchangers were discussed with an emphasis on their low fluid friction

losses. The total power loss of the displacer piston, heat exchangers, and tubing at nominal conditions is minimal and well-within the calculated range at design stage. The fabricated engine prototype was successfully tested and the experimental results were presented and discussed. The fabricated engine was almost noiseless due to the low operating frequency. There was a slight audible noise that was generated by the linear ball bearing. Similarly, the engine vibration was very little as well. Extensive experimentation on individual component subsystems confirmed the theoretical models and design considerations, providing a sound basis for higher power Stirling engine designs for residential or commercial deployments.

Chapter 5

Multi-Phase Stirling Engines

5.1 Introduction

Single-phase Stirling engines require two pistons, namely the displacer piston and the power piston, for successful operation. The displacer piston shuttles the working fluid back and forth between hot and cold sections of the engine, and, hence, generates an oscillatory pressure waveform inside the engine chamber. Coupling to the pressure waveform, the power piston moves and extracts the mechanical work that is produced by the Stirling thermodynamic cycle. Except for free-piston engines [33, 53], displacer and power pistons are mechanically linked to provide an appropriate phase delay, which facilitates power extraction.

Figure 5.1 shows the schematic diagram of a multi-phase Stirling engine. Each engine is an Alpha-type Stirling engine that is connected to its neighboring two engines via its two pistons. A multi-phase Stirling engine system must incorporate at least three engines and, hence, three pistons. There need not be mechanical linkage among pistons, multi-

phase Stirling engines can be implemented as free-piston engines. The working fluid in each engine is contained within its chamber and is not exchanged nor shared with other phases. Each piston is linked to its neighboring two pistons via the pressure waveform inside corresponding engine chambers. A multi-phase Stirling engine system is a good alternative to its single-phase counterparts in certain ways:

- It successfully eliminates the displacer piston and corresponding design and control problems.
- Each piston is double-acting, that is, it acts as the compression piston for one engine and as the expansion piston for the other.
- There is only one piston per phase which means that the system complexity is relatively reduced.
- It is self-starting.

The general formulation of a multi-phase Stirling engine is presented in this chapter followed by the modal analysis of the symmetric three-phase system. The design, fabrication, and experimental evaluation of a symmetric three-phase Stirling engine system is discussed next, which leads to the theoretic formulation, modal analysis, and experimental implementation of a “reverser” mechanism in multi-phase Stirling systems.

5.2 Formulation

An isothermal model [33] is the simplest formulation for thermodynamic behavior of a Stirling engine, and is used in this section to understand the qualitative system behavior.

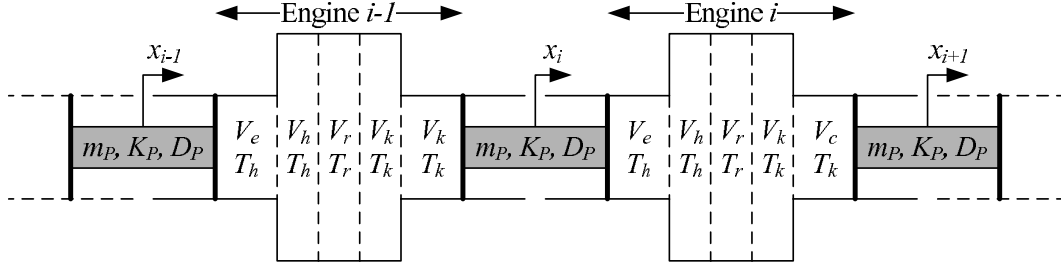


Figure 5.1: Schematic diagram of a multi-phase Stirling engine system.

For the i -th Stirling engine that operates within an N -phase system (Figure 5.1), pressure of the working fluid, p_i , is given by,

$$p_i = (MR) / \left(\frac{V_{e,i}}{T_h} + \frac{V_{c,i}}{T_k} + \frac{V_k}{T_k} + \frac{V_r}{T_r} + \frac{V_h}{T_h} \right) \quad i = 1, \dots, N \quad (5.1)$$

where M is the mass of the working fluid, R is the ideal gas constant, $V_{e,i}$ and $V_{c,i}$ are, respectively, the volumes of expansion and compression spaces, T_h and T_k are, respectively, the temperatures of the heater and cooler in each Stirling engine, and finally V_h , V_r , and V_k are the free volumes of the heater, regenerator, and cooler, respectively. The isothermal model presumes that the temperatures of expansion and compression spaces are T_h and T_k , respectively. The regenerator is sandwiched between heater and cooler and is considered to be adiabatic. Assuming a linear temperature profile across the regenerator, its mean effective temperature, T_r , can then be expressed as [33],

$$T_r = \frac{T_h - T_k}{\ln(T_h/T_k)} \quad (5.2)$$

Table 5.1: Three examples of common dissipation and loading functions. Parameters D , F_f , and L_P are, respectively, viscous friction factor, dry friction force, and loading factor, and $\mathcal{S}(\cdot)$ is the sign function.

Dissipation/Loading	$f_P(\dot{x})$	$\overline{\dot{W}_P}(x_m, \omega)$
Linear viscous dissipation	$D\dot{x}$	$(1/2)D(\omega x_m)^2$
Dry friction	$F_f\mathcal{S}(\dot{x})$	$(2/\pi)F_f(\omega x_m)$
Third-order nonlinear load	$L_P\dot{x}^3$	$(3/8)L_P(\omega x_m)^4$

Furthermore, $V_{e,i}$ and $V_{c,i}$ are calculated as a function of nominal volumes of expansion and compression spaces, V_e^{nom} and V_c^{nom} respectively, as,

$$V_{e,i} = V_e^{nom} - A_P x_i \quad (5.3)$$

$$V_{c,i} = V_c^{nom} + A_P x_{i+1} \quad (5.4)$$

where x_i is the displacement of the i -th piston and A_P is the cross-sectional area of each piston.

Consider each piston to be a mass-spring subsystem (m_P, K_P) , with a dissipation or loading function, $f_P(\dot{x}_i)$. Each piston is coupled to its two adjacent neighbors through the working gas modeled by Eq. (5.1). Table 5.1 tabulates three examples of common dissipation and loading functions. The third column of this table tabulates the average dissipated or consumed power, $\overline{\dot{W}_P}$, in each case using,

$$\overline{\dot{W}_P} = \frac{1}{T} \int_T f_P dx \quad (5.5)$$

where $x = x_m \sin(\omega t)$.

The system of differential equations in Eq. (5.6), representing Newton's second law, defines the nonlinear dynamical behavior of the i -th piston in a multi-phase system. Note

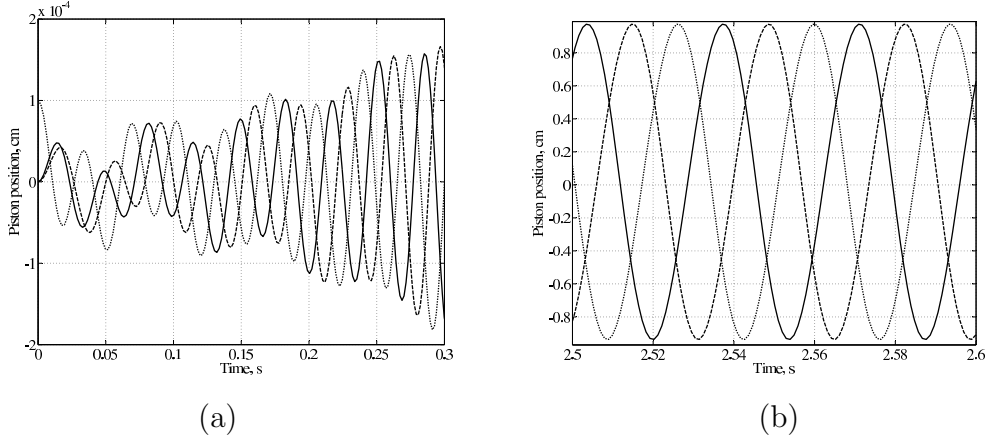


Figure 5.2: Simulated piston positions of the symmetric three-phase system. (a) Startup (b) Steady state.

that the N -th engine is followed by the first engine in a multi-phase system loop.

$$A_P (p_{i-1} - p_i) - f_P (\dot{x}_i) - K_P x_i = m_P \ddot{x}_i \quad (5.6)$$

where $i = 1, \dots, N$ and $f_P (\dot{x})$ may include any possible dissipation or loading model.

In steady-state operation, the pistons have a symmetrically skewed-phase oscillatory motion as shown in Figure 5.2(b). Of course, the output power of each engine, and hence the entire system, is a function of the phase delay between volume variation of compression and expansion spaces [33]. The simulation result of a symmetric three-phase Stirling engine system is depicted in Figure 5.2.

5.3 Linearization

System linearization at the or any of the system equilibria is an effective tool for qualitative analysis of nonlinear system behavior. Origin, x_0 , is the equilibrium of the multi-phase Stirling engine system defined by differential equations in Eq. (5.6). According

to the Hartman-Grobman theorem [54], the qualitative properties of nonlinear systems in the vicinity of isolated equilibria are determined by linearization of the nonlinear system if the linearization has no eigenvalues on the $j\omega$ -axis. Furthermore, the indirect method of Lyapunov proves that if the linearization of a nonlinear system around the origin has at least one eigenvalue in \mathbb{C}_+^o (right half of the complex plane excluding $j\omega$ -axis), then the origin is an unstable equilibrium for the nonlinear system [54].

Appropriate substitutions from Eqs. (5.3) and (5.4) and linearization of Eq. (5.6) leads to Eq. (5.7) which models the linearized dynamical behavior of the i -th piston.

$$\ddot{x}_i = \left(\frac{\alpha}{m_P} \frac{1}{T_h} \right) x_{i-1} - \left(\frac{\alpha}{m_P} \frac{1}{T_h} + \frac{\alpha}{m_P} \frac{1}{T_k} + \frac{K_P}{m_P} \right) x_i + \left(\frac{\alpha}{m_P} \frac{1}{T_k} \right) x_{i+1} - d\dot{x}_i \quad (5.7)$$

where $i = 1, \dots, N$ and,

$$\alpha = (MR) / \left(\frac{V_c^{nom}}{T_k} + \frac{V_k}{T_k} + \frac{V_r}{T_r} + \frac{V_h}{T_h} + \frac{V_e^{nom}}{T_h} \right)^2 A_P^2 = \frac{p^2 A_P^2}{MR} \quad (5.8)$$

$$d = \frac{1}{m_P} \left. \frac{\partial f_P(\dot{x}_i)}{\partial \dot{x}_i} \right|_{\dot{x}_i=0} \quad (5.9)$$

with p representing the mean pressure of the working fluid.

Therefore, the linearization of multi-phase Stirling engine system with fixed heater and cooler temperatures would be represented as a time-invariant autonomous linear system as

in Eq. (5.10).

$$\begin{bmatrix} \ddot{x}_1 \\ \ddot{x}_2 \\ \ddot{x}_3 \\ \vdots \\ \ddot{x}_{N-2} \\ \ddot{x}_{N-1} \\ \ddot{x}_N \end{bmatrix} + d \begin{bmatrix} \dot{x}_1 \\ \dot{x}_2 \\ \dot{x}_3 \\ \vdots \\ \dot{x}_{N-2} \\ \dot{x}_{N-1} \\ \dot{x}_N \end{bmatrix} + \begin{bmatrix} a & -b & 0 & \cdots & 0 & 0 & -c \\ -c & a & -b & \cdots & 0 & 0 & 0 \\ 0 & -c & a & \cdots & 0 & 0 & 0 \\ \vdots & \vdots & \vdots & \ddots & \vdots & \vdots & \vdots \\ 0 & 0 & 0 & \cdots & a & -b & 0 \\ 0 & 0 & 0 & \cdots & -c & a & -b \\ -b & 0 & 0 & \cdots & 0 & -c & a \end{bmatrix} \begin{bmatrix} x_1 \\ x_2 \\ x_3 \\ \vdots \\ x_{N-2} \\ x_{N-1} \\ x_N \end{bmatrix} = 0 \quad (5.10)$$

where

$$a = \frac{K_P}{m_P} + \frac{\alpha}{m_P} \frac{1}{T_k} + \frac{\alpha}{m_P} \frac{1}{T_h} = \frac{K_P}{m_P} + (b + c) \quad (5.11)$$

$$b = \frac{\alpha}{m_P} \frac{1}{T_k} \quad (5.12)$$

$$c = \frac{\alpha}{m_P} \frac{1}{T_h} \quad (5.13)$$

5.4 Analysis

Based on the above discussion on mathematical modeling, the modal analysis of the linearized multi-phase Stirling engine system will be discussed in this section. Specifically, the symmetrical three-phase system will be considered and analyzed. Discussion on the design, fabrication, and test of a three-phase Stirling engine prototype will follow the theoretical results for comparison purposes.

Eigenvalues of the linearized multi-phase system are functions of engine geometry, piston dynamical parameters, mean engine working pressure, and the heater and cooler

temperatures. However, for a fabricated engine, the temperatures are the only parameters that may vary and affect the eigenvalues. Therefore, assuming that the cooler temperature remains unchanged, effect of the heater temperature, T_h , will be considered and discussed for the above-mentioned Stirling engine examples.

5.4.1 Symmetric Three-Phase System

For the symmetric three-phase system, Eq. (5.10) is rewritten as,

$$\begin{bmatrix} \ddot{x}_1 \\ \ddot{x}_2 \\ \ddot{x}_3 \end{bmatrix} + d \begin{bmatrix} \dot{x}_1 \\ \dot{x}_2 \\ \dot{x}_3 \end{bmatrix} + \begin{bmatrix} \frac{K_P}{m_P} + (b+c) & -b & -c \\ -c & \frac{K_P}{m_P} + (b+c) & -b \\ -b & -c & \frac{K_P}{m_P} + (b+c) \end{bmatrix} \begin{bmatrix} x_1 \\ x_2 \\ x_3 \end{bmatrix} = 0 \quad (5.14)$$

or simply,

$$\ddot{\mathbf{x}} + d\dot{\mathbf{x}} + \mathbf{K}\mathbf{x} = 0 \quad (5.15)$$

where d is defined in Eq. (5.9).

By applying the Clark's transformation [55] $\mathbf{x} = \mathbf{T}\mathbf{z}$, where,

$$\mathbf{T} = \begin{bmatrix} \cos(0) & \sin(0) & \cos(0) \\ \cos(0) & \sin(\frac{2\pi}{3}) & \cos(\frac{2\pi}{3}) \\ \cos(0) & \sin(\frac{4\pi}{3}) & \cos(\frac{4\pi}{3}) \end{bmatrix} = \begin{bmatrix} 1 & 0 & 1 \\ 1 & \sqrt{3}/2 & -1/2 \\ 1 & -\sqrt{3}/2 & -1/2 \end{bmatrix} \quad (5.16)$$

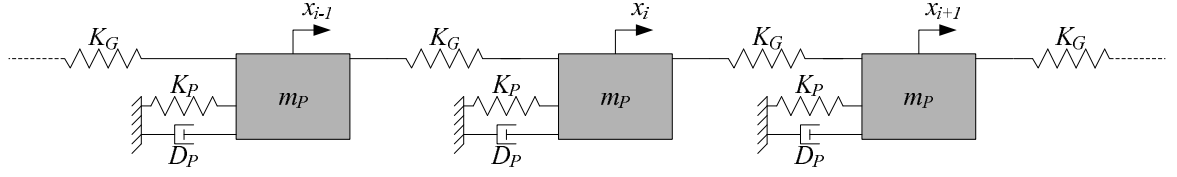


Figure 5.3: Mass-spring equivalent of the multi-phase Stirling engine system in Figure 5.1. K_G represents the gas spring stiffness.

Eq. (5.14) becomes,

$$\begin{bmatrix} \ddot{z}_1 \\ \ddot{z}_2 \\ \ddot{z}_3 \end{bmatrix} + d \begin{bmatrix} \dot{z}_1 \\ \dot{z}_2 \\ \dot{z}_3 \end{bmatrix} + \begin{bmatrix} \frac{K_P}{m_P} & 0 & 0 \\ 0 & \frac{K_P}{m_P} + \frac{3}{2}(b+c) & -\frac{\sqrt{3}}{2}(b-c) \\ 0 & \frac{\sqrt{3}}{2}(b-c) & \frac{K_P}{m_P} + \frac{3}{2}(b+c) \end{bmatrix} \begin{bmatrix} z_1 \\ z_2 \\ z_3 \end{bmatrix} = 0 \quad (5.17)$$

or,

$$\ddot{\mathbf{z}} + d\dot{\mathbf{z}} + \tilde{\mathbf{K}}\mathbf{z} = 0 \quad (5.18)$$

where $\tilde{\mathbf{K}} = \mathbf{T}^{-1}\mathbf{K}\mathbf{T}$ and hence $\tilde{\mathbf{K}}$ shares the same eigen-structure with matrix \mathbf{K} . The linear transformation \mathbf{T} elegantly decouples the system dynamical modes and readily exhibits its eigenvalues.

Figure 5.3 illustrates the mass-spring equivalent of the multi-phase Stirling engine system shown in Figure 5.1. For the sake of simplicity, the analysis is begun assuming $d = 0$. The effect of linear damping will be considered later on, after establishing the basis of the modal analysis. Based on this assumption, Eq. (5.15) becomes the classic state space representation of a resonator, i.e., $\ddot{\mathbf{x}} + \mathbf{K}\mathbf{x} = 0$. The eigenvalues of a resonator are the roots of the eigenvalues of the matrix $-\mathbf{K}$, and hence the roots of the eigenvalues of $-\tilde{\mathbf{K}}$. Therefore, if μ_1 is an eigenvalue of matrix $\tilde{\mathbf{K}}$, then λ_1 and λ'_1 are two eigenvalues of

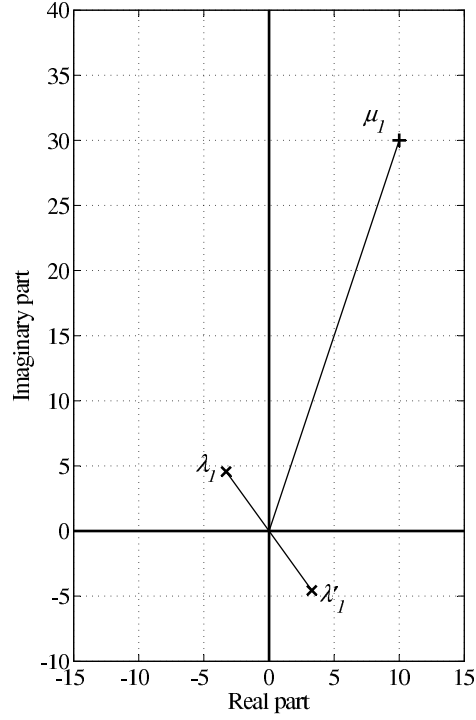


Figure 5.4: Relationship between a complex numbers, μ_1 , λ_1 , and λ'_1 .

the system associated with μ_1 and we have,

$$\lambda_1 = \sqrt{-\mu_1} = \sqrt{|\mu_1|} e^{j(\frac{\pi}{2} + \frac{1}{2}\angle\mu_1)} \quad (5.19)$$

$$\lambda'_1 = \sqrt{-\mu_1} = \sqrt{|\mu_1|} e^{j(\frac{3\pi}{2} + \frac{1}{2}\angle\mu_1)} \quad (5.20)$$

where $|\cdot|$ and \angle denote the amplitude and phase of a complex number, respectively.

Matrix $\tilde{\mathbf{K}}$ has one real and one pair of complex-conjugate eigenvalues. The real eigenvalue generates two eigenvalues for the system in Eq. (5.14) that are fixed on the $j\omega$ -axis and they correspond to a decoupled “zero-sequence” or simple oscillation mode where none of the working gas volumes undergoes any expansion or compression. Rather, each of the gas volumes is simply shuttled back and forth (in phase) through its respective heater,

cooler, and regenerator. Hence, the frequency of this mode is independent of the gas spring stiffness and is set only by the stiffness of the piston linkage, K_P . Although this mode is of no interest from a thermodynamic point of view, it is useful in allowing an independent assessment of fluid flow losses. The complex-conjugate eigenvalues of matrix $\tilde{\mathbf{K}}$ are,

$$\mu_1 = \left(\frac{K_P}{m_P} + \frac{3}{2}(b+c) \right) + j \frac{\sqrt{3}}{2}(b-c) \quad (5.21)$$

$$\mu_2 = \left(\frac{K_P}{m_P} + \frac{3}{2}(b+c) \right) - j \frac{\sqrt{3}}{2}(b-c) \quad (5.22)$$

At thermal equilibrium (i.e., $T_h = T_k$), b and c are equal. Hence,

$$\mu_1 = \mu_2 = \frac{K_P}{m_P} + 3b = \frac{K_P + 3K_G}{m_P} \quad (5.23)$$

$$\lambda_1 = \lambda_2 = -\lambda'_1 = -\lambda'_2 = j \sqrt{\frac{K_P + 3K_G}{m_P}} \quad (5.24)$$

where K_G is the isothermal gas spring stiffness which is illustrated in Figure 5.3 and derived in Appendix B. However, the slightest temperature difference between compression and expansion spaces (i.e., $T_h > T_k$) forces μ_1 and μ_2 away from the real axis. Consequently, the two eigenvalues λ'_1 and λ_2 , which correspond to the “forward” three-phase operating mode [29], migrate to the right half of the complex plane and the equilibrium becomes unstable. Therefore, according to the Hartman-Grobman theorem and indirect Lyapunov method, the main nonlinear system becomes unstable. The unstable mode is expected to grow spontaneously until a loading mechanism (e.g., the generator and electric loading) absorbs mechanical power at the same rate that it is produced. This is the intended mode of operation and makes the system become “self-starting.” Note that the real part of μ , $\Re(\mu)$,

is a linear function of the average value of the compression and expansion temperatures, and the imaginary part of μ , $\Im(\mu)$, is proportional to the difference of those two temperatures.

Also of interest is the complex pair of eigenvalues in the left half plane, λ_1 and λ_2 . This pair corresponds to “backward” three-phase operation where mechanical power needs to be supplied at this resonant frequency to support the motion. This mode corresponds to operation as a Stirling heat pump.

The next step is to consider the effect of the system internal losses (e.g., flow friction through heat exchangers, gas spring hysteresis loss, etc.) that are represented by a linear damping factor, d . Since internal dissipation reduces the useful output work of the Stirling cycle, the system should be designed for minimal losses. Damping factor, d , approximately shifts all six λ eigenvalues (i.e., the roots of the eigenvalues of $-\mathbf{K}$) to the left by $d/2$, as depicted in Figure 5.5. It moves the imaginary parts of the eigenvalues toward center as well. However, since the latter is a small effect, it is ignored in this analysis. In the case of a non-zero damping factor, as one can observe in Figure 5.5, a minimum temperature difference is required to force eigenvalues of the system to the unstable region and generate an unstable equilibrium. It is desired to estimate the minimum “start-up” temperature.

If the compression space temperature, T_k , remains unchanged, as the expansion space temperature, T_h , increases from the thermal equilibrium, the eigenvalues associated with the forward mode migrate toward the $j\omega$ -axis almost in parallel to the real axis. This reasoning is based on the argument that the temperature rise does not change the gas spring stiffness significantly. Therefore, the imaginary part of the eigenvalues, which is calculated in Eq. (5.24), remains constant. The equilibrium becomes unstable when the eigenvalues hit the $j\omega$ -axis. In this case, by utilizing trigonometric principles and identities

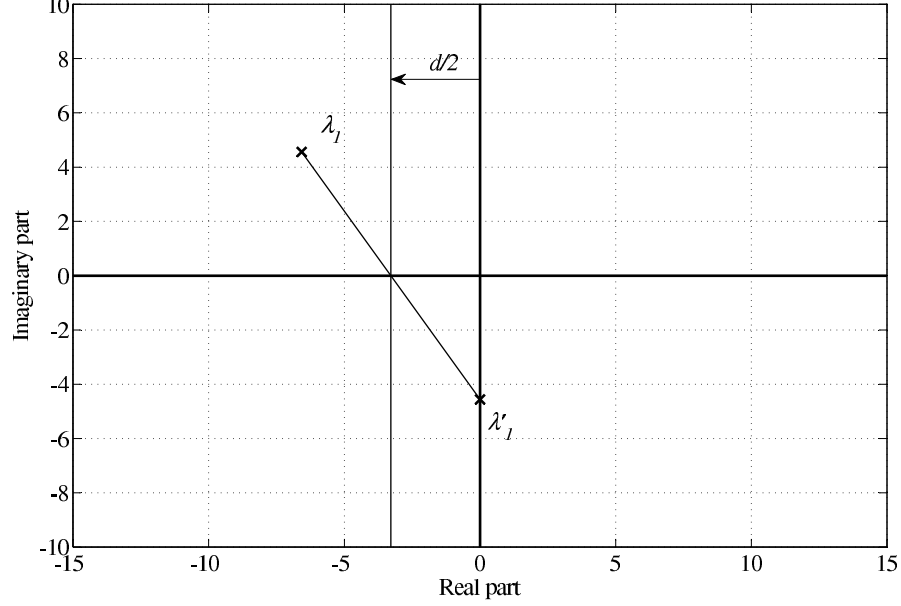


Figure 5.5: Approximated effect of system dissipation on the eigenvalues. Compare to Figure 5.4.

for Figure 5.5, we have,

$$d = 2\Re(\lambda'_1) = 2|\lambda'_1| \cos\left(\frac{3\pi}{2} + \frac{\theta}{2}\right) \quad (5.25)$$

$$\sqrt{\frac{K_P + 3K_G}{m_P}} \approx -\Im(\lambda'_1) = -|\lambda'_1| \sin\left(\frac{3\pi}{2} + \frac{\theta}{2}\right) \quad (5.26)$$

where $\theta = \angle\mu_1$. By multiplying both sides of Eqs. (5.25) and (5.26), we have,

$$d\sqrt{\frac{K_P + 3K_G}{m_P}} = -|\lambda'_1|^2 \sin(3\pi + \theta) = |\mu_1| \sin(\theta) = \Im(\mu_1) = \frac{\sqrt{3}}{2}(b - c) \quad (5.27)$$

and appropriate substitutions from Eqs. (5.12) and (5.13) lead to,

$$\frac{1}{T_h} = \frac{1}{T_k} - \frac{d}{\alpha} \sqrt{\frac{4}{3}m_P(K_P + 3K_G)} \quad (5.28)$$

Equation (5.28) specifies an interesting relationship between parameters d and T_h . Given the design parameters of the engine (i.e. volumes, cold side temperature, mean working gas pressure, piston linkage mass and stiffness, and piston area) one can calculate the maximum damping factor d that will allow the symmetric three-phase Stirling engine system to start at a given T_h . Conversely, for a given damping factor d , the minimum temperature T_h that starts the engine can be calculated.

Similarly, a symmetric six-phase Stirling system can be formulated and analyzed to identify the coresponding dynamical modes, resonant frequency, and start-up temperature. The modal analysis of a symmetric six-phase Stirling system is summarized in appendix C. The following two sections will discuss the fabrication and experimental assessment of a symmetric three-phase Stirling engine to validate the foregoing theoretical discussion.

5.5 Symmetric Three-Phase Stirling Prototype

The design, fabrication and testing of a symmetric three-phase Stirling engine system is presented in this section. The thermodynamic design parameters of the fabricated three-phase Stirling engine system are tabulated in Table 5.2. Ambient pressure air was selected initially as the working fluid of the Stirling engines in order to avoid difficulties pertaining to gas containment during the laboratory tests. In order to eliminate surface-to-surface sliding friction, the pistons are realized by diaphragms, which also seal the engine chambers. Each piston is connected to the piston of its neighboring engine via a rigid linkage, and as will be explained, the oscillation of piston linkages is supported by a nylon cantilever flexure.

Ideally, each engine in the system produces about 12.7 W output mechanical power with 20.2% efficiency at 29.4 Hz. Of course, in practice, this figure will be lower due to the

Table 5.2: Prototype three-phase Stirling engine parameters. Volume multipliers indicate the porosity of each section.

Fluid	Air
p	100 kPa
T_k	27 °C
T_h	147 °C
MR	0.119 J/K (at 1 bar and T_k)
x_m^{nom}	1 cm
A_P	45.6 cm ²
m_P	0.64 kg
K_P	3.58 kN/m
V_e^{nom}, V_c^{nom}	93.2 cm ³ × 100%
V_h, V_k	82.4 cm ³ × 64%
V_r	108.9 cm ³ × 53%
V_{total}	349.6 cm ³
K_G	5.95 kN/m
\dot{W}_{out}	12.7 W per engine

existing non-ideal effects in the system. Asymmetric electrical loading across the phases will alter the magnitudes of the piston oscillations depending on the loading distribution. However, the phase relationship between phases remains unchanged. As an example, Figure 5.6 depicts a case where each of the three engines maintains its internal dissipations (e.g., fluid flow and gas spring hysteresis losses) and an external third-order load is applied to one of the phases only resulting in reduced amplitude for this phase.

Several subsystems are interacting with each other in the fabricated prototype and will be discussed in the sequel.

5.5.1 Heat Exchangers

Heat exchangers have crucial roles in a Stirling engine system. A good heat exchanger design provides a balance between fluid flow friction and heat transfer characteristics. Heat

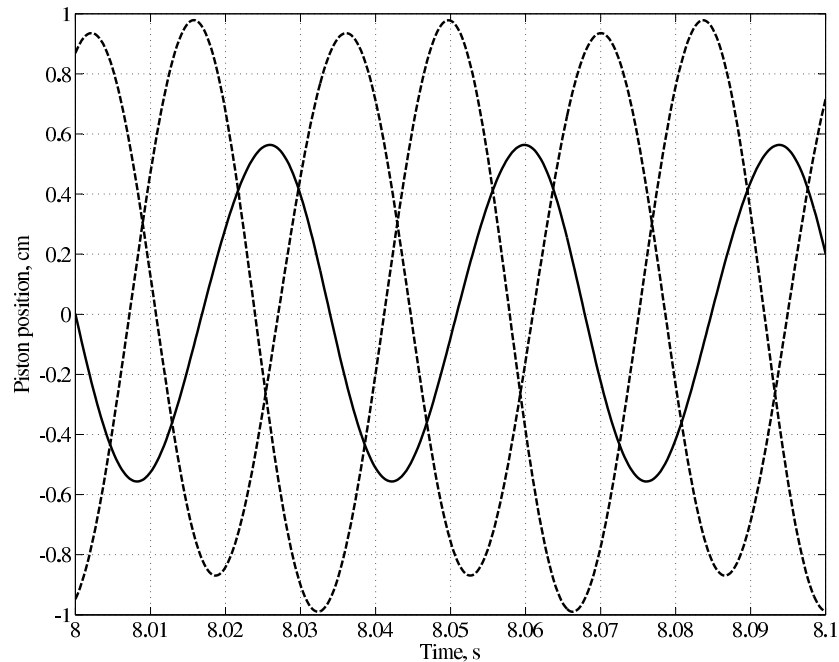


Figure 5.6: Simulation of the symmetric three-phase Stirling engine system under asymmetric electric loading condition. All three engines maintain their internal viscous and gas spring hysteresis dissipations and an external third-order load is applied to one of the phases only (shown with solid line).

exchangers with a wide frontal open area and short axial length together with an optimized hydraulic diameter are acceptable designs. Figure 5.7 shows the fabricated heat exchanger screens and the heater housing. The power resistors attached to the outside perimeter of the heater housing act as the heating source. The regenerator is a stack of woven-wire screens with circular cross-section wire, whereas the heater and cooler are stacks of etched copper screens (not woven) with square cross-section etched wire. Furthermore, in addition to its conventional sealing task, the o-ring is designed to act as a spacer between hot and cold sides of each engine to minimize the static heat loss from hot side of the engine to its cold side.

For flow friction, as discussed in chapter 3, there are several approaches suggested

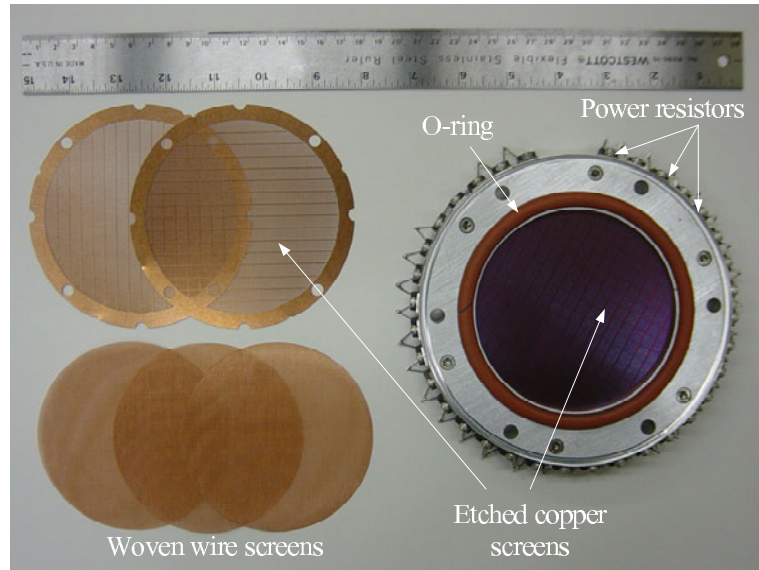


Figure 5.7: Fabricated heat exchanger frame and the screens.

in the literature. Estimated efficiencies based on Tanaka's correlation are reported in reference [41] to be higher than experimental measurements. On the other hand, since the working fluid conditions of Tanaka's experiments (e.g., temperature, pressure, fluid type, Reynolds number) fit in the range of conditions for the engine discussed here, Tanaka's correlation has been trusted in design computations.

5.5.2 Diaphragm Pistons

Mechanical friction is virtually eliminated by replacing moving pistons by diaphragms. Thus, losses associated with surface-to-surface sliding friction and lifetime limitations associated with mechanical wear are avoided. As a further consequence, lack of static friction enables the engine system to self-start upon application of heat, as discussed in section 5.4. In addition, there is no emphasis on difficult sealing requirements that have plagued Stirling designs with conventional crank-mechanism.

The piston diameter (10 cm) and excursion (1 cm) were initially chosen based on the

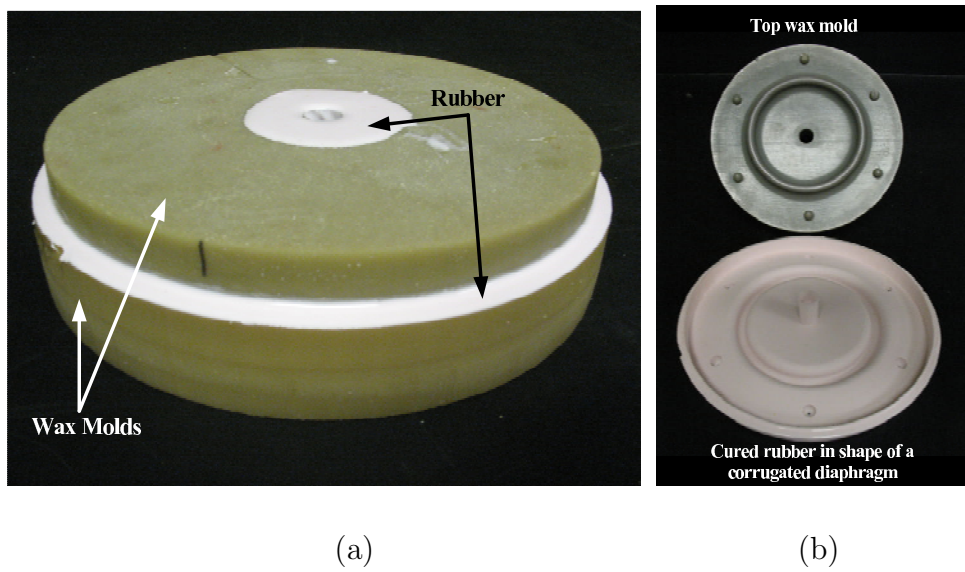


Figure 5.8: (a) Liquid rubber is cast in printed wax molds to fabricate the diaphragms. (b) Top wax mold and corrugated diaphragm after being separated from the molds.

Table 5.3: As-cured physical properties of the silicone diaphragm material.

Durometer hardness	20 points (Shore A scale)
Tensile strength	600 psi
Elongation	500%
Tear strength	125 ppi (die B)

very simple Beale analysis [33] to produce 70 W output power per engine at 50 Hz operating frequency. However, later on, in order to avoid the nonlinear stiffness of a flat diaphragm, the piston diameter was reduced to 7.6 cm to accommodate a thicker diaphragm with one ring of corrugation. This change, of course, reduced the gas spring stiffness and set the operating frequency to about 30 Hz, based on the analysis of section 5.4.

The corrugated diaphragms are fabricated by casting Dow Corning High Strength Moldmaking Silicone Rubber HSII in custom-made wax molds, which are produced by three-dimensional printers. Figure 5.8 illustrates the fabrication process and Figure 5.9 shows the trimmed diaphragm that is attached to the system. Some as-cured physical properties of this material are listed in Table 5.3.

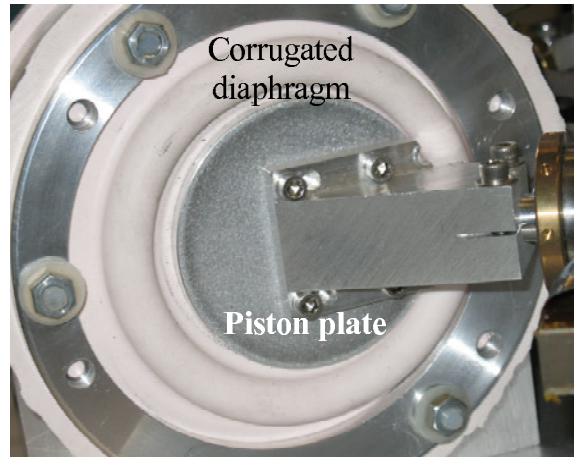


Figure 5.9: Close-up view of the fabricated diaphragm with one ring of corrugation.

5.5.3 Flexure

A rigid arm, the piston linkage, connects the expansion piston plate of one engine to the compression piston plate of the other. For each piston linkage, a bearing is realized with a nylon cantilever flexure. This flexure has to be designed to be very stiff in the axial and radial directions, but with low loss and low stiffness for angular motion. Variation of the pressure inside each engine chamber translates into force on each piston plate and a radial force component as large as 350 N is applied to the flexure in this design. The maximum or critical radial force, F_r , that the flexure can withstand before buckling is given by,

$$F_r = \left(\frac{\pi}{2.1}\right)^2 EI \frac{1}{l^2} \quad (5.29)$$

where E is the elasticity modulus of the flexure material, $I = \frac{1}{12}ht^3$ is the second moment of area, t is the flexure thickness, h is the flexure height in axial direction, and l is the flexure length in radial direction.

The flexure dimensions should be chosen such that the flexure cross sectional area is large enough to keep the radial stress well within the maximum tensile strength of

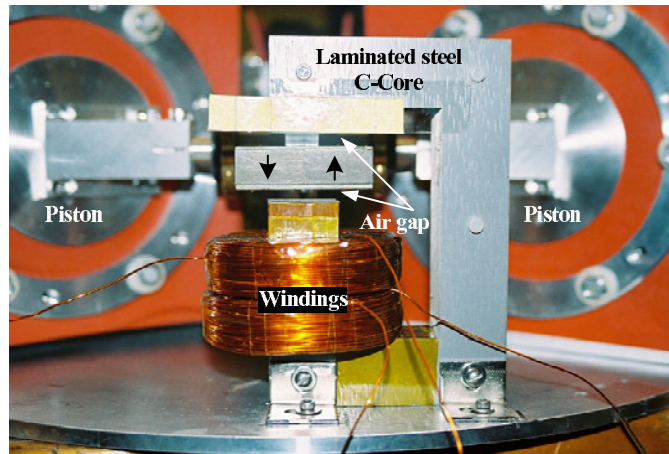


Figure 5.10: Fabricated magnetic actuator (control circuitry not shown).

the flexure material. Steel has a very high tensile strength limit. However, it is not an appropriate material choice due to its high elasticity modulus. In order to fulfill the low angular stiffness requirement, a thin sheet of steel would be required which, in turn, would not withstand the buckling force. Nylon with maximum tensile strength of about 60 MPa and elasticity modulus of about 1 GPa turns out to be a good choice of material for the three flexures. The flexure dimensions are chosen as $t = 1.3$ mm, $l = 10$ mm, and $h = 100$ mm.

5.5.4 Actuator

One of the three fabricated magnetic actuators is shown in Figure 5.10. The fabricated prototype engine is shown in Figure 5.11. Magnets are connected to the jaw that is indicated in Figure 5.11 and move as the pistons oscillate. Therefore, as a generator or motion sensor, when the pistons (and hence magnets) move, an alternating magnetic flux links the coils which, in turn, induces voltage on the winding terminals. On the other hand, as an actuator, when alternating current flows through the windings, the resulting electromagnetic force pushes the magnet pair back and forth depending on the direction of the current flow.

Actuators are connected to a variable frequency three-phase inverter. Hence, in ad-

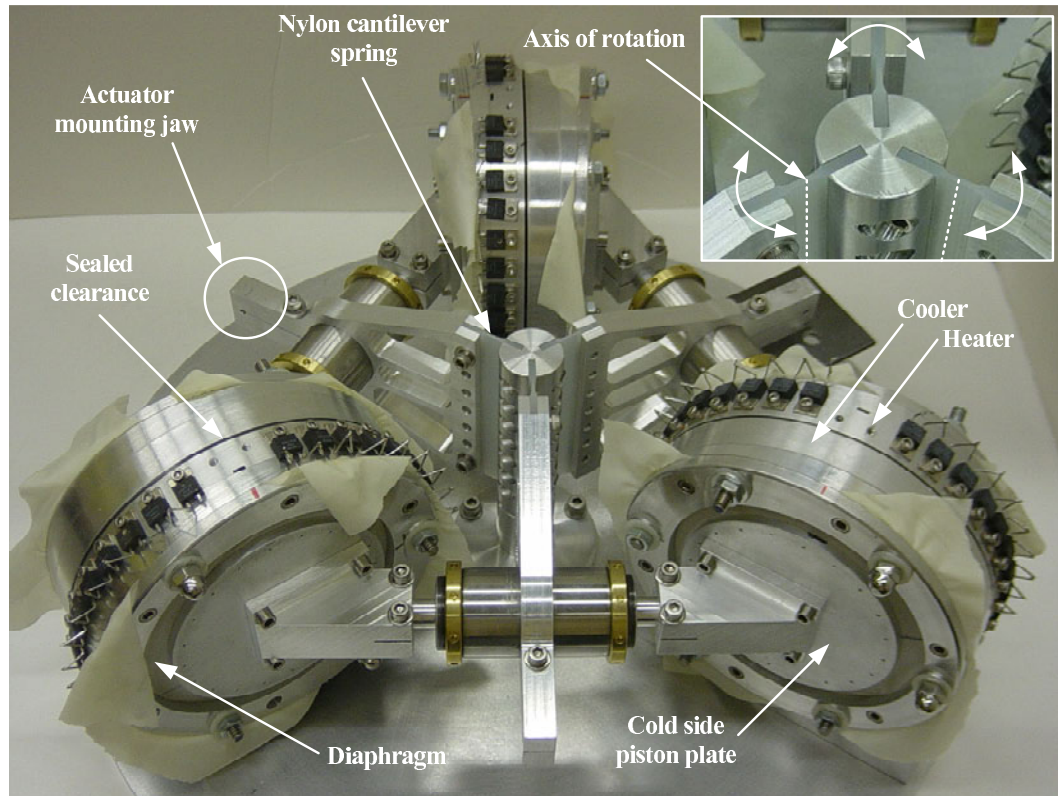


Figure 5.11: Fabricated three-phase Stirling engine system. Photograph taken before custom corrugated silicone diaphragms were fabricated and installed.

dition to driving the system in heat pump regime, each Stirling engine may be driven (as an alpha-type machine) in pure displacement or compression modes using two actuators only, if mechanically separated from the other two phases. The latter two driving modes are particularly useful while assessing the fluid flow and gas spring hysteresis losses, respectively.

5.6 Experimental Results

This section summarizes the experimental results obtained with the symmetric three-phase Stirling engine system. The following methodologies have been implemented in assessment of the prototype:

- *Ring-Down Test*

A ring-down test is an appropriate way for estimating the various parameters of a simple dynamical system. The system is displaced from its equilibrium and is released. By looking at the rate and type of the envelope (exponential for viscous friction or linear for dry friction,) one can translate it into important system parameters such as natural frequency, quality factor and damping factor, which are then used to estimate the power loss.

- *Calorimetric Transient Test*

Any loss within a component generates heat and, therefore, has the potential of increasing the temperature of that component. In a calorimetric test, the temperature transient behavior is observed while the component runs in the desired operating conditions. An estimation algorithm is then utilized to estimate the amount of the generated heat (i.e., the loss within that component). This algorithm is based upon a thermal model that is developed for the component and its surrounding environment. It should be noted that accurate knowledge of a component thermal mass is a key point in this test. Since obtaining a priori accurate values of thermal resistance is very difficult, equivalent thermal dissipation is extracted from the temperature transient characterized by the estimation process.

5.6.1 Fluid Flow Friction

The ring-down test turns out to be the most appropriate method to evaluate frictional losses. Figure 5.12 shows the ring-down test for one of the three nylon cantilever hinges. In order to assess the feasibility of the designed flexure, none of the diaphragms (nor the heat

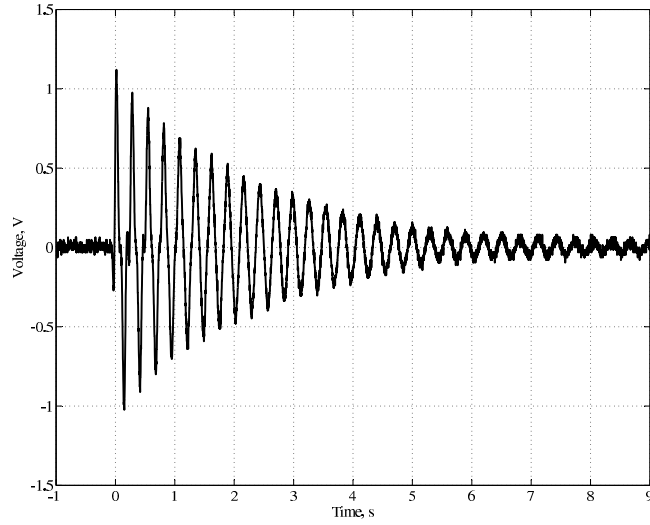


Figure 5.12: Ring-down characteristic of the nylon flexure.

exchangers) are linked in this experiment. As described in appendix A one can conclude that the natural frequency of the mass-spring system is about 3.7 Hz. This is a function of the flexure stiffness and the equivalent moving mass. The quality factor is about 26.7 which is an indication of minimal losses in the designed nylon flexure, as discussed below.

Table 5.4 tabulates resonant frequency, f_r , quality factor, Q , and damping factor, D , of the ring-down tests that were carried out for various cases to estimate the contribution of each component on the overall system behavior, and in particular, power dissipation. The nylon flexure stiffness is about 350 N/m based on a separate measurement. Therefore, the equivalent moving mass is about 0.64 kg, which enables calculation of the dissipated power loss at design excursion of 1 cm. This data is tabulated in column $\overline{W}_{loss}^{meas}$ and the estimated dissipation at the 29.4 Hz operating frequency is listed in column $\overline{W}_{loss}^{est}$.

The nylon flexure, the diaphragms, and the magnetic stiffness of the actuator are the three components that contribute to the overall stiffness of the mass-spring system with the actuator stiffness being dominant which basically sets the frequency of the displacement

Table 5.4: Summary of the ring-down tests carried out on the prototype. On each row the cross sign indicates which components were included in the test. F, D, K, H, R, and C refer to flexure, diaphragm, cooler, heater, regenerator, and C-core (actuator laminated steel core shown in Figure 5.10), respectively.

F	D	K	H	R	C	f_r , Hz	Q	D , N.s/m	$\overline{\dot{W}}_{loss}^{meas}$, W at f_r	$\overline{\dot{W}}_{loss}^{est}$, W at 29.4 Hz
×						3.7	26.7	0.56	0.02	0.96
×	×	×				7.5	10.8	2.78	0.31	4.74
×	×	×	×			7.5	8.9	3.42	0.38	5.84
×	×	×	×	×		7.5	6.3	4.80	0.53	8.19
×					×	10.2	65.4	0.62	0.13	1.06
×	×	×			×	11.9	19.3	2.49	0.70	4.25
×	×	×	×		×	11.9	17.4	2.76	0.77	4.71
×	×	×	×	×	×	11.9	9.5	5.07	1.42	8.65

Table 5.5: Comparison of the measured flow friction data with designed values for heater and regenerator.

f , Hz	$\overline{\dot{W}}_{H, loss}^{calc}$, W	$\overline{\dot{W}}_{H, loss}^{meas}$, W	$\overline{\dot{W}}_{R, loss}^{calc}$, W	$\overline{\dot{W}}_{R, loss}^{meas}$, W
7.5	0.04	0.07	0.65	0.15
11.9	0.13	0.07	1.7	0.65
29.4	1.2	0.46-1.1	7	2.35-3.94

mode operation of the system to about 11.9 Hz.

We can infer the fluid flow loss contribution of the heater, cooler, and the regenerator at two frequencies (i.e., 7.5 Hz and 11.9 Hz) from Table 5.4. A comparison of the measured data for regenerator with the design values, Table 5.5, signifies that the flow friction correlations suggested by Tanaka [41] for oscillating flow are reliable and even conservative. Hence, using such reliable correlations one can be confident that the fabricated machine will not suffer from unexpected excessive flow friction.

5.6.2 Heat Pump Operation

A calorimetric transient test is an appropriate method for measuring the amount of the pumped heat in this mode of operation. In a calorimetric test, as stated before, the system

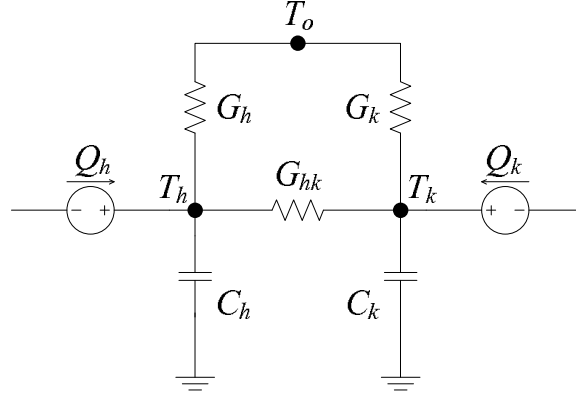


Figure 5.13: Electric circuit analogue for the thermal model of the prototype while operating as heat pump.

runs under the desired operating conditions and the injected and rejected heats at either side of the engines are estimated based on the observed temperature transient behavior. Figure 5.13 shows the electric analogue of a simple thermal model for one of the engines. Variables T_h , T_k , and T_o are, respectively, the hot side, cold side, and ambient temperatures. The thermal masses of the hot side and the cold side of the engine are represented by C_h and C_k , respectively. G_h and G_k are conductances that model the thermal dissipation at the hot and cold sides, respectively. Conductance G_{hk} models the thermal losses that are the result of temperature difference between the hot and the cold sides of the engine. Lastly, Q_h and Q_k are the injected (or rejected) heat at either side of the engine and are assumed constant during the transient. The continuous-time dynamics of this system is represented as,

$$\begin{bmatrix} C_h & 0 \\ 0 & C_k \end{bmatrix} \begin{bmatrix} \dot{\tilde{T}}_h \\ \dot{\tilde{T}}_k \end{bmatrix} = \begin{bmatrix} G_h + G_{hk} & -G_{hk} \\ -G_{hk} & G_k + G_{hk} \end{bmatrix} \begin{bmatrix} \tilde{T}_h \\ \tilde{T}_k \end{bmatrix} + \begin{bmatrix} -1 & 0 \\ 0 & -1 \end{bmatrix} \begin{bmatrix} \dot{Q}_h \\ \dot{Q}_k \end{bmatrix} \quad (5.30)$$

or

$$\mathbf{C}\dot{\mathbf{x}}_c = \mathbf{A}\mathbf{x}_c + \mathbf{B}\mathbf{u} \quad (5.31)$$

where

$$\tilde{T}_h = T_h - T_o \quad (5.32)$$

$$\tilde{T}_k = T_k - T_o \quad (5.33)$$

In this experiment the temperatures are sampled at a sampling period of T_s . Therefore, the following discrete-time representation is used for the sampled-data system:

$$\begin{bmatrix} T_h^{n+1} \\ T_k^{n+1} \end{bmatrix} = \mathbf{A}_d \begin{bmatrix} T_h^n \\ T_k^n \end{bmatrix} + \mathbf{B}_d \mathbf{u} \quad (5.34)$$

where $n \in \{1, \dots, N_s\}$ corresponds to the sample number. For an experiment with N_s sampled data, we have,

$$\begin{bmatrix} T_h^2 & T_k^2 \\ T_h^3 & T_k^3 \\ \vdots & \vdots \\ T_h^{N_s} & T_k^{N_s} \end{bmatrix} = \begin{bmatrix} T_h^1 & T_k^1 & 1 \\ T_h^2 & T_k^2 & 1 \\ \vdots & \vdots & \vdots \\ T_h^{N_s-1} & T_k^{N_s-1} & 1 \end{bmatrix} \left[\mathbf{A}_d \mid \mathbf{B}_d \mathbf{u} \right]^T \quad (5.35)$$

or

$$\mathbf{Y} = \mathbf{Z} \left[\mathbf{A}_d \mid \mathbf{E} \right]^T \quad (5.36)$$

where matrices \mathbf{Y} and \mathbf{Z} are constructed based on the recorded samples. Utilizing the least squares estimation method, we have,

$$\left[\mathbf{A}_d \mid \mathbf{E} \right]^T = \mathbf{Z} \setminus \mathbf{Y} \quad (5.37)$$

where \backslash denotes the least squares operator. After extracting matrices \mathbf{A}_d and \mathbf{E} from Eq. (5.37), \mathbf{B}_d is computed as,

$$\mathbf{B}_d = \left(\int_0^{T_s} e^{\mathbf{A}_c \tau} d\tau \right) \mathbf{C}^{-1} \mathbf{B} = - \left(\int_0^{T_s} e^{\mathbf{A}_c \tau} d\tau \right) \mathbf{C}^{-1} \quad (5.38)$$

where

$$\mathbf{A}_d = e^{\mathbf{A}_c T_s} \quad (5.39)$$

$$\mathbf{A}_c = \mathbf{C}^{-1} \mathbf{A} \quad (5.40)$$

And finally \mathbf{u} is calculated as,

$$\mathbf{u} = \mathbf{B}_d^{-1} \mathbf{E} \quad (5.41)$$

As is implied by Eqs. (5.38) and (5.40), accurate knowledge of the thermal masses is a key point in this test. Since obtaining a priori accurate values of thermal resistance is very difficult, equivalent thermal dissipation is extracted from the estimated matrix \mathbf{A} in Eq. (5.40).

By driving all three actuators with a balanced symmetrical three-phase power supply, the system operates as a heat pump. Figure 5.14 shows the temperature variation for both cold and hot sides of a single unit of the three-phase Stirling engine. The system operated in heat pump regime for about 53 minutes during which temperatures of the hot and cold sides separated from their initial thermal equilibrium in two opposite directions. Actuators are tuned off at $t = 53$ minutes, which allows the temperatures to converge back to their

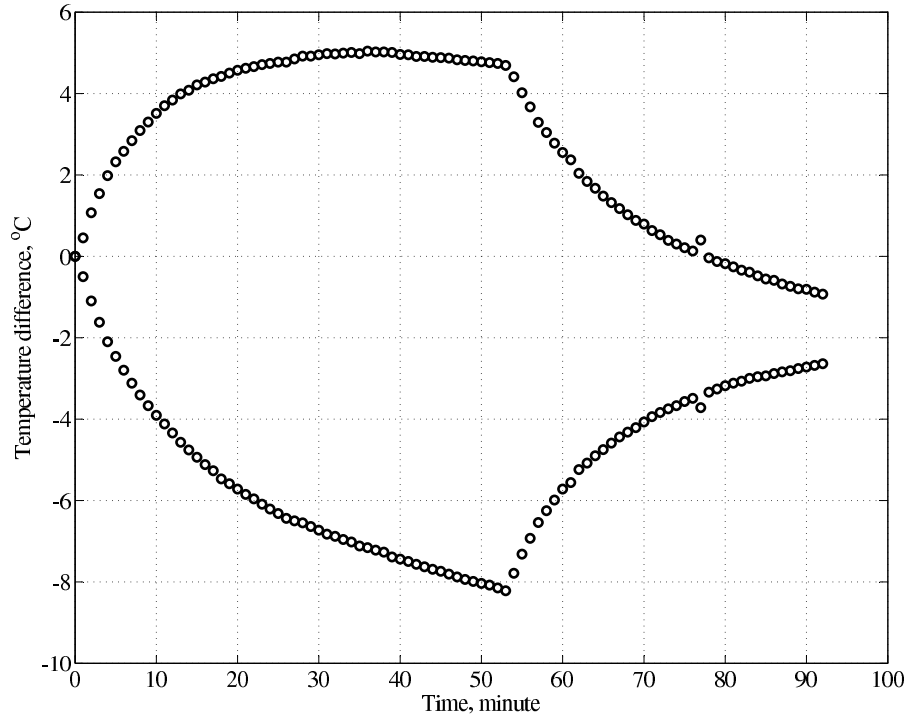


Figure 5.14: Temperature variation of the hot and cold sides of one Stirling engine during the heat pump regime.

equilibrium. The forgoing algorithm estimates

$$\dot{Q}_h = 15.6 \text{ W} \quad (5.42)$$

$$\dot{Q}_k = -16.1 \text{ W} \quad (5.43)$$

In the above analysis $|Q_k| > |Q_h|$ likely due to unmodeled thermal mass on the “hot” side.

The actuator electrical input power in this experiment is 44 W with a copper loss of about 37 W in the actuator windings. Only a quarter of the regenerator screens are installed in this experiment. Therefore, since the regenerator has the largest contribution to the flow friction (see Table 5.4) and the pistons are operating at about half of their nominal

Table 5.6: Comparison of measured and calculated gas spring hysteresis (compression) losses in various conditions. The number in the left three columns indicate the fraction of corresponding heat exchanger screens that is in place.

Heater	Cooler	Regen.	f , Hz	Piston stroke, mm	$\overline{\dot{W}}_{hys}^{calc}$, W	$\overline{\dot{W}}_{hys}^{meas}$, W
0%	0%	0%	28.2	12	2.3	2
50%	50%	0%	29.2	12	2.6	2.6
100%	100%	0%	29.6	13	3.7	3.7
50%	50%	50%	30	6	0.7	0.7

excursion, the fluid flow dissipation is expected to be about 1.5 W. On the other hand, since the temperature separation at the hot and cold sides of the engine (Figure 5.14) is very little, the input work needed to effect heat pumping is negligible. Hence, a different source of dissipation exists that consumes the remaining 4.5 W, which was not considered at the design stage. The gas spring hysteresis is this mysterious dissipation source that is discussed in the sequel.

5.6.3 Gas Spring Hysteresis

The calorimetric test proved to be an appropriate method for the measurement of the gas hysteresis dissipation as well. A single engine phase is actuated at its pure compression resonant frequency (about 30 Hz) and, hence, the pistons are 180° out of phase with respect to each other. Under this condition, the working fluid is virtually not flowing through the heat exchangers. therefore, the measured dissipation is solely related to the gas spring hysteresis. In order to observe the effect of the heat exchanger on gas spring hysteresis, four different conditions have been considered as tabulated in Table 5.6. The outlined estimation algorithm in a calorimetric test is then utilized to estimate the amount of the generated heat (i.e., the loss within that component). In each case, a slightly different resonant frequency was observed for the compression mode that is due to the different

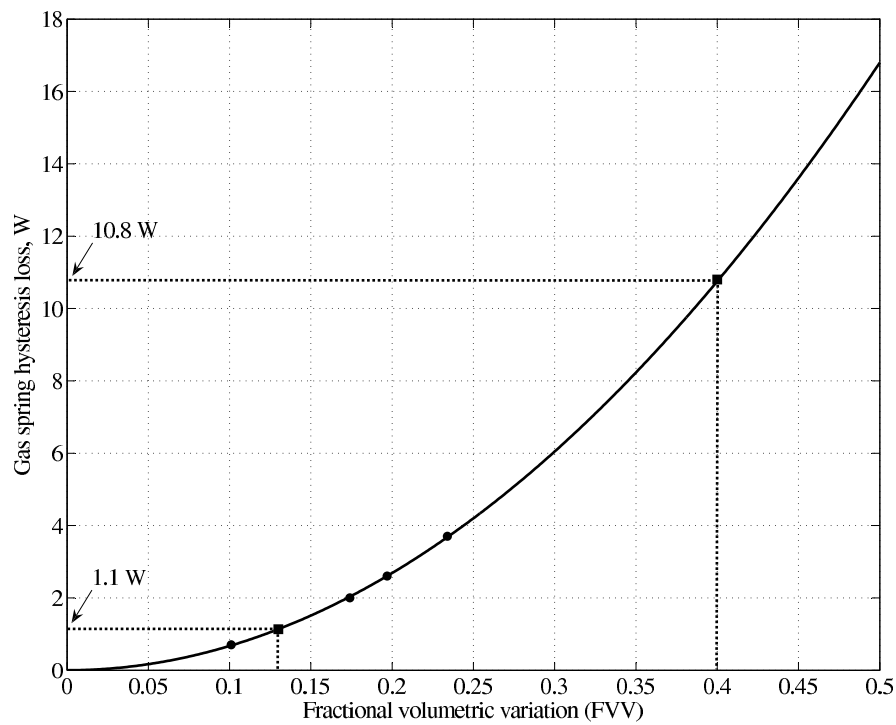


Figure 5.15: Gas spring hysteresis loss versus fractional volumetric variation. The graph is a quadratic regression through the measured points (shown in dots) taken from Table 5.6.

volume of gas that is enclosed by the engine chamber. As one may expect, the measured data confirms that by decreasing the working gas volume (adding more screens inside the engine), the gas spring stiffness increases which, in turn, raises the resonant frequency.

In Table 5.6, the measured gas spring hysteresis loss has been compared with the suggested formulation in chapter 3. This result confirms the accuracy of the calculation and provides a reliable basis for estimation of the compression losses that plays a crucial role in the operation of free-piston Stirling engines. The measured data points are plotted in Figure 5.15 versus fractional volumetric variation, and a quadratic curve fit through those data validates the theoretical modeling of the gas spring hysteresis dissipation discussed in chapter 3.

5.6.4 Engine Operation

The gas spring hysteresis dissipation was not initially considered in the design and it turns out that it is an important dissipation phenomenon and should be carefully addressed in the low-power Stirling engine design as it hindered the operation of the test system in engine mode. At steady state, the phase delay between the two pistons of each Stirling engine is intended to be 120 degrees. This condition translates into a fractional volumetric variation of about 0.4 for the working fluid inside the engine chamber. Hence, as shown in Figure 5.15, the gas spring hysteresis loss would be about 10.8 W. This figure corresponds to a damping factor of about 6.1 N.s/m, according to the discussions in chapter 3. From a power balance point of view, the total losses in the system (i.e., viscous friction and gas spring hysteresis dissipation) is about 19.5 W per engine, which actually surpasses the nominal output power of 12.7 W. On the other hand, with a total damping factor of 11.2 N.s/m, according to Eq. (5.28), the start-up temperature is about 175 °C. A direct numerical calculation of the eigenvalues of the linearized system, as depicted in Figure 5.16, confirms the accuracy of the derived expression in Eq. (5.28). In addition to being significantly higher than the design temperature, the required start-up temperature surpasses the operating temperature limit of the rubber diaphragm (diaphragm material releases toxic gases at temperatures above 150 °C). The computed start-up temperature is about 87 °C considering the viscous dissipation only.

In order to decrease the gas spring hysteresis dissipation, as described in chapter 3, reduction of fractional volumetric variation is the most effective strategy. If the fabricated engines (six of them) are assembled together in a six-phase system, the phase delay between the pistons of each engine becomes 60°. This will reduce the fractional volumetric variation

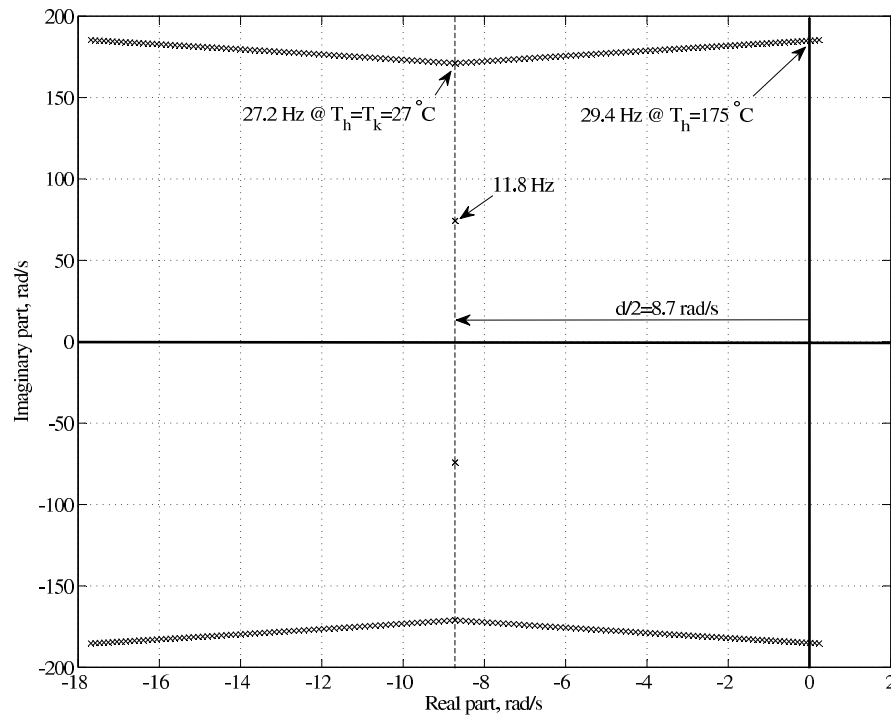


Figure 5.16: Progression of the eigenvalues of the symmetric three-phase Stirling engine system toward the unstable region as the hot side temperature increases. At $T_h = 175$ °C the system becomes self-starting.

to 0.13, which reduces the gas spring hysteresis losses by an order of magnitude to 1.1 W, according to Figure 5.15. In addition, the operating frequency drops to about 19.4 Hz, which further decreases the gas spring hysteresis dissipation to 0.9 W and the viscous losses to 3.7 W. Therefore, the total damping factor is 6.3 N.s/m, which corresponds to a start-up temperature of about 79 °C (refer to appendix C for details). From the power balance point of view, the indicated output power in this case is about 10 W with a total dissipation of 4.6 W. These figures confirm the possibility of operation in engine mode.

Therefore, attempting a six-phase system is very interesting and promising. However, it is even more interesting if the kinematics of a symmetric three-phase system is slightly modified to force the pistons of each engine to oscillate with a 60° phase delay instead of

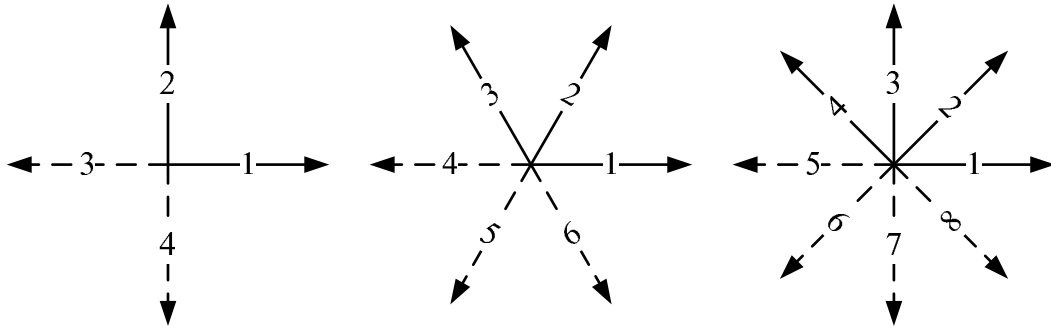


Figure 5.17: Phasor diagram for three examples of multi-phase Stirling engine systems with four, six, and eight phases. Each vector represents position of one piston. Dashed vectors are representative of the pistons that can be eliminated by utilizing a reverser.

the classical 120° . Such a system will have half of the parts (moving or not) that otherwise would be required for a successful operation. The following section introduces what is called a “reverser” in this dissertation and provides the required theoretic background for dynamical analysis of a multi-phase Stirling engine that utilizes a reverser.

5.7 Reverser Modeling and Analysis

Gas hysteresis loss is an important dissipation phenomenon for low-temperature free-piston Stirling engines [33, 56]. Increasing the number of phases in a multi-phase system reduces the phase delay between the pistons of each engine. This change, in turn, decreases the fractional volumetric variation inside each engine chamber, which translates into lower gas hysteresis loss.

For the fundamental mode of an N -phase system ($N > 3$) with even number of phases, there are $N/2$ pairs of pistons with equal and opposite trajectories. Figure 5.17 depicts the phasor diagrams for three examples of multi-phase systems. In such cases, by utilizing a reversing mechanism for one of the pistons, half of the engine chambers can be eliminated without altering the phase relationship between the remaining pistons.

Figure 5.18 shows the schematic diagram of a multi-phase Stirling engine system with the r -th piston acting as a reverser. Newton's second law for the reversing piston is expressed as Eq. (5.44) which can be substituted in Eq. (5.6) to define the nonlinear dynamical behavior of a multi-phase Stirling engine system that is equipped with a reverser.

$$A_P(p_{r-1} + p_r - 2p_o) - f_P(\dot{x}_r) - K_P x_r = m_P \ddot{x}_r \quad (5.44)$$

where p_o is the ambient or bounce space pressure. It should be noted that, due to the reversing mechanism of piston r , we have,

$$V_{e,r} = V_e^{nom} + A_P x_r \quad (5.45)$$

However, for all other expansion and compression volumes, Eqs. (5.3) and (5.4) are still valid.

Therefore, in a system where the r -th piston is a reverser, Eq. (5.7) should be replaced by Eq. (5.46) for the r -th piston and by Eq.(5.47) for the $(r + 1)$ -th piston, respectively.

$$\ddot{x}_r = \left(\frac{\alpha}{m_P} \frac{1}{T_h} \right) x_{r-1} - \left(\frac{\alpha}{m_P} \frac{1}{T_h} + \frac{\alpha}{m_P} \frac{1}{T_k} + \frac{K_P}{m_P} \right) x_r - \left(\frac{\alpha}{m_P} \frac{1}{T_k} \right) x_{r+1} - d\dot{x}_r \quad (5.46)$$

$$\ddot{x}_{r+1} = - \left(\frac{\alpha}{m_P} \frac{1}{T_h} \right) x_r - \left(\frac{\alpha}{m_P} \frac{1}{T_h} + \frac{\alpha}{m_P} \frac{1}{T_k} + \frac{K_P}{m_P} \right) x_{r+1} + \left(\frac{\alpha}{m_P} \frac{1}{T_k} \right) x_{r+2} - d\dot{x}_{r+1} \quad (5.47)$$

Hence, the linearized dynamics of an N -phase Stirling engine system with piston $r < N$ as the reverser can still be represented by Eq. (5.10) if the element $(r, r + 1)$ of the stiffness matrix is replaced with $+b$ and the element $(r + 1, r)$ is replaced with $+c$.

If the second linkage of a symmetric three-phase Stirling system is replaced with a

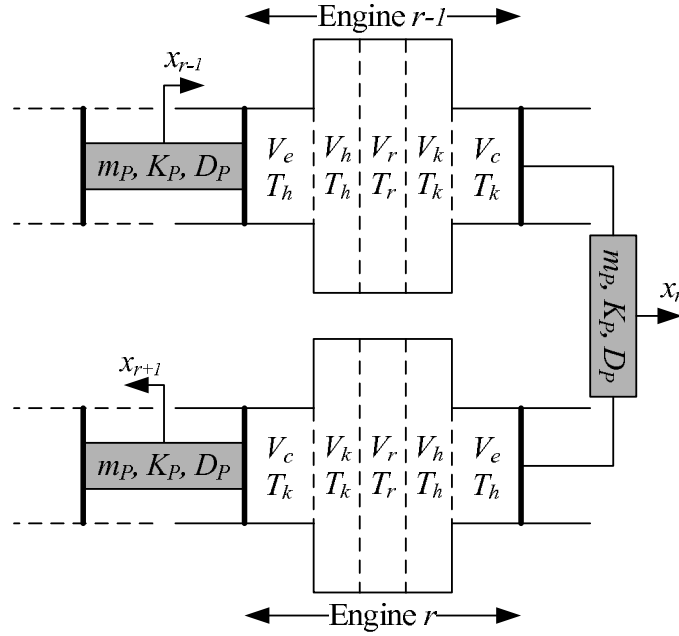


Figure 5.18: Schematic diagram of a multi-phase Stirling engine system that incorporates a reversing mechanism within piston r .

reverser (i.e., $r = 2$), matrix \mathbf{K} in Eq. (5.14) becomes,

$$\mathbf{K} = \begin{bmatrix} \frac{K_P}{m_P} + (b + c) & -b & -c \\ -c & \frac{K_P}{m_P} + (b + c) & +b \\ -b & +c & \frac{K_P}{m_P} + (b + c) \end{bmatrix} \quad (5.48)$$

By applying the transformation $\mathbf{x} = \mathbf{Tz}$, where,

$$\mathbf{T} = \begin{bmatrix} -1 & 0 & 1 \\ 1 & \sqrt{3}/2 & 1/2 \\ 1 & -\sqrt{3}/2 & 1/2 \end{bmatrix} \quad (5.49)$$

the state-state representation of the system becomes,

$$\begin{bmatrix} \ddot{z}_1 \\ \ddot{z}_2 \\ \ddot{z}_3 \end{bmatrix} + d \begin{bmatrix} \dot{z}_1 \\ \dot{z}_2 \\ \dot{z}_3 \end{bmatrix} + \begin{bmatrix} \frac{K_P}{m_P} + 2(b+c) & 0 & 0 \\ 0 & \frac{K_P}{m_P} + \frac{1}{2}(b+c) & -\frac{\sqrt{3}}{2}(b-c) \\ 0 & \frac{\sqrt{3}}{2}(b-c) & \frac{K_P}{m_P} + \frac{1}{2}(b+c) \end{bmatrix} \begin{bmatrix} z_1 \\ z_2 \\ z_3 \end{bmatrix} = 0 \quad (5.50)$$

which simply reveals the following three eigenvalues for the stiffness matrix,

$$\mu_1 = \frac{K_P}{m_P} + 2(b+c) \quad (5.51)$$

$$\mu_{2,3} = \left(\frac{K_P}{m_P} + \frac{1}{2}(b+c) \right) \pm j \frac{\sqrt{3}}{2}(b-c) \quad (5.52)$$

It is very interesting to note that none of the modes associated with the three-phase system are present here. However, the modes are identical to a subset of the modes of a six-phase system that are discussed in appendix C. Based on that discussion, μ_1 represents the “pure compression” mode. The remaining two eigenvalues correspond to the “forward” and “backward” six-phase operation of the system. This guarantees a 60° phase delay between the pistons of each engine in a three-phase system that utilizes a reverser.

Following a similar approach to the symmetric three-phase case, the relationship between the damping factor and start-up temperature becomes,

$$\frac{1}{T_h} = \frac{1}{T_k} - \frac{d}{\alpha} \sqrt{\frac{4}{3} m_P (K_P + K_G)} \quad (5.53)$$

which indicates that both the resonant frequency and start-up temperature of this system will be lower than its symmetric three-phase counterpart. Based on this analysis, an op-

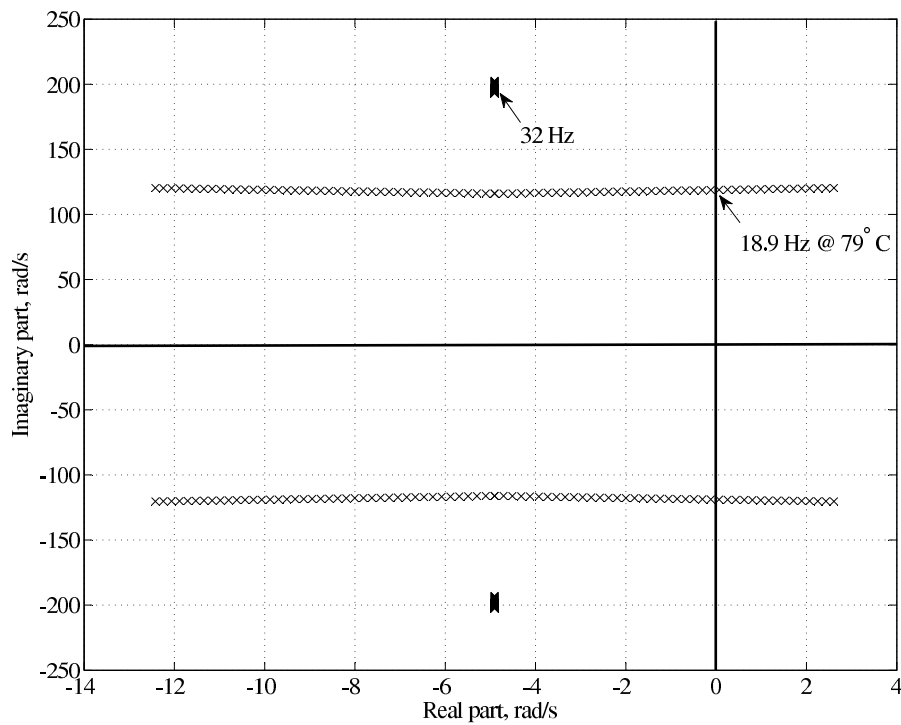


Figure 5.19: Progression of the eigenvalues of three-phase Stirling engine with reverser toward the unstable region as the hot side temperature increases. At $T_h = 79\text{ }^\circ\text{C}$ the system becomes self-starting.

erating resonant frequency of 19 Hz and start-up temperature of $79\text{ }^\circ\text{C}$ is estimated for the revised system. The eigenvalue loci of the three-phase Stirling engine system with reverser is shown in Figure 5.19 and the simulation result of the same system is depicted in Figure 5.20.

5.8 Reverser Implementation

Figure 5.21 illustrates the implementation of a reverser system within the fabricated prototype. The rigid rods are very light tubes to help the system retain its symmetry (i.e., equal mass and external stiffness for all three engines). All three heaters of the system are

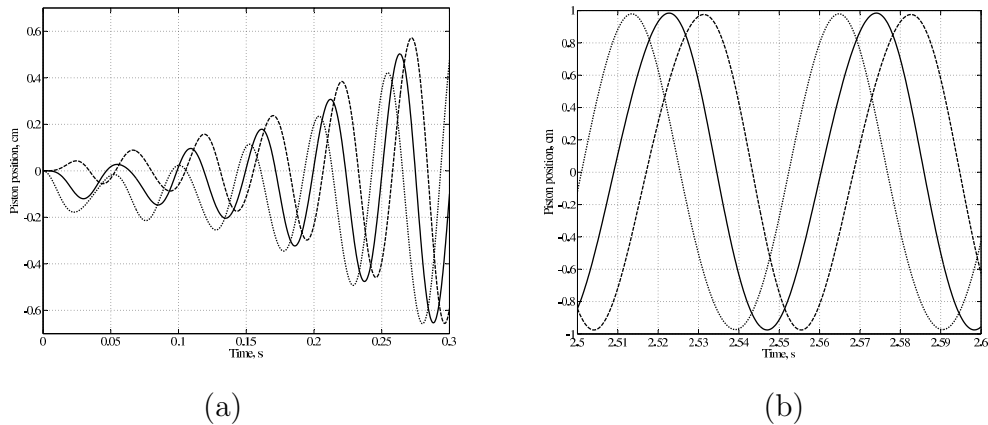


Figure 5.20: Simulated piston positions of the three-phase system with reverser. (a) Startup (b) Steady state.

heated by an electric heater that is wrapped on their outer perimeter. As the expansion space temperature rises, the system exhibits higher quality factor if examined by ring-down test. As soon as the temperature reaches about $100\text{ }^{\circ}\text{C}$ the engine starts. Note that the cold side temperature is about $40\text{ }^{\circ}\text{C}$. In this condition, the estimated start-up temperature is $94\text{ }^{\circ}\text{C}$.

Figure 5.22 depicts the recorded acceleration signals of the three phases at small excursions. The extracted fundamental frequency components of the acceleration signals are shown in Figure 5.23. The signals show an oscillation frequency of about 16 Hz and 60° phase delays between the three phases as expected. At large excursions, the pistons oscillate at magnitudes of about 0.7 cm according to Figure 5.24.

5.9 Conclusions

Mathematical modeling of multi-phase Stirling engine systems was presented in this chapter. A symmetric three-phase system was discussed in detail based on eigen-analysis of the corresponding linearization. This analysis proved the self-starting potential of multi-

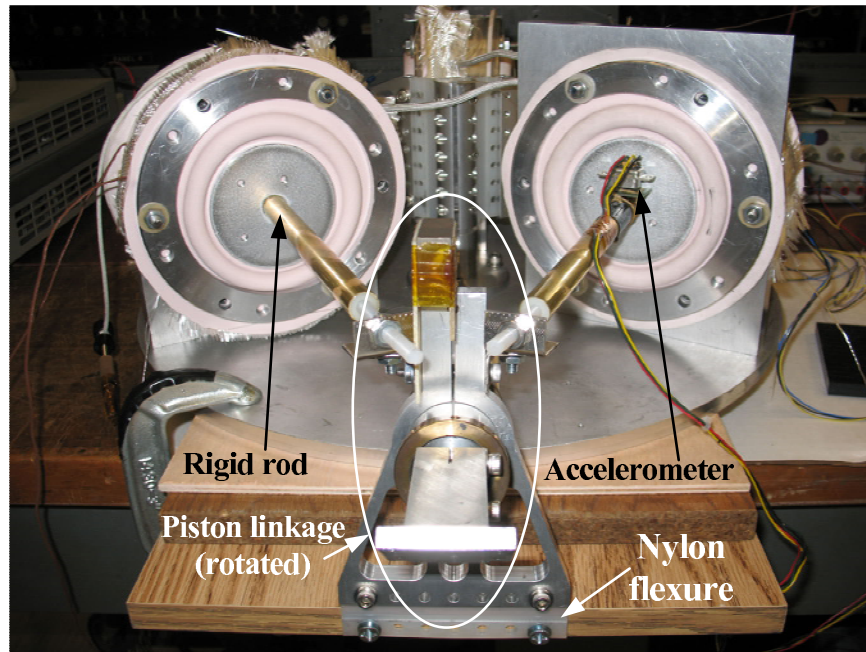


Figure 5.21: Implementation of reverser mechanism within the fabricated three-phase Stirling engine prototype.

phase systems relying on Hartman-Grobman theorem and indirect method of Lyapunov. The start-up temperature of the heater at which the system starts its operation was derived based on the same modal analysis.

Design, fabrication, and test of a symmetric three-phase free-piston Stirling engine system were discussed as well. The system was designed to operate with moderate-temperature heat input that is consistent with solar-thermal collectors. Diaphragm pistons and nylon flexures are considered for this prototype to eliminate surface friction and provide appropriate seals. The experimental results were presented and compared with design calculations. Tests confirmed the design models for heat exchanger flow friction losses and gas spring hysteresis dissipation. However, it was revealed that gas spring hysteresis loss was an important dissipation phenomenon for low-power systems, and should be carefully addressed in design as it hindered the operation of the symmetric three-phase prototype.

Analysis showed that the gas hysteresis dissipation could be reduced drastically by

increasing the number of phases in a system with a little compromise on the operating frequency and, hence, the output power. It was further shown that for an even number of phases (greater than 5), half of the pistons could be eliminated by utilizing a reverser. By introducing a reverser to the fabricated system, the system proved its self-starting capability in engine mode and validated the derived expression for computing the start-up temperature.

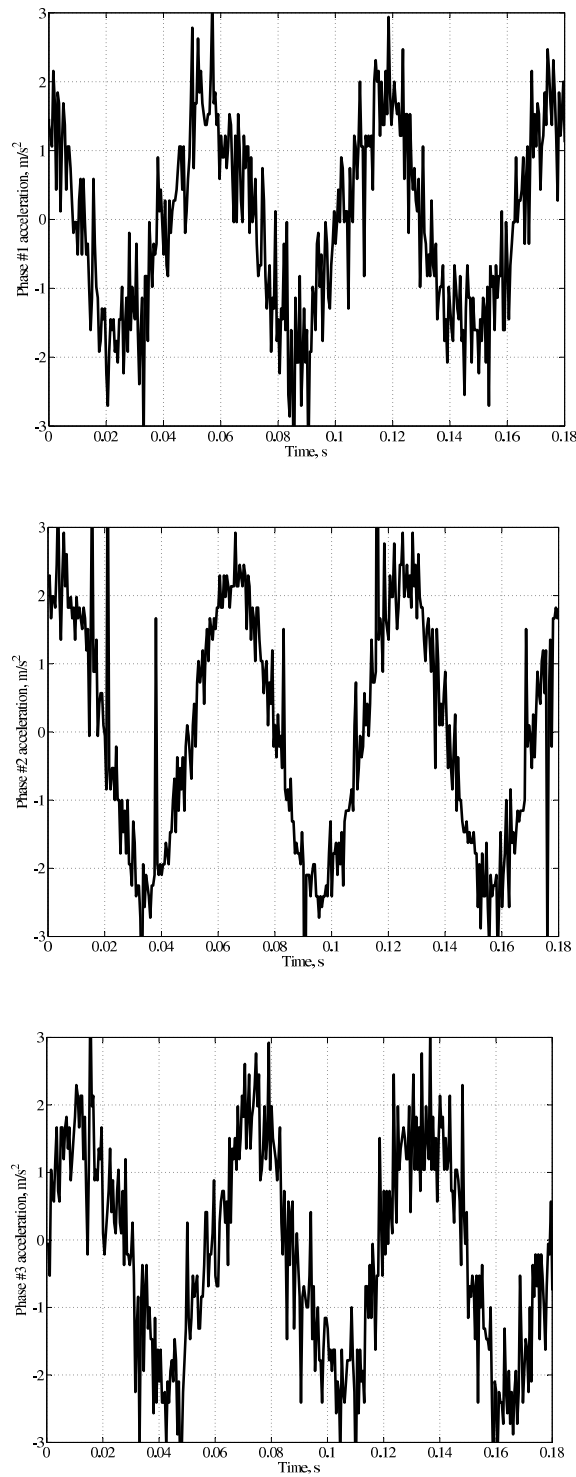


Figure 5.22: Recorded acceleration signals of the three phases in the revised three-phase Stirling engine system.

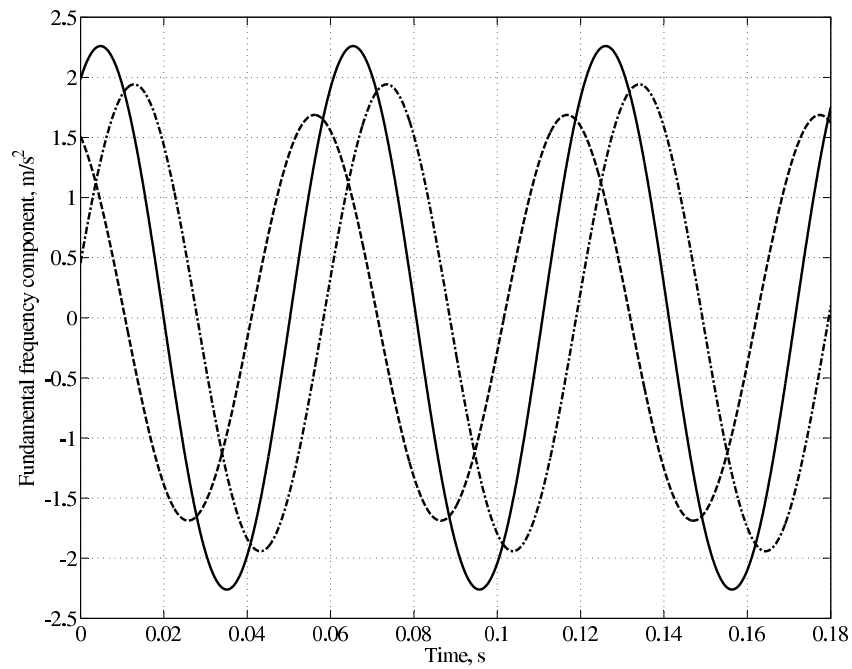


Figure 5.23: Fundamental frequency components of the three acceleration signals. Compare to Figure 5.20(b).

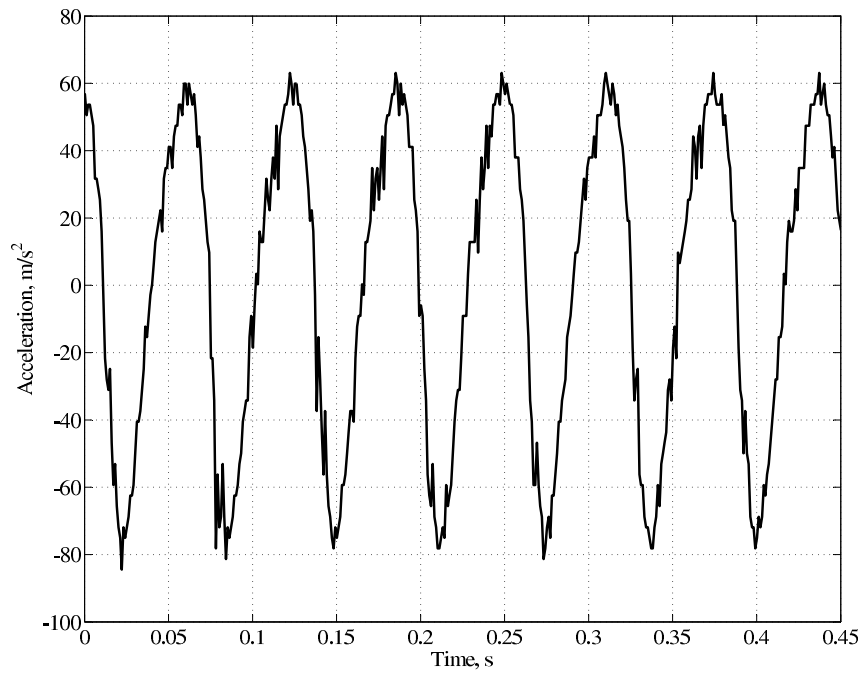


Figure 5.24: Acceleration signal of one piston at full-amplitude oscillation.

Chapter 6

Conclusions

A promising case for the use of distributed solar-thermal-electric generation was outlined in this dissertation, based on low temperature-differential Stirling engine technology in conjunction with state-of-the-art solar thermal collectors. Although the predicted efficiencies are modest, the estimated cost in \$/W for large scale manufacturing of these systems is quite attractive in relation to conventional photovoltaic technologies. Considering that the solar to thermal energy conversion is a mature technology, the main purpose of this dissertation was to understand the operation of the Stirling thermodynamic cycle at moderate temperatures and to identify the associated challenges.

A low-power single-phase Gamma-type free-piston Stirling engine engine prototype was designed and fabricated as part of the conducted research work. This prototype incorporates an electrically driven displacer, which is actuated independent of the power piston, hence the name free-piston. It is a resonant mass-spring system and the stiffness is provided by a magnetic spring system. The magnetic spring system is based on permanent magnets. The specific implementation method, significantly reduces the eddy currents and the

associated power dissipation which, in turn, improves the quality factor. In addition, this spring exhibits a highly linear stiffness characteristic over its full stroke. A linear stiffness characteristic is essential to avoid the complexities associated with frequency tuning. In this prototype, the power piston is not mechanically linked to the displacer piston. It forms a mass-spring resonating subsystem with the gas spring and has resonant frequency matched to that of the displacer. The displacer piston, cylinders, and heat exchangers frame are fabricated from plastic materials. The fluid flow friction and the gas spring hysteresis losses were identified as the major dissipation sources in this system. Extensive experimentation on individual component of the fabricated engine confirmed the theoretical models and design considerations, providing a sound basis for higher power Stirling engine designs.

Existing commercial Stirling engines are used for various applications such as NASA's deep-space missions, submarine power systems, solar dish-Stirling systems, cryocooling, etc. They are mostly high-temperature single-phase Beta-type machines. Multi-phase Stirling engine systems are particularly interesting because they are comprised of Alpha-type Stirling engines and, hence, eliminate the need for a displacer piston and the associated design and control challenges. A detailed dynamical model of multi-phase free-piston Stirling engine systems was discussed in this dissertation. The mathematical model proved that such a system is capable of starting automatically at a minimum temperature difference that is dependent on the system internal dissipation and physical dimensions. A symmetric three-phase Stirling engine prototype was fabricated and tested in this research to validate the developed mathematical models. The use of diaphragm pistons and nylon flexure were exercised on the fabricated system as possible easy-to-manufacture components. A reverser was introduced to modify the dynamics of a multi-phase system, mainly to lower the

corresponding gas spring hysteresis dissipation. Mathematical modeling and experimental results were discussed for the three-phase system that is equipped with a reverser.

6.1 High Power Stirling Engine Design

This dissertation provided a strong basis for the design of a high power Stirling engine that could be a potential candidate for commercial utilization in the proposed solar-thermal-electric technology. The goal is to design a Stirling engine with 2 to 3 kW output power. It is desired to keep the operating frequency below audible range. In addition, it is desired to keep the flow friction dissipation below 25 W, as that is the main loading for the displacer piston, and hence, for its actuator. The flow friction losses are strongly dependent on the flow speed, which is partly dictated by the frequency of operation. Therefore, 10 Hz appears to be an appropriate choice of operating frequency.

Output power of the engine is, to the first order, proportional to the displacer swept volume. To keep the cost low, it is proposed to use flexures to provide the bearing function for the displacer mass-spring subsystem rather than a linear motion ball bearing. Flexures are simple and very easy to manufacture. However, it appears to be a challenge to design a flexure for large piston excursions. Hence, the displacer piston excursion and diameter are chosen to be 2 cm and 13 cm, respectively. Based on these dimensions, the mean pressure of the working fluid needs to be about 75 bars to produce 2.5 kW of mechanical work. Table 6.1 tabulates the dimensions of a possible design and corresponding calculated non-ideal effects of the engine components. This design is projected to achieve thermal efficiency of 16% that is about 65% of the Carnot efficiency at 27°C and 130°C temperatures. As expected from the foregoing theoretical models and experimental efforts, the dissipative

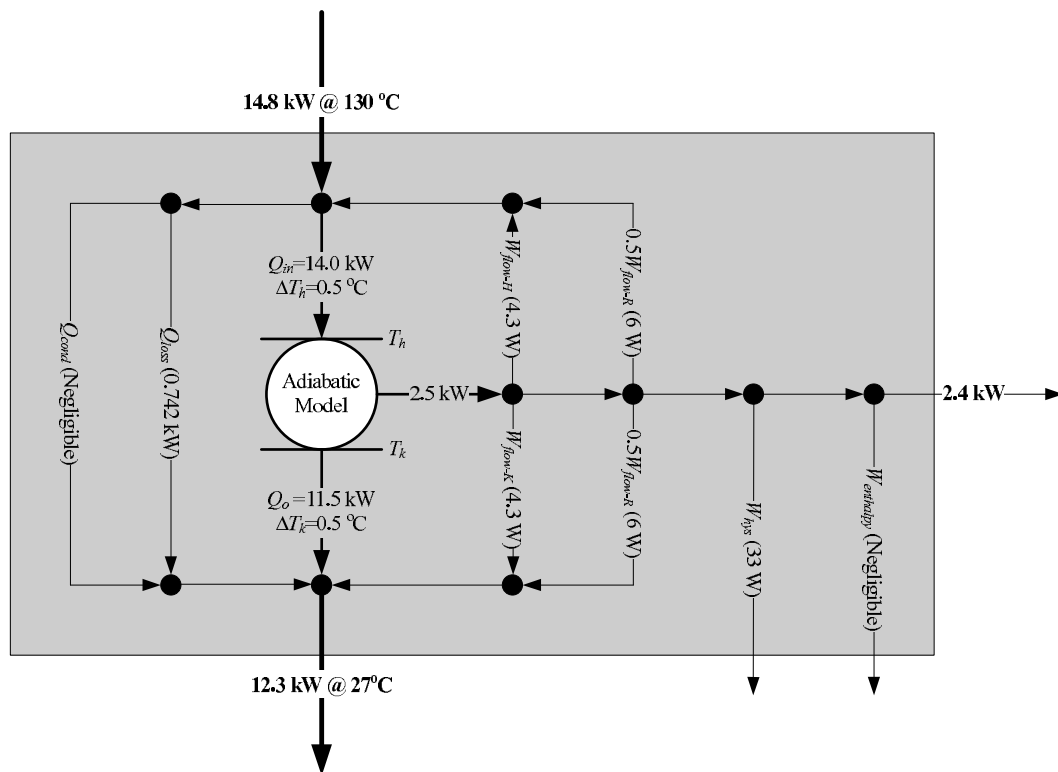


Figure 6.1: Energy balance diagram for the high-power Stirling engine. Compare to Figure 3.3.

effects of the engine are a small fraction of its output power (2.2% in this design) at higher pressures. Figure 6.1 depicts the power balance diagram of the design indicating the loss contributions of different components.

6.2 Future Work

Without a doubt, building a high-power engine and assembling a complete solar-thermal-electric system is the most important task in pursuing the proposed technology. The following paragraphs suggest some areas of research that have the potential to help improve the engine design in many respects and to provide more practical designs and low-cost components for the system.

A flexure is an appropriate and low-cost replacement for the magnetic spring within the displacer subsystem. A flexure is very stiff in the radial direction and provides the required stiffness in axial direction to set the operating frequency. It obviates the linear motion ball bearing and the shaft, eliminating the sliding friction, enthalpy and conduction losses that are an inseparable part of the current single-phase engine prototype. Therefore a research and design effort in this area will be rewarding for the next generation engine. However, careful consideration is necessary for a reliable design which guarantees 25 to 30 years of continuous operation.

In the single-phase engine prototype, the displacer piston is part of an electromagnetic system and is actuated by flowing alternating current through the windings. The magnetic circuit is an air-core system and, hence, is not very efficient. Other actuation systems could replace the current mechanism to make it simpler and more efficient. For instance, piezoelectric actuation might be an appropriate candidate for the task. Hence, further studies in this direction could lead to outstanding solutions.

This dissertation outlined a low-temperature Stirling engine which, converts low-quality thermal power into mechanical work and then into electricity. Obviously, solar-thermal-electric power generation is not the only application for such an engine. Waste heat recovery from industrial plants or even geothermal resources are examples of other areas for which a low-cost low-temperature Stirling engine could find its niche applications in generating electricity from a source of energy that otherwise would be wasted. This, by itself, could be a great research work in future.

Table 6.1: Engine design parameters.

Working fluid	Air
Temperatures	T_h : 130 °C T_k : 27 °C
Frequency	10 Hz
Pressure	75 bars
Indicated powers	Adiabatic model Input: 15 kW Output: 2.4 kW
Heater	Open area: 250 cm ² Length: 1 cm Hydraulic diameter: 0.1 mm Flow friction loss: 4.32 W Temperature drop: 0.5 °C
Cooler	Open area: 250 cm ² Length: 1 cm Hydraulic diameter: 0.1 mm Flow friction loss: 4.32 W Temperature drop: 0.5 °C
Regenerator	Open area: 600 cm ² Length: 1 cm Hydraulic diameter: 70 μ m Flow friction loss: 11.72 W Effectiveness: 98%
Displacer piston	Diameter: 12.7 cm Stroke: 4 cm
Power piston	Diameter: 15 cm Stroke: 4 cm
Gas spring hysteresis loss	33 W

Bibliography

- [1] M. A. Green, *Solar Cells*. The University of New South Wales, December 1998.
- [2] R. Pernick, C. Wilder, and C. Wilder, *The Clean Tech Revolution: The Next Big Growth and Investment Opportunity*, 1st ed. HarperCollins Publishers, June 2007.
- [3] D. Kammen, “What solar power needs now,” *Renewable Energy Access*, August 2007.
- [4] “The u.s. photovoltaic industry roadmap,” Sandia National Laboratories, Tech. Rep., May 2001.
- [5] “<http://www.solarbuzz.com>,” Worldwide web.
- [6] “<http://www.miasole.com>,” Worldwide web.
- [7] “<http://www.firstsolar.com>,” Worldwide web.
- [8] A. Tiwari, “Thin film chalcogenide photovoltaic materials,” *Thin Solid Films*, vol. 480481, p. 1, 2005.
- [9] S. Horne, “Solfocus: Redefining solar energy,” Presentation, MSE/ER C226 class: Photovoltaic Materials: Modern Technologies in the Context of a Growing Renewable Energy Market, November 2006.

-
- [10] W. T. Welford and R. Winston, *High Collection Nonimaging Optics*. Academic Press, San Diego, CA, 1989.
- [11] “<http://www.solargenix.com>,” Worldwide web.
- [12] “<http://beyondoilsolar.com>,” Worldwide web.
- [13] “Solar trough power plants,” National Renewable Energy Laboratory, Consumer Information DOE/GO-10098-469, august 2000.
- [14] “Executive summary: Assessment of parabolic trough and power tower solar technology cost and performance forecasts,” National Renewable Energy Laboratory, Tech. Rep. NREL/SR-550-35060, October 2003.
- [15] “Renewable energy technology characterization,” U.S. Department of Energy and EPRO, Tech. Rep. TR-109496, December 1997.
- [16] M. Eck and W. Steinmann, “Modelling and design of direct solar steam generating collector fields,” in *National Solar Energy Conference*, Portland, OR, July 2004.
- [17] E. Zarza and K. Hennecke, “Direct steam generation in parabolic troughs (diss) - the first year of operation of the diss test facility on the plataforma solar de almeria,” in *10th Solar PACES International Symposium on Solar Thermal Concentrating Technologies*, Sydney, Australia, March 2000.
- [18] A. Leitner, “Fuel from the sky: Solar power’s potential for western energy supply,” National Renewable Energies Laboratory, Tech. Rep. SR-550-32160, July 2002.

-
- [19] L. L. Vant-Hull and M. E. Izygon, "Guideline to central receiver heliostat field optimization," in *Advances in Solar Energy*, vol. 15. Boulder, CO: American Solar Energy Society, INc., 2003.
- [20] W. Meinecke and M. Bohn, *Solar Energy Concentrating Systems: Applications and Technologies*, B. G. M. Becker, Ed. Heidelberg, Germany: Muller Verlag, 1995.
- [21] J. C. Martín, "Solar tres," Presentation, NREL CSP Technology Workshop, March 2007.
- [22] V. L. Zimmer, C. Woo, and P. Schwartz, "Concentrated solar power for santa barbara county: Analysis of high efficiency photovoltaic and solar thermal electric," University of California, Berkeley," ERG226, Course project, December 2006.
- [23] M. Geyer, "Dish stirling activities at schlaich bergermann und partner," Presentation, NREL Concentrating Solar Power Technology Workshops, March 2007.
- [24] T. Smith, "Infinia corporation," Presentation, NREL Concentrating Solar Power Technology Workshops, March 2007.
- [25] "Solar dish stirling systems report," Presentation, NREL Concentrating Solar Power Technology Workshops, March 2007.
- [26] "<http://www.apricus.com>," Worldwide web.
- [27] "<http://www.schott.com>," Worldwide web.
- [28] J. R. Senft, *An Introduction to Low Temperature Differential Stirling Engines*, 5th ed. Moriya Press, River Falls, WI, 2002.

-
- [29] A. Der-Minassians, K. H. Aschenbach, and S. R. Sanders, "Low-cost distributed solar-thermal-electric power generation," *Proceedings of SPIE*, vol. 5185, pp. 89–98, 2004, invited Paper.
- [30] "Solel-cpc 2000, colector solar termico de concentracion," Siemens Controlmatic, Barcelona, 2000.
- [31] H. Schweiger, "The potential of solar heat for industrial processes (poship)," European Commission - Directorate General for Energy and Transport, European Union, Final NNE5-1999-0308, 2001.
- [32] S. F. N. K. Vejen and L. J. Shah, "Development of 12.5 m² solar collector panel for solar heating plants," *Solar Energy Materials and Solar Cells*, vol. 84, no. 1-4, pp. 205–223, October 2004.
- [33] I. Urieli and D. M. Berchowitz, *Stirling Cycle Engine Analysis*. Adam Hilger Ltd, Bristol, 1984.
- [34] G. T. Reader and C. Hooper, *Stirling Engines*. London; New York: E. and F.N. Spon, 1983.
- [35] T. Finkelstein and A. J. Organ, *Air Engines: The History, Science, and Reality of the Perfect Engine*. New York: ASME Press, 2001.
- [36] *Solar Electric Products Catalog: Solar Electric Modules*, 10th ed. Japan: Kyocera Solar, 2003.
- [37] J. William D. Callister, *Materials Science and Engineering: An Introduction*, 7th ed. New York: John Wiley and Sons, 2007.

- [38] R. Winston, "Solar energy for heat, light, and power," CITRIC Research Exchange Seminar, UC Berkeley, February 2007.
- [39] W. M. Kays and A. L. London, *Compact Heat Exchangers*, 3rd ed. McGraw-Hill, USA, 1984.
- [40] S. Kakac and H. Liu, *Heat Exchangers, Selection, Rating, and Thermal Design*, 2nd ed. CRC Press, Boca Raton, FL, 2002.
- [41] M. Tanaka, I. Yamashita, and F. Chisaka, "Flow and heat transfer characteristics of the stirling engine regenerator in an oscillating flow," *JSME International Journal*, vol. 33, series II, no. 2, pp. 283–289, 1990.
- [42] Z. Yuan and A. Dybbs, "Oscillating flow and heat transfer in a stirling engine regenerator," *The 28th National Heat Transfer Conference and Exhibition*, vol. 193, pp. 73–85, August 1992.
- [43] T. S. Zhao and P. Cheng, "Oscillatory pressure drops through a woven-screen packed column subjected to a cyclic flow," *Cryogenics*, vol. 36, no. 5, pp. 333–341, 1996.
- [44] S. Isshiki, A. Sakano, I. Ushiyama, and N. Isshiki, "Studies on flow resistance and heat transfer of regenerator wire meshes of stirling engine in oscillatory flow," *JSME International Journal*, vol. 40, series B, no. 2, pp. 281–289, February 1997.
- [45] I. Yamashita and K. Hamaguchi, "Effect of entrance and exit areas on the pressure drop and velocity distribution in regenerator matrix," *JSME International Journal*, vol. 42, series B, no. 3, pp. 498–505, February 1999.

-
- [46] B. Thomas, "Evaluation of 6 different correlations for the flow friction factor of stirling engine regenerators," *Proceedings of the 34th Intersociety Engineering Conference on Energy Conversion*, 1999.
- [47] B. Thomas and D. Pittman, "Update on the evaluation of different correlations for the flow friction factor and heat transfer of stirling engine regenerators," *Proceedings of the 35th Intersociety Engineering Conference on Energy Conversion*, vol. 1, pp. 76–84, 2000.
- [48] D. Gedeon and J. G. Wood, "Oscillating-flow regenerator test rig: Hardware and theory with derived correlations for screens and felts," NASA, Contractor Report 198442, February 1996.
- [49] P. J. Patt, "Design and testing of a coaxial linear magnetic spring with integral linear motor," *IEEE Trans. Magnetics*, vol. 21, no. 5, pp. 1759–1761, September 1985.
- [50] K. Qian, P. Zeng, W. Ru, and H. Yuan, "Novel magnetic spring and magnetic bearing," *IEEE Trans. Magnetics*, vol. 39, no. 1, pp. 559–561, January 2003.
- [51] W. Robertson, B. Cazzolato, and A. Zander, "A multiple array magnetic spring," *IEEE Trans. Magnetics*, vol. 41, no. 10, pp. 3826–3828, October 2005.
- [52] *McMaster-Carr Catalog 110*.
- [53] A. Der-Minassians and S. R. Sanders, "A magnetically-actuated resonant-displacer free-piston stirling machine," *5th International Energy Conversion Engineering Conference, IECEC*, June 2007.

-
- [54] S. Sastry, *Nonlinear Systems, Analysis, Stability, and Control*, 1st ed., S. W. J.E. Marsden, L. Sirovich, Ed. Springer Science+Business Media, Inc., USA, 1999.
- [55] S. D. S. Paul C. Krause, Oleg Wasynczuk, *Analysis of Electric Machinery*, iee reprint of the 1986 edition by mcgraw-hill ed., W. Perkins, Ed. IEEE Press, 1995.
- [56] A. Der-Minassians and S. R. Sanders, “Multiphase free-piston stirling engine for solar-thermal-electric power generation applications,” *5th International Energy Conversion Engineering Conference*, June 2007.

Appendix A

Second Order Dynamical System

A.1 Dry Friction

Dynamical behavior of a mass-spring system which is subject to an external force, F_{in} , and dry friction force, F_f , is expressed in form of a second order differential equation as,

$$m\ddot{x} = F_{in} - Kx - F_f\mathcal{S}(\dot{x}) \quad (\text{A.1})$$

where x is the position, m is the mass, K is the spring stiffness, and $\mathcal{S}(\cdot)$ is the sign function. The system of (A.1) can be expressed and analyzed as a piecewise linear (a.k.a. hybrid) system. However, to avoid unnecessary and complicated mathematics involved, the linear system approach is preferred here. A *ring-down* is the response of an autonomous dynamical system (i.e., $F_{in} = 0$) to a nonzero initial condition. Therefore, the ring-down of system in (A.1) is expressed as,

$$\ddot{x} = \omega_n^2 (x + \delta\mathcal{S}(\dot{x})), \quad x_0 \neq 0 \quad (\text{A.2})$$

where $\omega_n^2 = K/m$ and $\delta = F_f/K$. By choosing,

$$y_1 = \omega_n(x + \delta\mathcal{S}(\dot{x})) \quad (\text{A.3})$$

$$y_2 = \dot{x} \quad (\text{A.4})$$

the state space representation for Eq. (A.2) becomes,

$$\begin{bmatrix} \dot{y}_1 \\ \dot{y}_2 \end{bmatrix} = \begin{bmatrix} 0 & \omega_n \\ -\omega_n & 0 \end{bmatrix} \begin{bmatrix} y_1 \\ y_2 \end{bmatrix} \quad (\text{A.5})$$

which is the canonical representation of a linear oscillator that oscillates at an angular velocity of ω_n . Origin is the equilibrium of system (A.5). The equilibrium is the center-point of a circle which, depending on the initial condition, defines the system's phase portrait. Therefore, there are two equilibria to the system (A.2) which are calculated as,

$$\begin{aligned} (x_e = +\delta, \dot{x}_e = 0) \quad \dot{x} < 0 \\ (x_e = -\delta, \dot{x}_e = 0) \quad \dot{x} \geq 0 \end{aligned} \quad (\text{A.6})$$

Figure A.1 shows ring-down phase portrait and figure A.2 depicts the time-domain position of a second order mass-spring system with dry friction. Both figures indicate that the oscillation envelope is a line that can be expressed as,

$$x_{env} = m_x t + x_0 = \left(-\frac{4\delta}{T}\right)t + x_0 = \left(-\frac{2\omega_n F_f}{\pi K}\right)t + x_0 \quad (\text{A.7})$$

where m_x is the slope of the envelope to the position signal. Similarly the slope of the

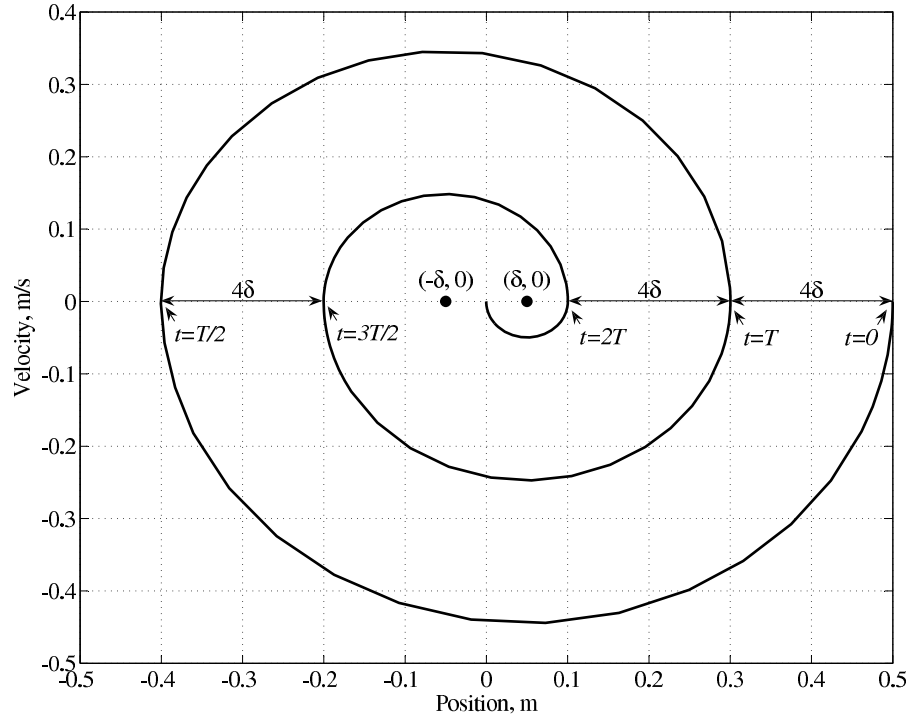


Figure A.1: Ring-down phase portrait of a second order mass-spring system with dry friction. For the simulated system, $m = 1$ kg, $K = 1$ kN/m, and $F_f = 50$ N.

envelope to the velocity signal, $m_{\dot{x}}$, and the slope of the acceleration signal envelope, $m_{\ddot{x}}$, are given by,

$$m_{\dot{x}} = \omega_n m_x = -\omega_n \frac{4\delta}{T} \quad (\text{A.8})$$

$$m_{\ddot{x}} = \omega_n^2 m_x = -\omega_n^2 \frac{4\delta}{T} \quad (\text{A.9})$$

Therefore, observation of a linear envelope in the position, velocity, or acceleration signal during a ring-down assessment test indicates existence of dry friction. Magnitude of the friction force is estimated based on the slope of this envelope given that either the spring stiffness or the mass of the ringing system is known. Consequently, the power loss associated with the estimated friction force for a certain frequency and displacement, can be calculated by the corresponding expression given in Table 5.1.

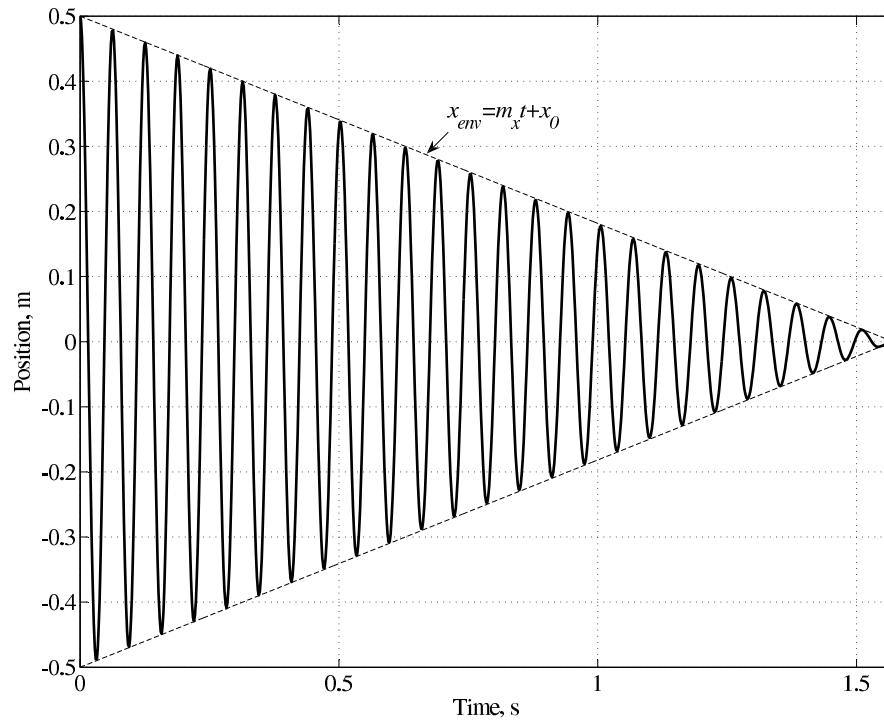


Figure A.2: Time-domain position for the ring-down of a second order mass-spring system with dry friction. For the simulated system, $m = 1$ kg, $K = 10$ kN/m, and $F_f = 50$ N.

A.2 Viscous Friction

Figure A.3 depicts the time-domain position of a second order mass-spring system with viscous friction. The oscillation envelope expressed as,

$$x_{env} = x_0 e^{-\frac{1}{2} \frac{D}{m} t} \quad (\text{A.10})$$

where D is the friction factor and m is the oscillating mass. Therefore, observation of an exponential envelope in the position, velocity, or acceleration signal during a ring-down assessment test indicates existence of viscous friction. Friction factor, D , is estimated based on the following calculation given that either the spring stiffness, K , or the mass of the

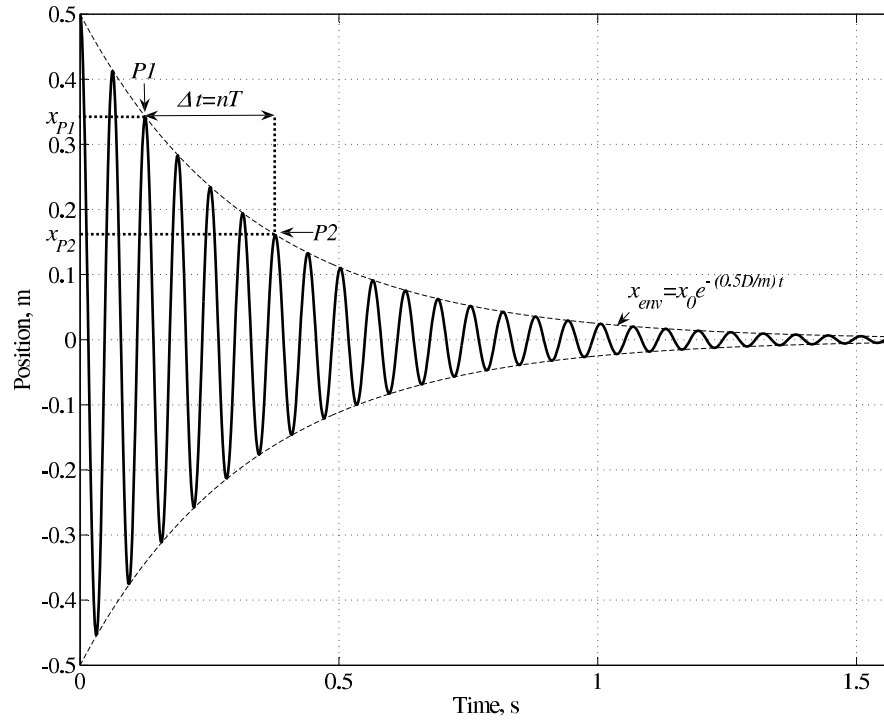


Figure A.3: Time-domain position for the ring-down of a second order mass-spring system with viscous friction. For the simulated system, $m = 1$ kg, $K = 10$ kN/m, and $D = 6$ Ns/m.

ringing system, m , is known.

$$\frac{D}{m} = \frac{2}{\Delta t} \ln \left(\frac{x_{P1}}{x_{P2}} \right) \quad (\text{A.11})$$

where x_{P1} and x_{P2} correspond to the position (also velocity or acceleration) of the ringing mass at two arbitrary peaks, and Δt is the time delay between the peaks which, of course, is a multiple of ringing period, T . These parameters are shown on figure A.3 as well. Needless to mention that,

$$\omega_n = \frac{2\pi}{T} = \sqrt{\frac{K}{m}} \quad (\text{A.12})$$

Consequently, the power loss associated with the estimated viscous friction for a certain frequency and displacement, can be calculated by the corresponding expression given in

Table 5.1. Lastly, the quality factor, Q , of this system is calculated as,

$$Q = \frac{\omega_n}{D/m} \quad (\text{A.13})$$

Appendix B

Gas Spring Stiffness

Consider a thermally insulated gas container that is equipped with a sealed moving piston. Without loss of generality, we can assume that the internal and external pressures of the container are initially equal and, hence, the piston is at resting position. The thermal insulation provides an adiabatic boundary condition for the contained gas. Therefore, at any given temperature, the gas pressure, p , and its volume, V , will follow a trajectory defined by

$$pV^\gamma = C \tag{B.1}$$

where $\gamma = c_p/c_V$ is the ratio of the gas specific heat at constant pressure to the gas specific heat at constant volume and C represents a constant value. A small force, dF , will cause a small displacement, dx , and the gas pressure and volume will change according to the following expressions

$$dV = -A_P dx \tag{B.2}$$

$$dp = \frac{dF}{A_P} \tag{B.3}$$

where A_P is the cross sectional area of the piston.

By differentiating (B.1) and appropriate substitutions from (B.2) and (B.3) we have,

$$V^\gamma \frac{dF}{A_P} - \gamma p A_P V^{\gamma-1} dx = 0 \quad (\text{B.4})$$

which yields to the gas spring stiffness, K_G , as derived below,

$$K_G = \frac{dF}{dx} = \frac{\gamma p A_P^2}{V} \quad (\text{B.5})$$

Similarly, if gas compression is considered an isothermal process, we have,

$$pV = C \quad (\text{B.6})$$

which yields to the gas spring stiffness, K_G , as below,

$$K_G = \frac{p A_P^2}{V} \quad (\text{B.7})$$

Appendix C

Symmetric Six-Phase Stirling System

For a symmetric six-phase system, according to the general formulation in Eq. (5.10), the stiffness matrix \mathbf{K} of the linearization is,

$$\mathbf{K} = \begin{bmatrix} \frac{K_P}{m_P} + (b + c) & -b & 0 & 0 & 0 & -c \\ -c & \frac{K_P}{m_P} + (b + c) & -b & 0 & 0 & 0 \\ 0 & -c & \frac{K_P}{m_P} + (b + c) & -b & 0 & 0 \\ 0 & 0 & -c & \frac{K_P}{m_P} + (b + c) & -b & 0 \\ 0 & 0 & 0 & -c & \frac{K_P}{m_P} + (b + c) & -b \\ -b & 0 & 0 & 0 & -c & \frac{K_P}{m_P} + (b + c) \end{bmatrix} \quad (\text{C.1})$$

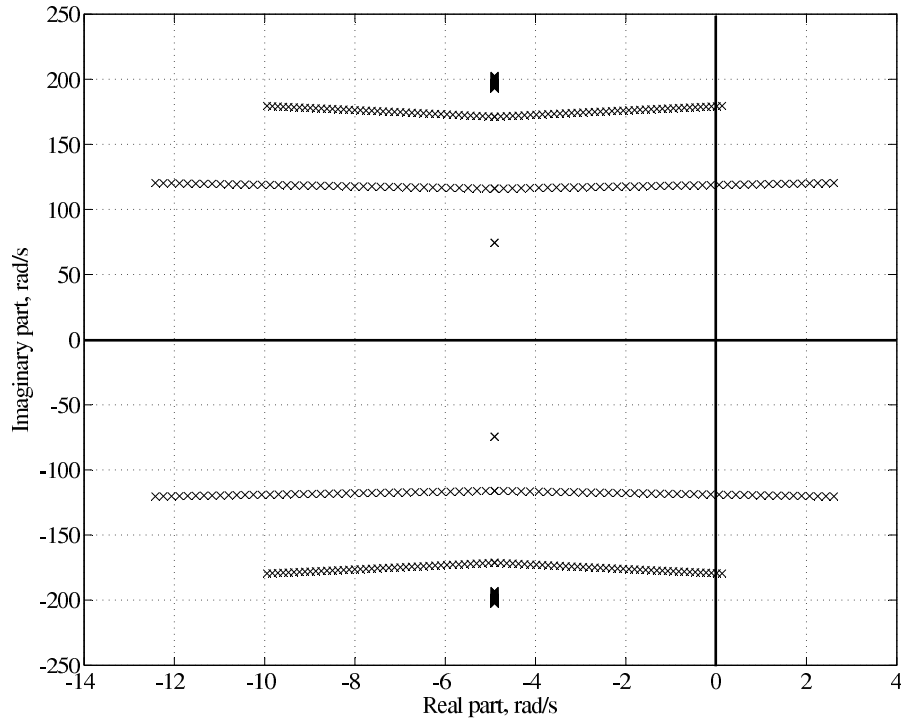


Figure C.1: Progression of the eigenvalues of six-phase Stirling engine toward the unstable region as the hot side temperature increases. At $T_h = 79$ °C the system becomes self-starting.

And similar to the symmetric three-phase case, a linear transformation $\mathbf{x} = \mathbf{T}\mathbf{z}$ where

$$\mathbf{T} = \begin{bmatrix} \cos(0) & \sin(0) & \cos(0) & \sin(0) & \cos(0) & \cos(0) \\ \cos(0) & \sin(\frac{\pi}{3}) & \cos(\frac{\pi}{3}) & \sin(\frac{2\pi}{3}) & \cos(\frac{2\pi}{3}) & \cos(\pi) \\ \cos(0) & \sin(\frac{2\pi}{3}) & \cos(\frac{2\pi}{3}) & \sin(\frac{4\pi}{3}) & \cos(\frac{4\pi}{3}) & \cos(2\pi) \\ \cos(0) & \sin(\frac{3\pi}{3}) & \cos(\frac{3\pi}{3}) & \sin(\frac{6\pi}{3}) & \cos(\frac{6\pi}{3}) & \cos(3\pi) \\ \cos(0) & \sin(\frac{4\pi}{3}) & \cos(\frac{4\pi}{3}) & \sin(\frac{8\pi}{3}) & \cos(\frac{8\pi}{3}) & \cos(4\pi) \\ \cos(0) & \sin(\frac{5\pi}{3}) & \cos(\frac{5\pi}{3}) & \sin(\frac{10\pi}{3}) & \cos(\frac{10\pi}{3}) & \cos(5\pi) \end{bmatrix} \quad (\text{C.2})$$

transforms matrix \mathbf{K} into a new state matrix $\tilde{\mathbf{K}}$ as below,

$$\tilde{\mathbf{K}} = \begin{bmatrix} \frac{K_P}{m_P} & 0 & 0 & 0 & 0 & 0 \\ 0 & \frac{K_P}{m_P} + \frac{1}{2}(b+c) & -\frac{\sqrt{3}}{2}(b-c) & 0 & 0 & 0 \\ 0 & \frac{\sqrt{3}}{2}(b-c) & \frac{K_P}{m_P} + \frac{1}{2}(b+c) & 0 & 0 & 0 \\ 0 & 0 & 0 & \frac{K_P}{m_P} + \frac{3}{2}(b+c) & -\frac{\sqrt{3}}{2}(b-c) & 0 \\ 0 & 0 & 0 & \frac{\sqrt{3}}{2}(b-c) & \frac{K_P}{m_P} + \frac{3}{2}(b+c) & 0 \\ 0 & 0 & 0 & 0 & 0 & \frac{K_P}{m_P} + 2(b+c) \end{bmatrix} \quad (\text{C.3})$$

which simply reveals the following six eigenvalues for the six-phase stiffness matrix \mathbf{K} ,

$$\mu_1 = \frac{K_P}{m_P} \quad (\text{C.4})$$

$$\mu_{2,3} = \left(\frac{K_P}{m_P} + \frac{3}{2}(b+c) \right) \pm j \frac{\sqrt{3}}{2}(b-c) \quad (\text{C.5})$$

$$\mu_4 = \frac{K_P}{m_P} + 2(b+c) \quad (\text{C.6})$$

$$\mu_{5,6} = \left(\frac{K_P}{m_P} + \frac{1}{2}(b+c) \right) \pm j \frac{\sqrt{3}}{2}(b-c) \quad (\text{C.7})$$

Note that a six-phase system includes all the modes of a three-phase system (i.e., μ_1 , μ_2 , and μ_3). In addition, μ_4 represents the “pure compression” mode with a frequency that is proportional to the root of the average temperature of compression and expansion spaces. As the average temperature rises, the internal pressure of the engine and, hence, the gas spring stiffness increases, which causes a higher resonant frequency. Remember that μ_1 represents the pure displacement mode which is independent of gas spring stiffness and, therefore, remains unchanged with temperature variations. The remaining two eigenvalues

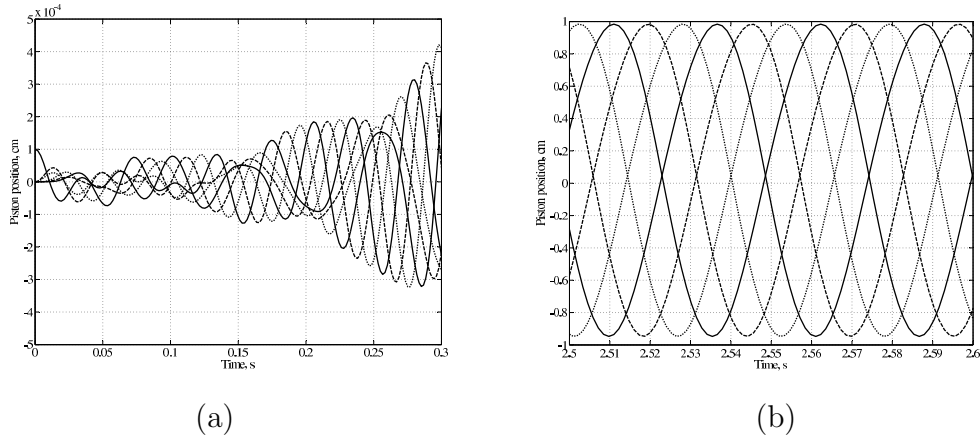


Figure C.2: Simulated piston positions of the six-phase system. (a) Startup (b) Steady state.

correspond to the “forward” and “backward” six-phase operation of the system.

Departing from thermal equilibrium, as T_h increases, eigenvalues $\lambda_{5,6}$ (associated with eigenvalues $\mu_{5,6}$) hit the $j\omega$ -axis first. Therefore, the relationship between the damping factor and start-up temperature becomes,

$$\frac{1}{T_h} = \frac{1}{T_k} - \frac{d}{\alpha} \sqrt{\frac{4}{3} m_P (K_P + K_G)} \quad (\text{C.8})$$

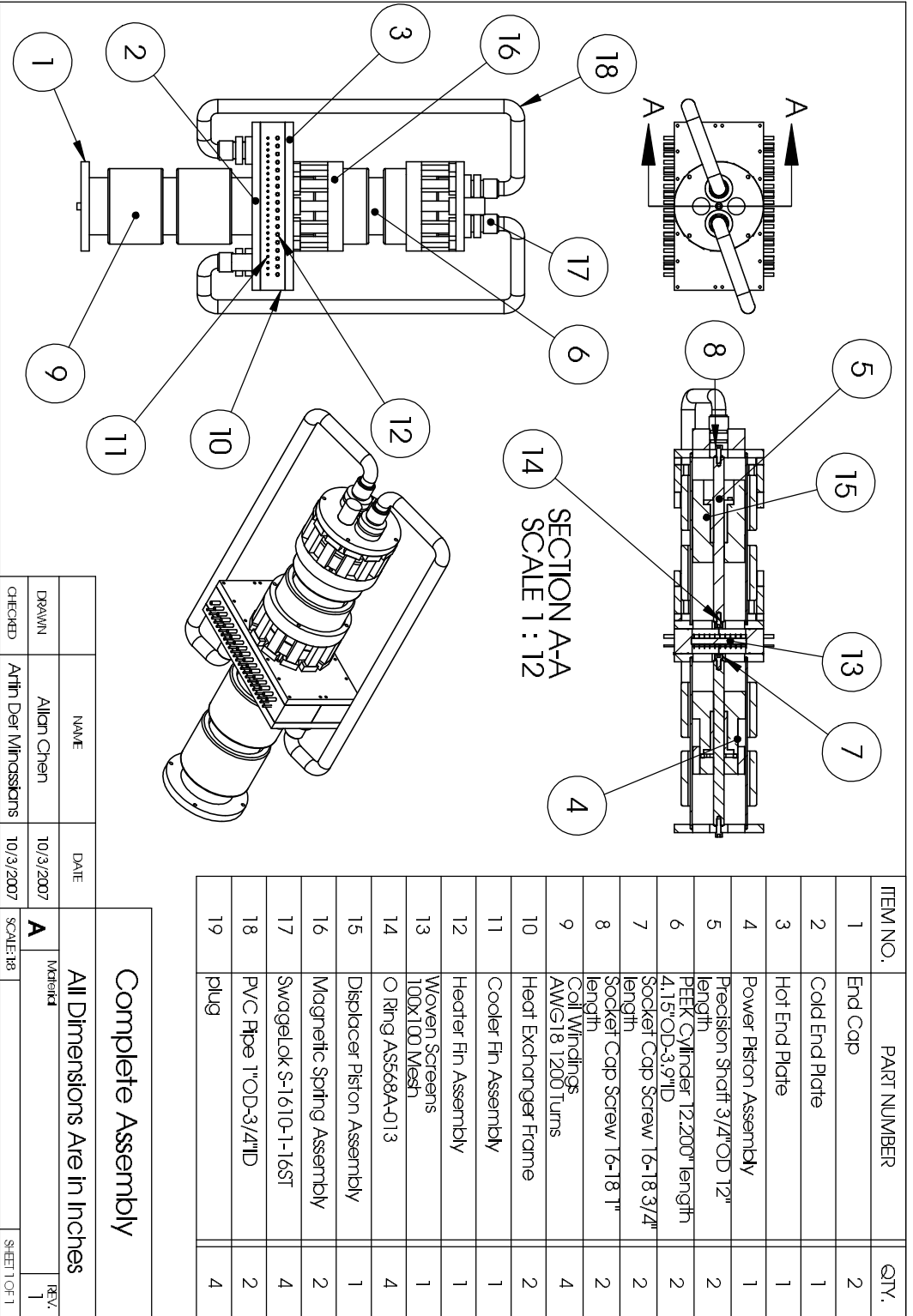
which indicates that the resonant frequency of the system is set by sum of the stiffnesses K_P and K_G .

The eigenvalue loci of the three-phase Stirling engine system with reverser is shown in Figure C.1 and the simulation result of the same system is depicted in Figure C.2.

Appendix D

Technical Drawings for the Single-Phase Stirling Engine Prototype

This appendix contains the engineering drawings to make the single-phase Stirling engine prototype. The parts and assemblies are named intuitively to reflect their function within the engine. All assembly drawings contain a BOM to reference the corresponding parts. The drawings are ordered first by hierarchy: Assembly drawings precede part drawings. The parts drawings are ordered by alphanumeric order.



ITEM NO.	PART NUMBER	QTY.
1	End Cap	2
2	Cold End Plate	1
3	Hot End Plate	1
4	Power Piston Assembly	1
5	Precision Shaft 3/4"OD 12" length	2
6	PEEK Cylinder 12.200" length 4.15"OD-3.9"ID	2
7	Socket Cap Screw 16-18 3/4" length	2
8	Socket Cap Screw 16-18 1" length	2
9	Coil Windings AWG18 1200 Turns	4
10	Heat Exchanger Frame	2
11	Cooler Fin Assembly	1
12	Heater Fin Assembly	1
13	Woven Screens 100X100 Mesh	1
14	O Ring ASS668A-013	4
15	Displacer Piston Assembly	1
16	Magnetic Spring Assembly	2
17	Swagelok S-1610-1-16ST	4
18	PVC Pipe 1"OD-3/4"ID	2
19	plug	4

Complete Assembly

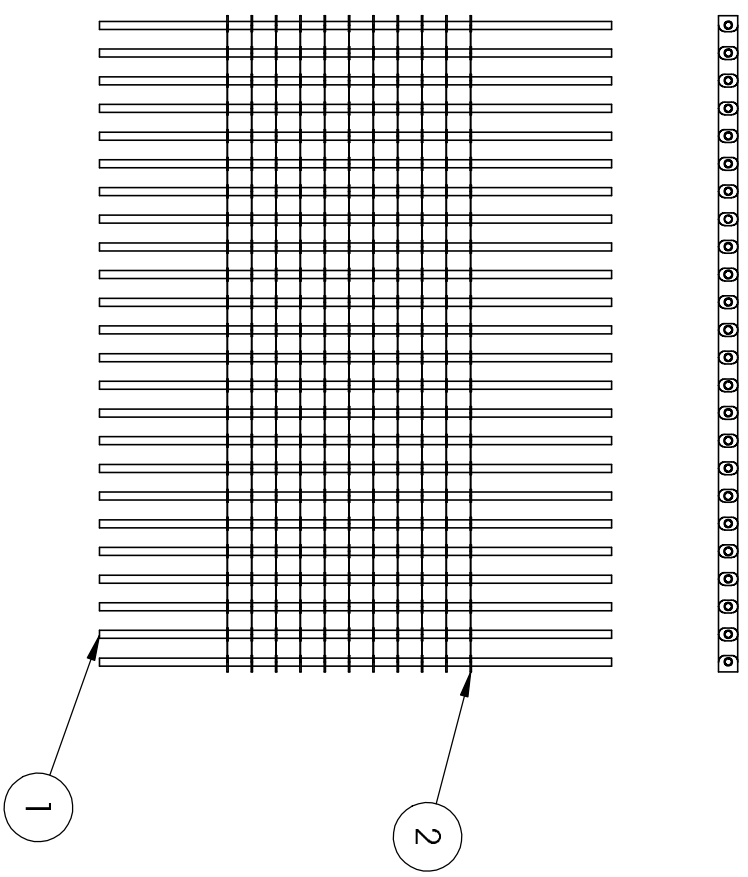
All Dimensions Are in Inches

NAME	DATE	REV.
Allan Chen	10/3/2007	1
Artin Der Minassians	10/3/2007	

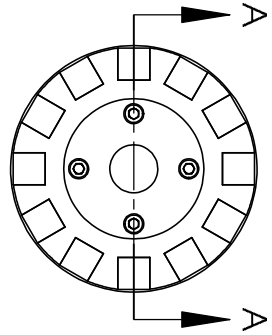
CHECKED

SCALE:	SHEET	OF
A	18	1

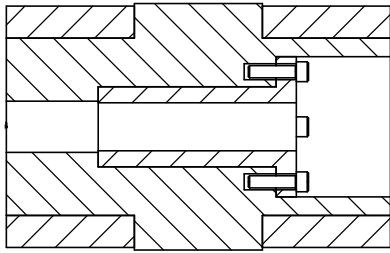
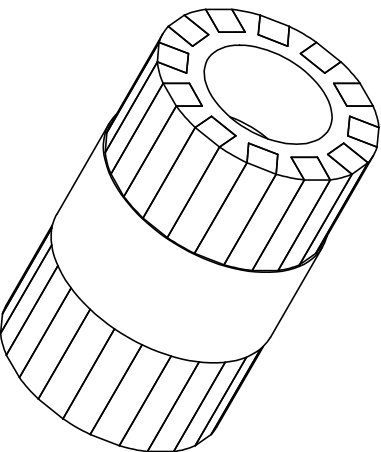
ITEM NO.	PART NUMBER	QTY.
1	Cooler Tube	24
2	Cooler Fin	195



Cooler Fin Assembly	
All Dimensions Are in Inches	
NAME	DATE
Allan Chen	10/3/2007
DRAWN	SCALE: A
Artin Der Minassians	10/3/2007
CHECKED	SCALE: 1:3
	SHEET 1 OF 1



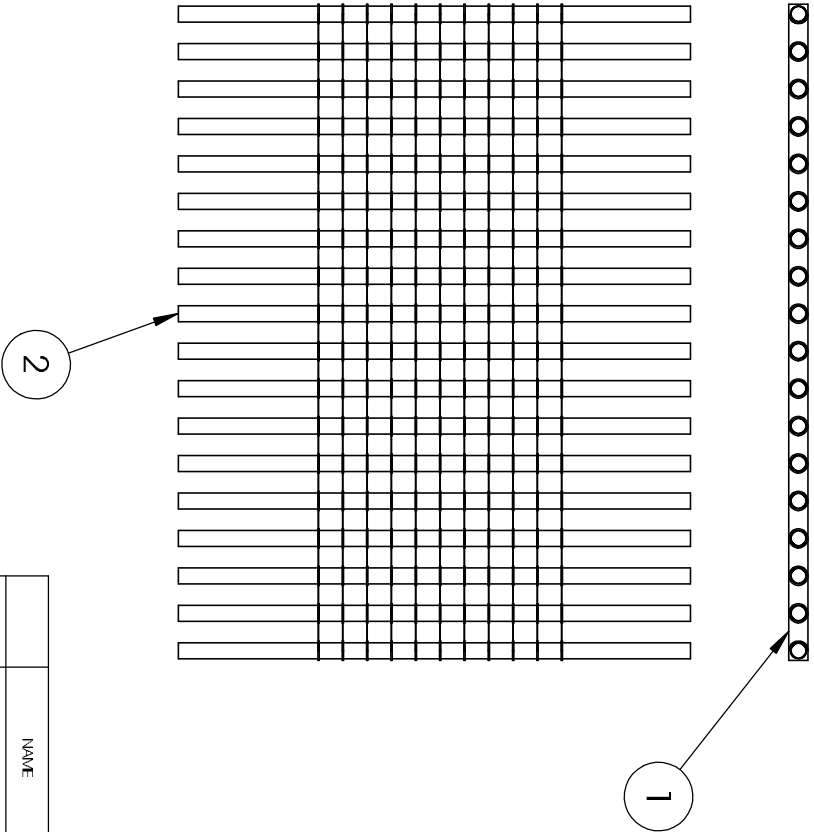
ITEM NO.	PART NUMBER	QTY.
1	Displacer Piston Core	1
2	Displacer Piston Sm-Co Magnet	24
3	Linear Ball Bearing (Nippon Bearing - SWSF12)	1
4	Socket Cap Screw HX-SHCS 0.19-32X0.75X0.75-N	4



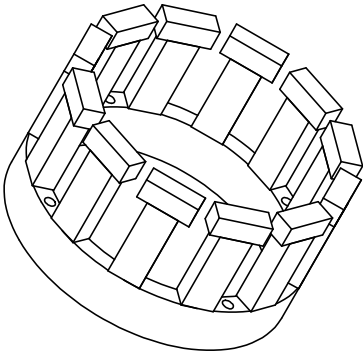
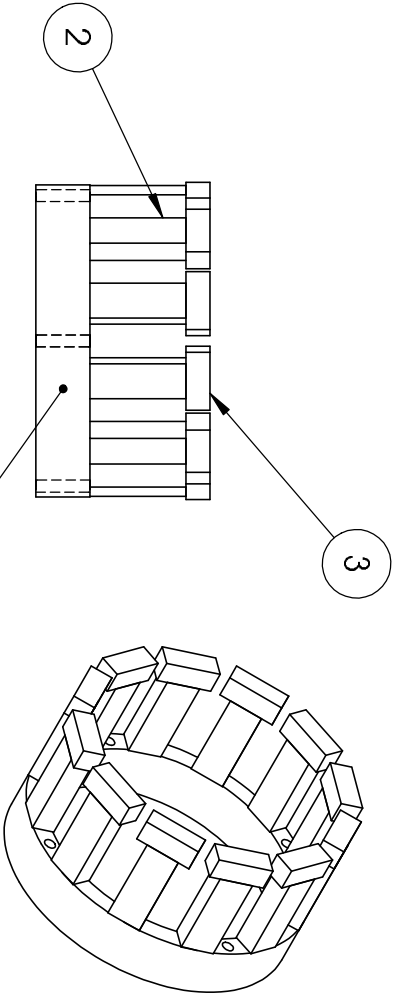
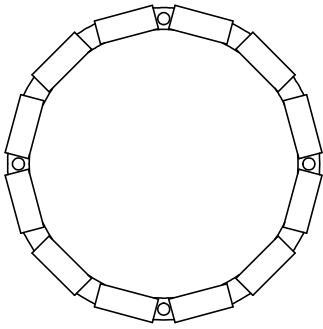
SECTION A-A

NAME	DATE	Displacer Piston Assembly	
Alien Chen	10/3/2007	All Dimensions Are in Inches	
Artin Der Minassians	10/3/2007	SCALE:1:1	REV. 1
CHECKED			SHEET 1 OF 1

ITEM NO.	PART NUMBER	QTY.
1	Heater Fin	11
2	Heater Tube	195



Heater Fin Assembly			
All Dimensions Are in Inches			
	NAME	DATE	SCALE:1:3
DRAWN	Allen Chen	10/3/2007	A
CHECKED	Artin Der Minassians	10/3/2007	REV: 1
			SHEET 1 OF 1



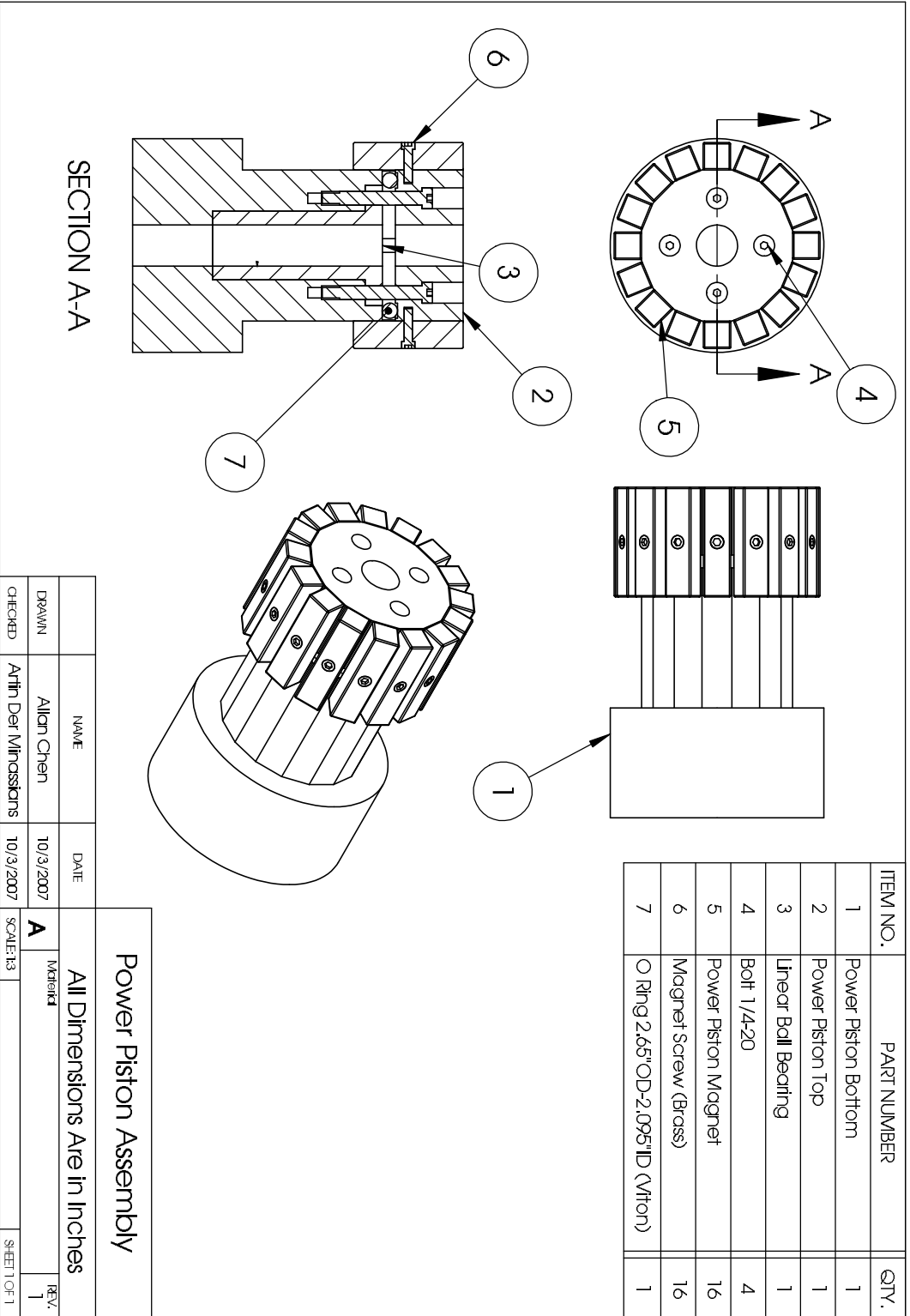
ITEM NO.	PART NUMBER	QTY.
1	Powder Iron Ring	1
2	Spring Magnet Vertical	12
3	Spring Magnet Horizontal	12

Magnetic Spring Assembly

All Dimensions Are in Inches

	NAME	DATE	SCALE:1:1	REV.
DRAWN	Alicia Chen	10/2/2007	A	1
CHECKED	Artin Der Minassians	10/2/2007		

SHEET 1 OF 1



SECTION A-A

Power Piston Assembly

All Dimensions Are in Inches

NAME	DATE	SCALE	SHEET
Alien Chen	10/3/2007	A	1
Artin Der Minassians	10/3/2007		1

DRAWN

CHECKED

REV.

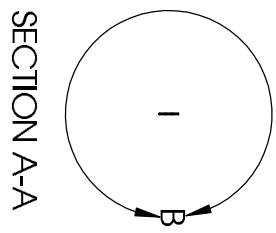
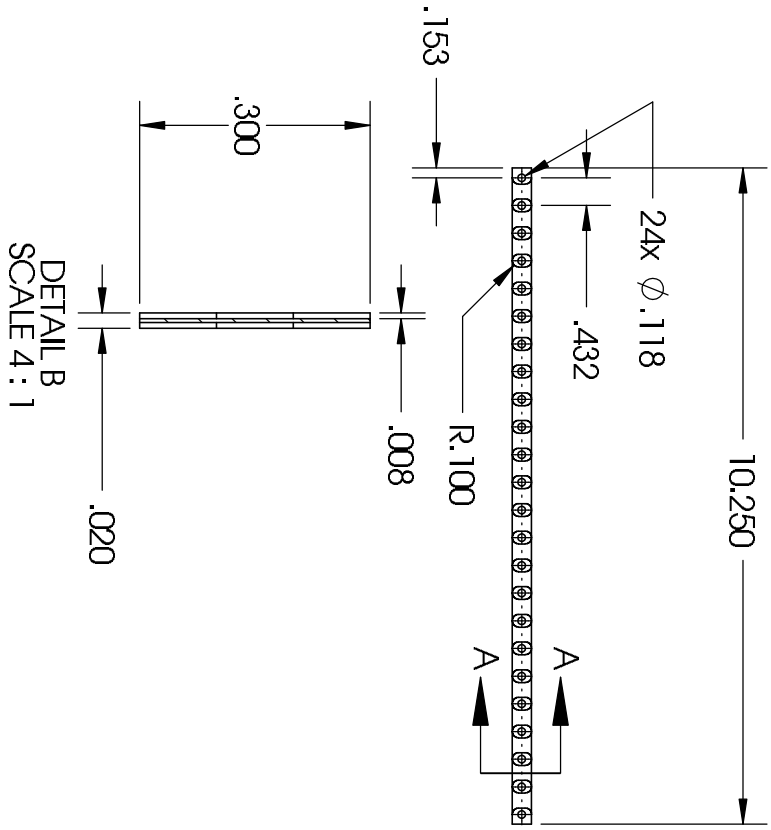
1

1

1

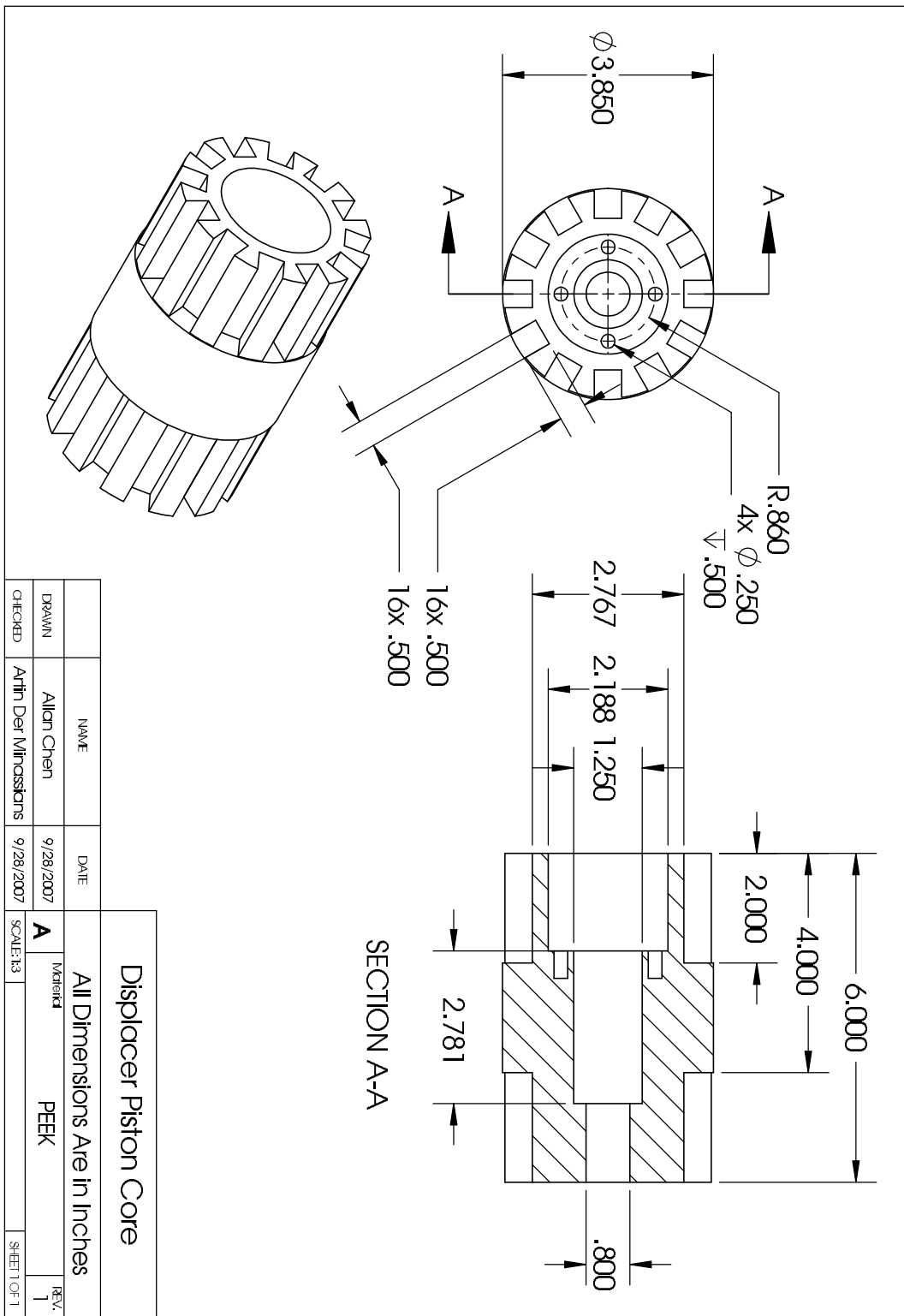
1

1

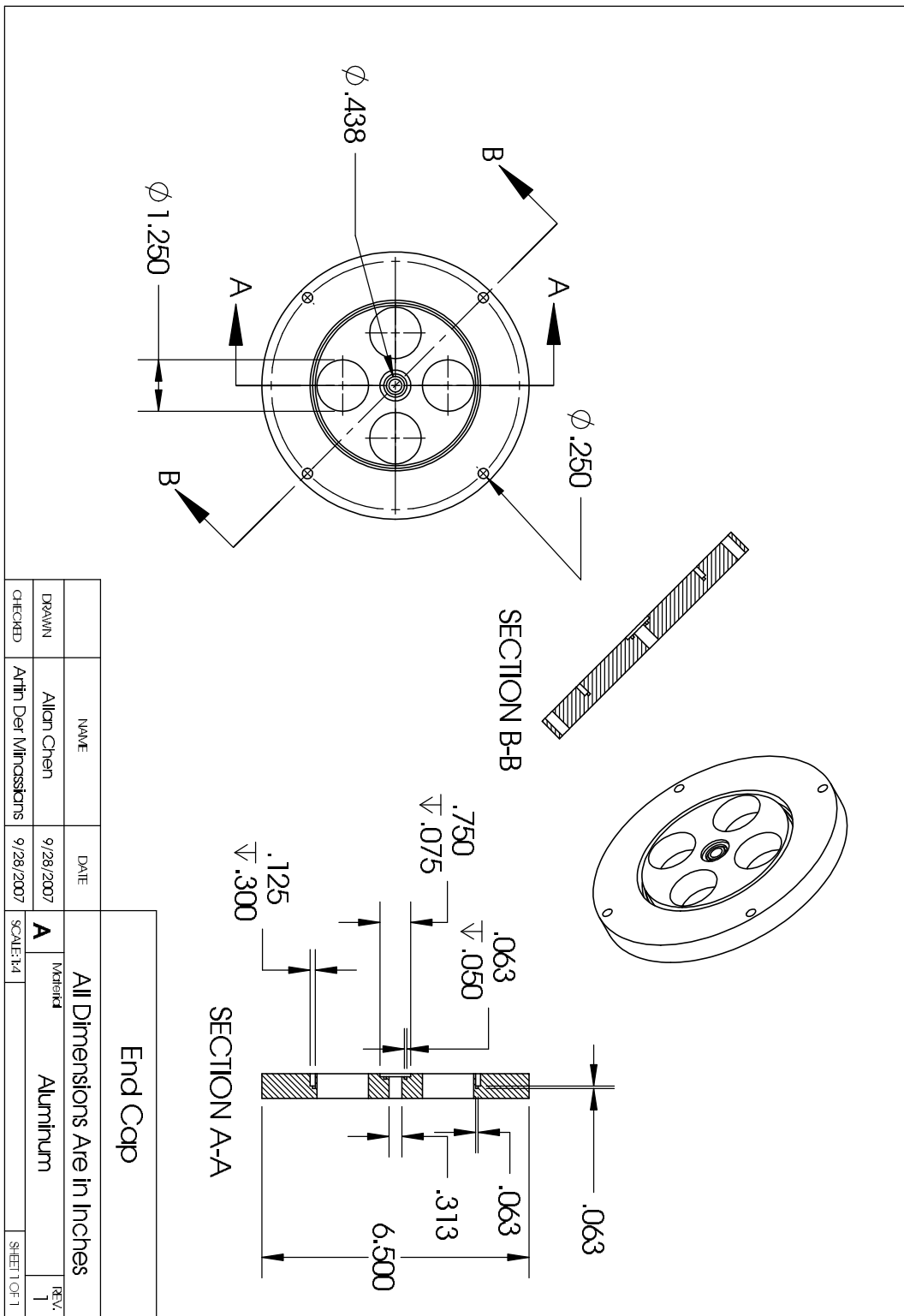


Cooler Fin

All Dimensions Are in Inches	
NAME	Alien Chen
DATE	10/3/2007
DRAWN	Artin Der Minassians
CHECKED	10/3/2007
SCALE: 13	SCALE: 13
REV.	1
SHEET	1 OF 1



<p style="text-align: center;">Displacer Piston Core</p> <p style="text-align: center;">All Dimensions Are in Inches</p>		NAME	DATE	<p style="text-align: center;">Material</p> <p style="text-align: center;">PEEK</p>	<p style="text-align: center;">REV.</p> <p style="text-align: center;">1</p>
		DRAWN	9/28/2007		
CHECKED	Artin Der Minassians	9/28/2007	SCALE: 1:1	SHEET 1 OF 1	

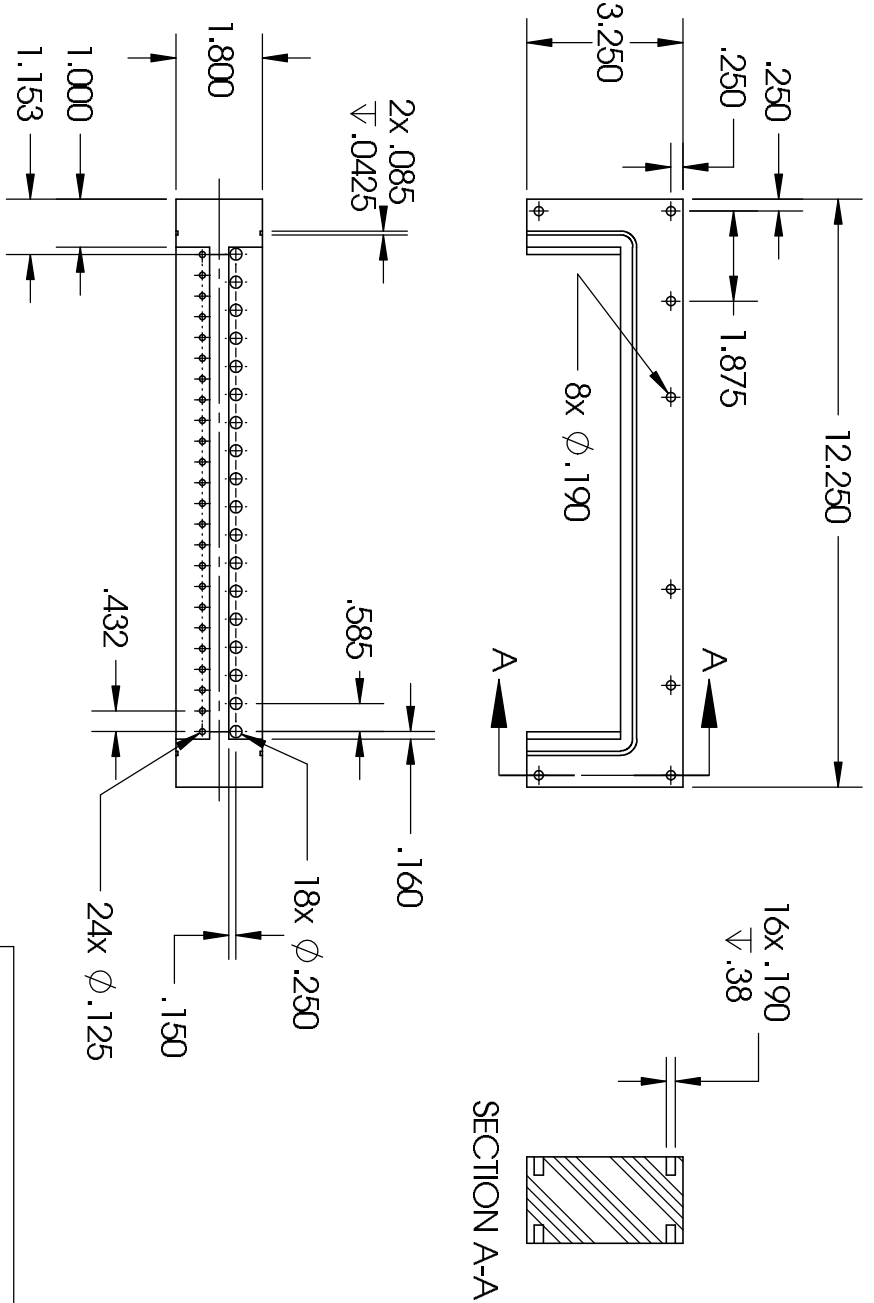


All Dimensions Are in Inches		NAME	DATE	SCALE: 1:1	SHEET 1 OF 1
		DRAWN	9/28/2007		
CHECKED	Artin Der Minassians	9/28/2007			

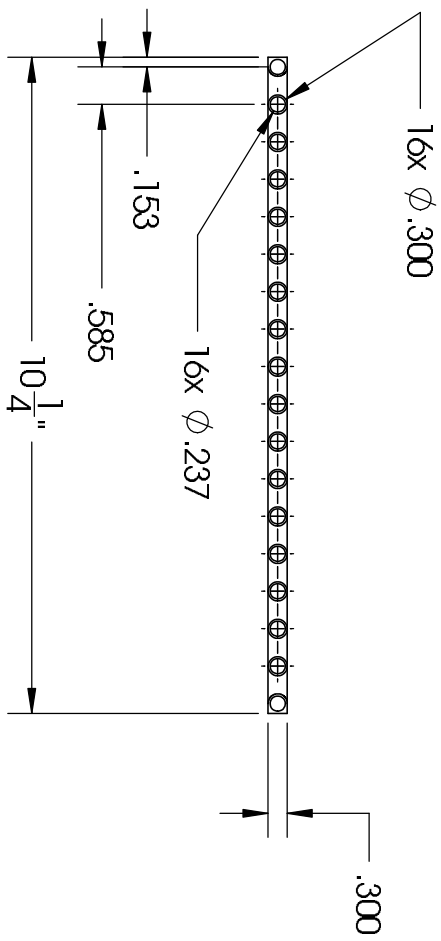
End Cap

Material: Aluminum

REV: 1



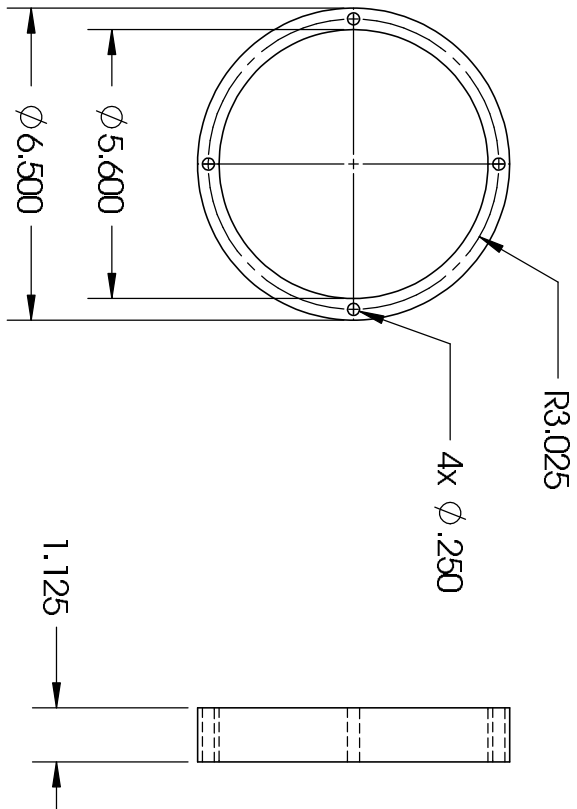
Heat Exchangers Frame		All Dimensions Are in Inches	
NAME	Alien Chen	DATE	10/2/2007
DRAWN	Artin Der Minostians	CHECKED	Artin Der Minostians
SCALE: 1:1	PTFE	REV:	1
SHEET 1 OF 1			



0.02 Overall thickness (right view dimensions are the same as Cooler Fin)

		NAME		DATE		All Dimensions Are in Inches	
DRAWN		Allan Chen		10/3/2007		Material	
CHECKED		Artin Der Minassians		10/3/2007		Copper	
		SCALE: 1:1		REV.		1	
		SHEET 1 OF 1					

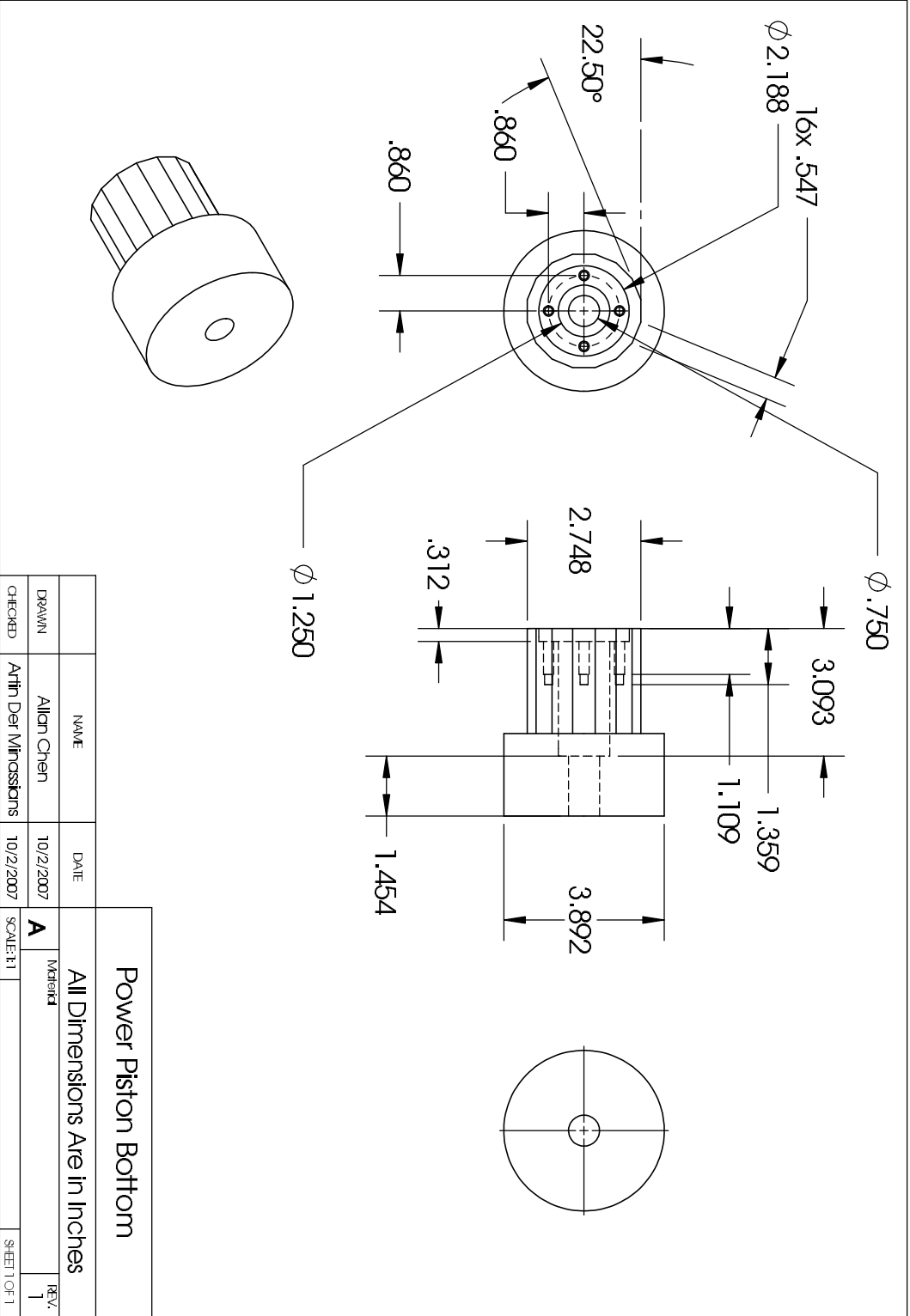
Heater Fin



Micrometals Inc.
-52 Material

Powder Iron Ring

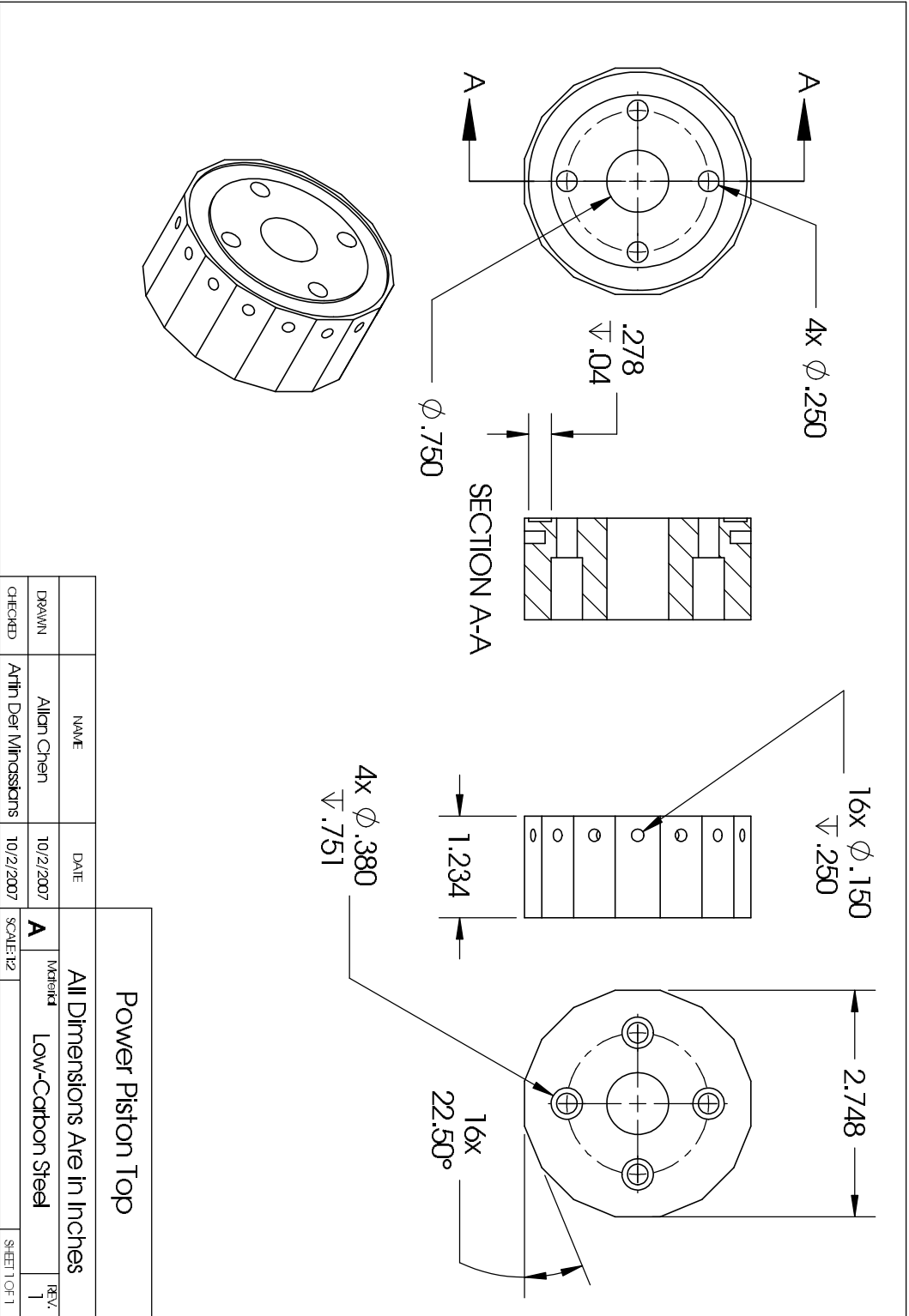
All Dimensions Are in Inches	
NAME	Allan Chen
DATE	10/2/2007
DRAWN	Artin Der Minassians
CHECKED	Artin Der Minassians
SCALE:1:1	REV: 1
SHEET 1 OF 1	



Power Piston Bottom

All Dimensions Are in Inches

NAME	DATE	Modified	
Artin Der Minassians	10/2/2007	A	REV: 1
Artin Der Minassians	10/2/2007	SCALE: 1:1	SHEET 1 OF 1



Power Piston Top

All Dimensions Are in Inches

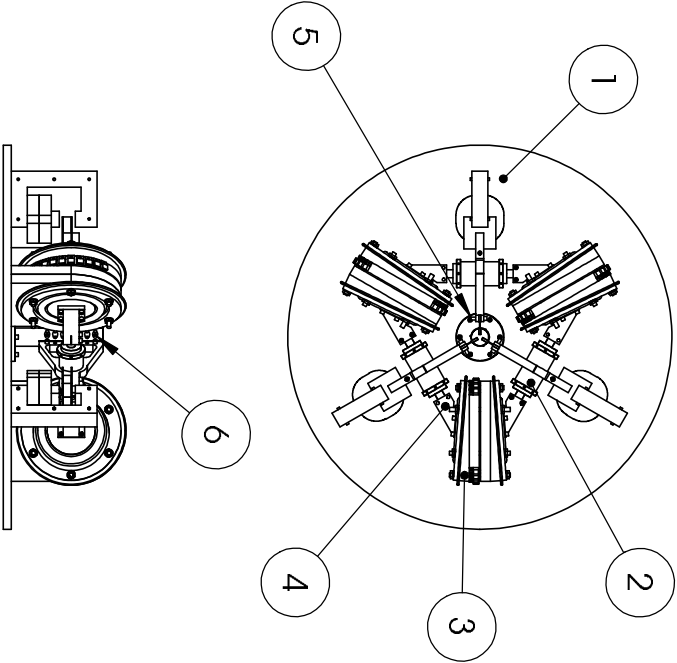
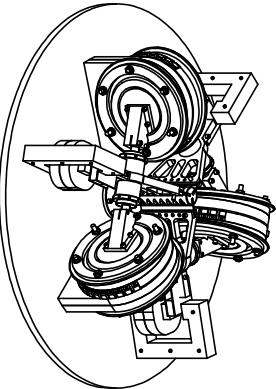
NAME	DATE	All Dimensions Are in Inches	
Alien Chen	10/2/2007	Material	REV.
Artin Der Minassians	10/2/2007	Low-Carbon Steel	1
CHECKED		SCALE: 1:2	SHEET 1 OF 1

Appendix E

Technical Drawings for the Three-Phase Stirling Engine Prototype

This appendix contains the engineering drawings to make the three-phase Stirling engine prototype. The parts and assemblies are named intuitively to reflect their function within the engine. All assembly drawings contain a BOM to reference the corresponding parts. The drawings are ordered first by hierarchy: Assembly drawings precede part drawings. The parts drawings are ordered by alphanumeric order.

ITEM NO.	PART NUMBER	QTY.
1	Plate Assembly	1
2	Arm Assembly	3
3	Engine Assembly	3
4	Shoe	6
5	Socket Cap Screw 10-32 Threaded (long)	7
6	Socket Cap Screw 10-32 Threaded (short)	30

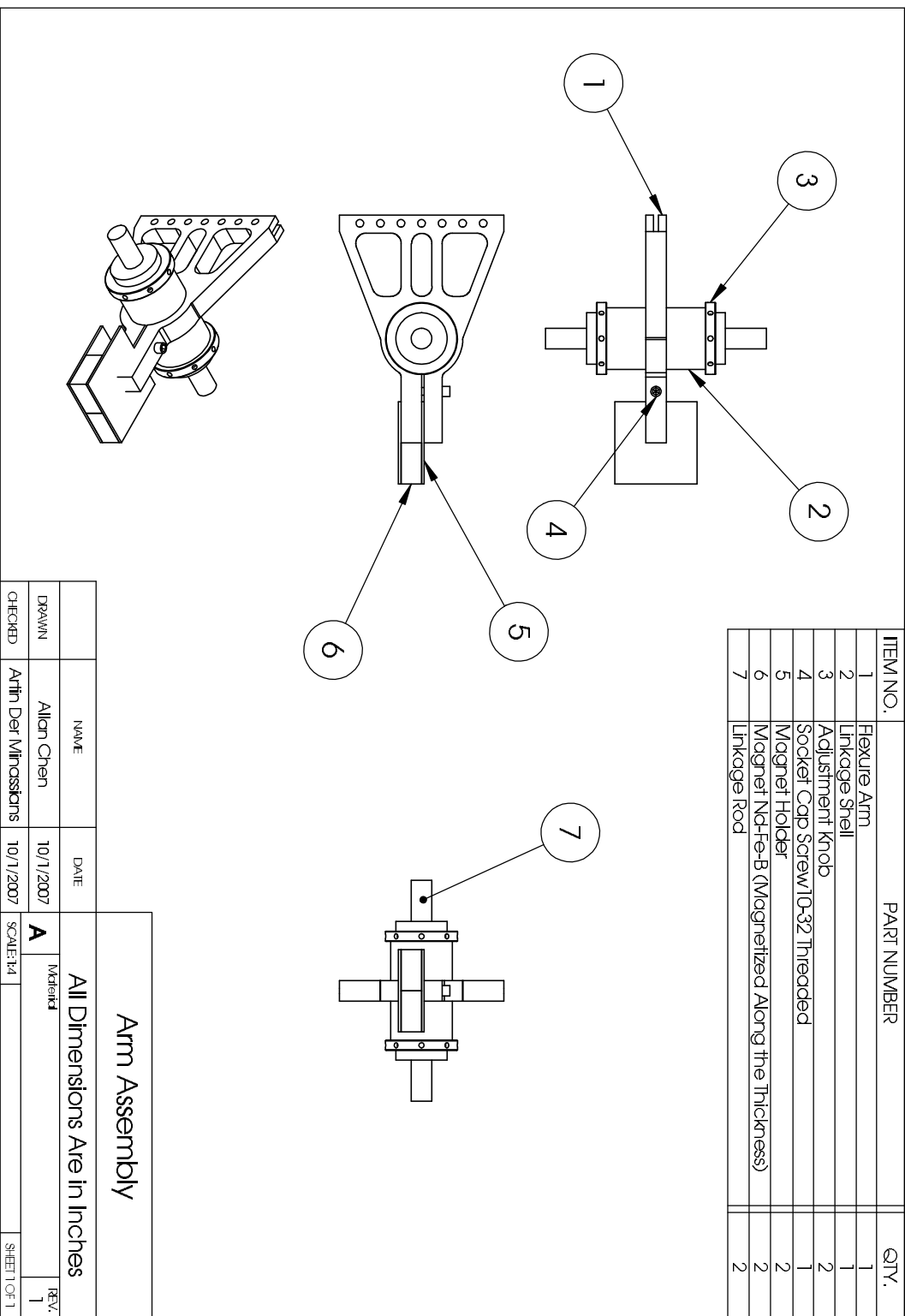



Three Phase Engine Assembly

All Dimensions Are in Inches

NAME	DATE	SCALE	SHEET
Alian Chen	10/1/2007	A	1
Artin Der Missions	10/1/2007	SCALE: 1/2	SHEET 1 OF 1

DRAWN	CHECKED
-------	---------



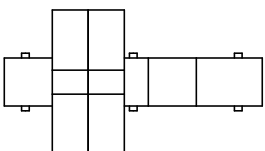
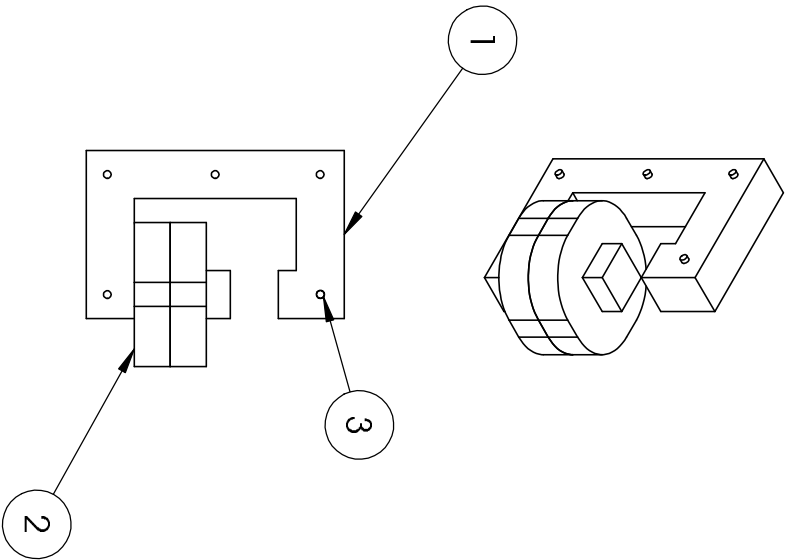
Arm Assembly

All Dimensions Are in Inches

NAME	DATE	SCALE:1:1	REV.
Allan Chen	10/11/2007	A	1
Checked: Artin Der Missions	10/11/2007		

SHEET 1 OF 1

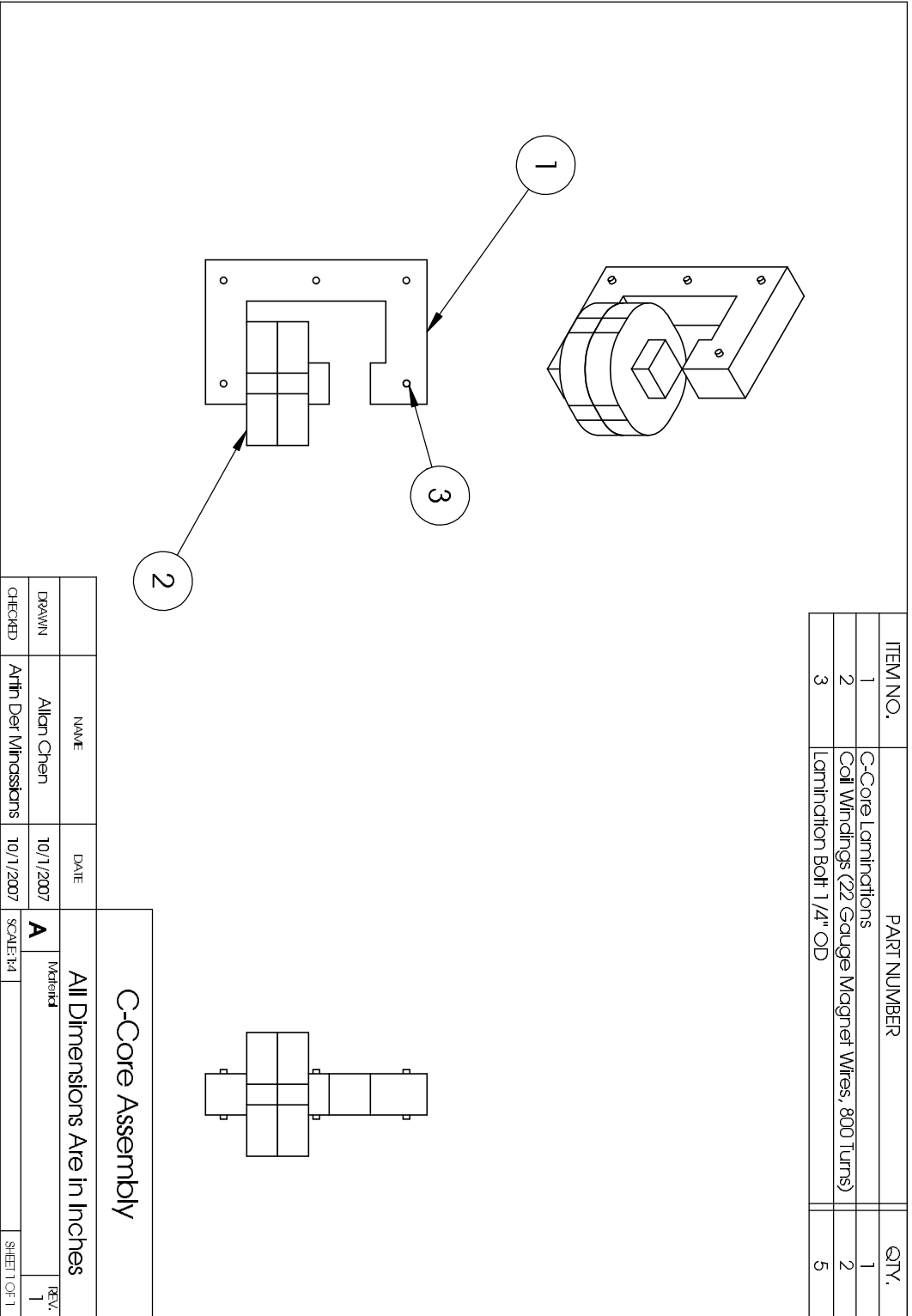
ITEM NO.	PART NUMBER	QTY.
1	C-Core Laminations	1
2	Coil Windings (22 Gauge Magnet Wires, 800 Turns)	2
3	Lamination Bolt 1/4" OD	5

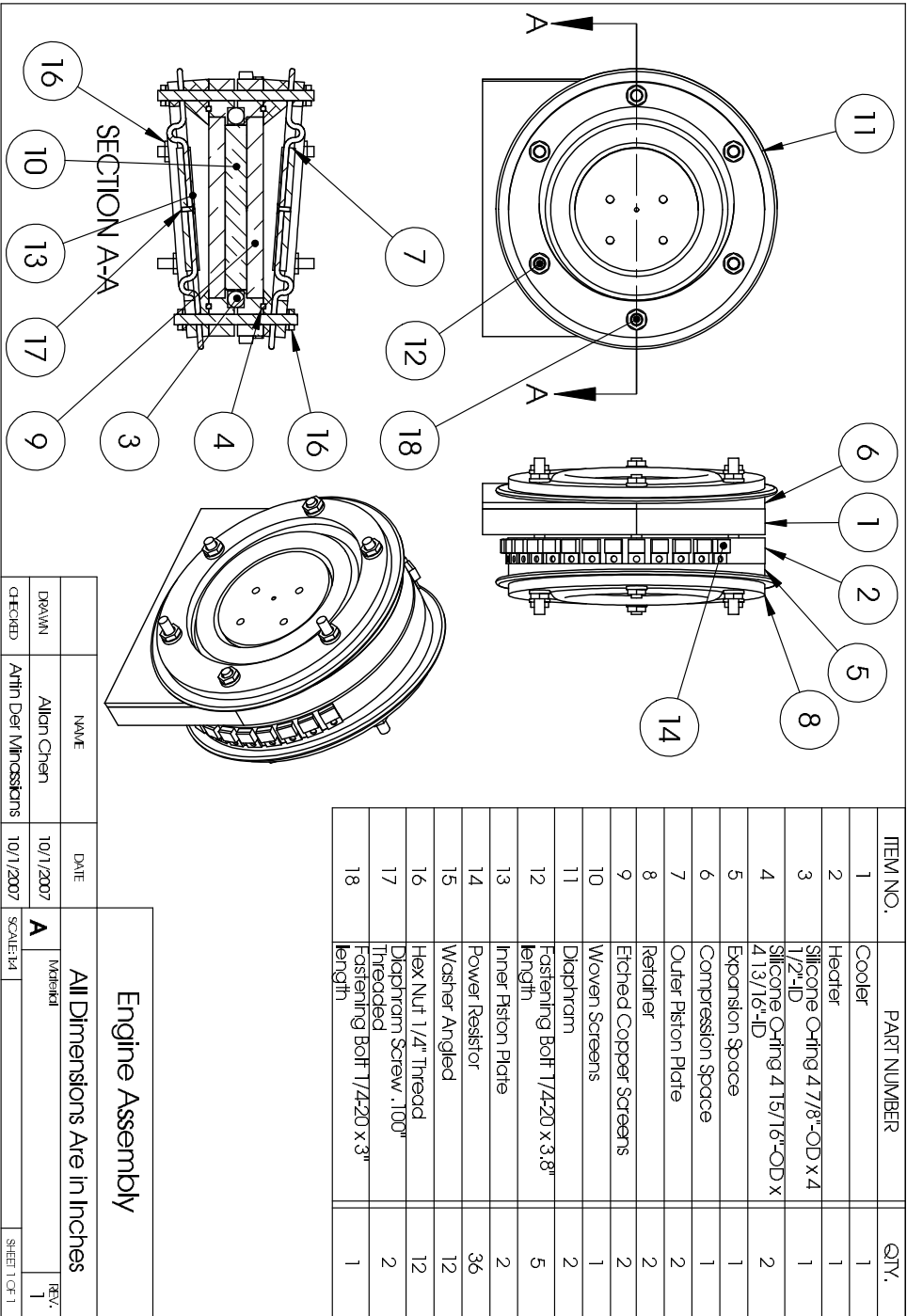


C-Core Assembly

All Dimensions Are in Inches

	NAME	DATE	SCALE:1:1	SHEET 1 OF 1
DRAWN	Allan Chen	10/11/2007	A	
CHECKED	Artin Der Missossians	10/11/2007		





NAME	Alian Chen
CHECKED	Antin Der Mitroshans

DATE	10/1/2007
SCALE	1:1

Engine Assembly

All Dimensions Are in Inches

REV. 1

ITEM NO.	PART NUMBER	QTY.
1	Base Plate	1
2	Flexure	3
3	Center Post	1
4	Socket Cap Screw 10-32 Threaded	6
5	C-Core Assembly	3

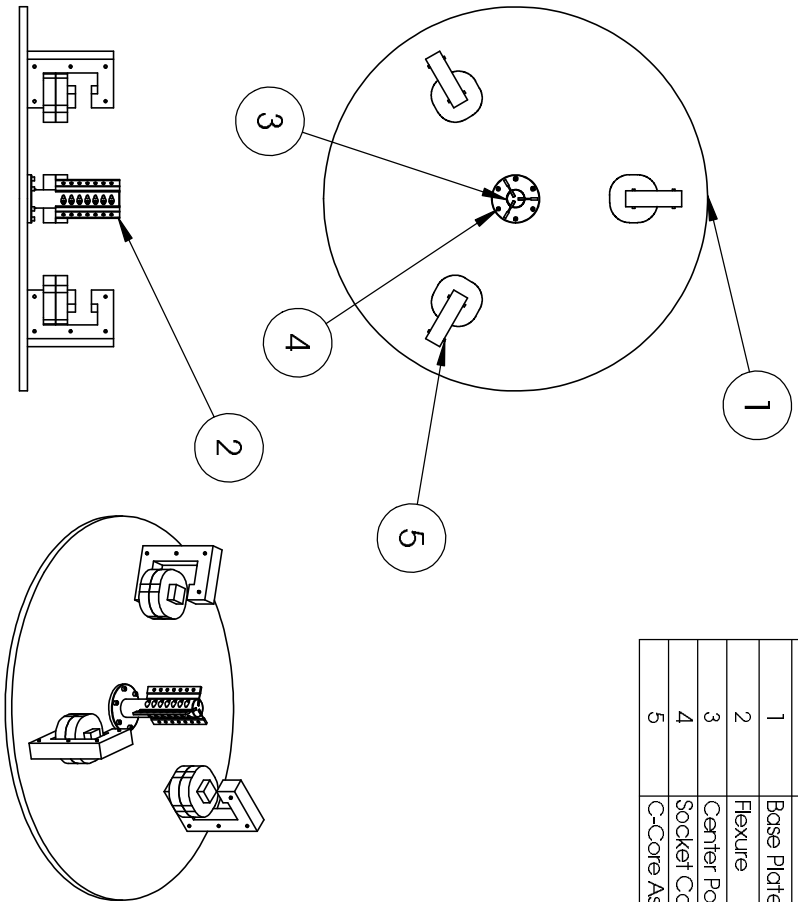
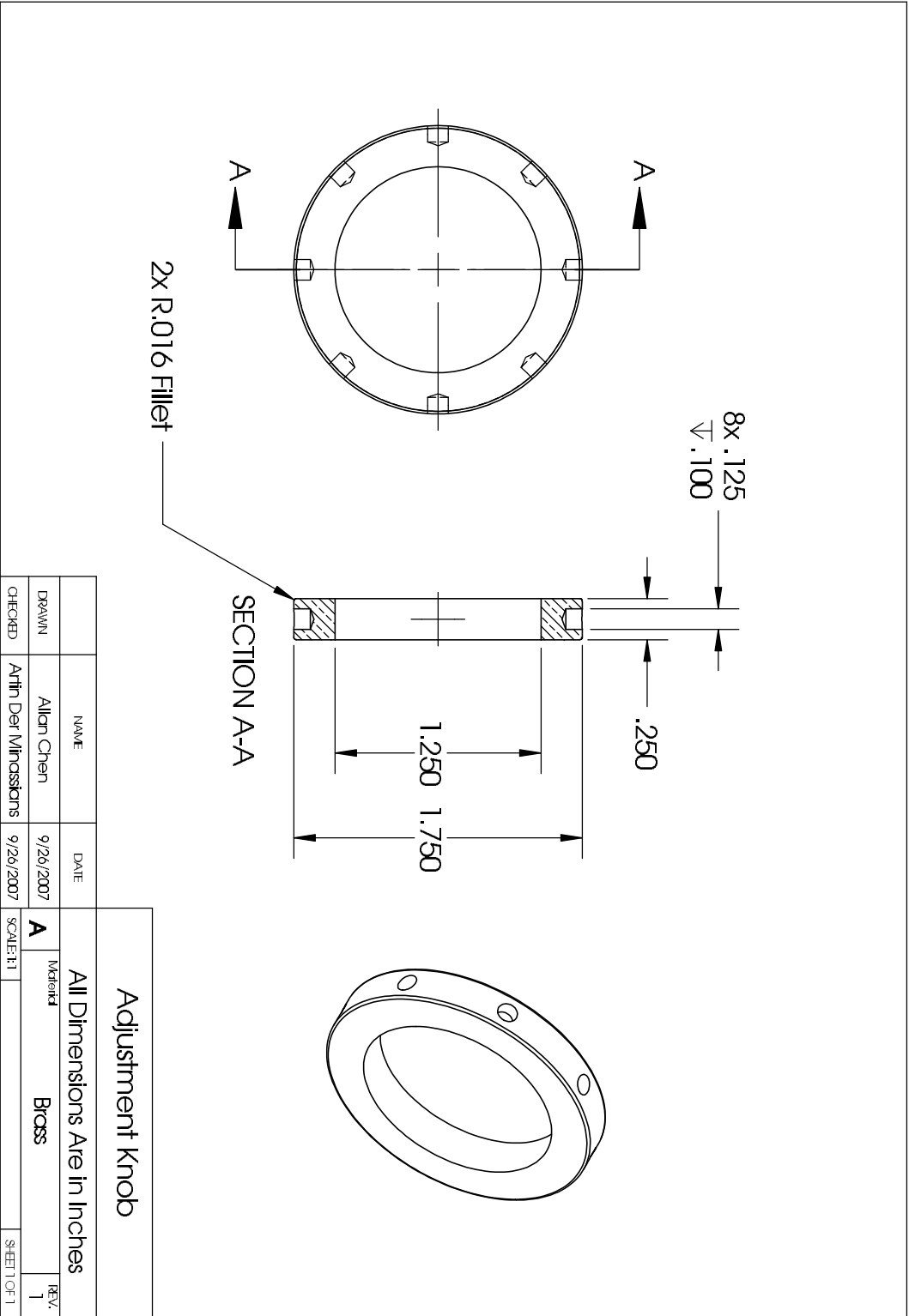
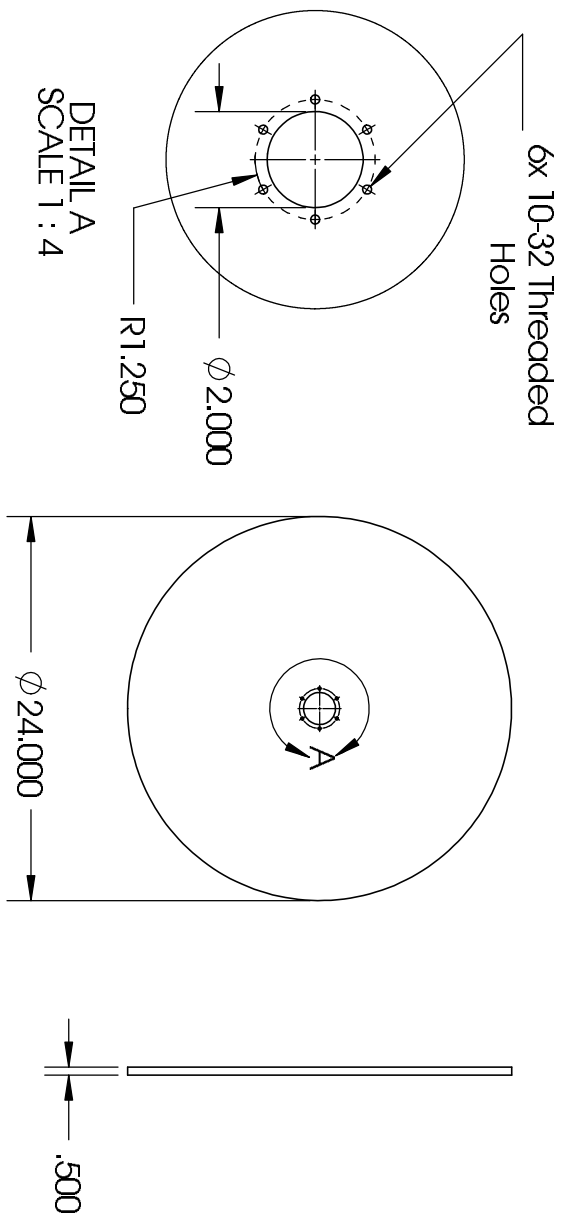


Plate Assembly

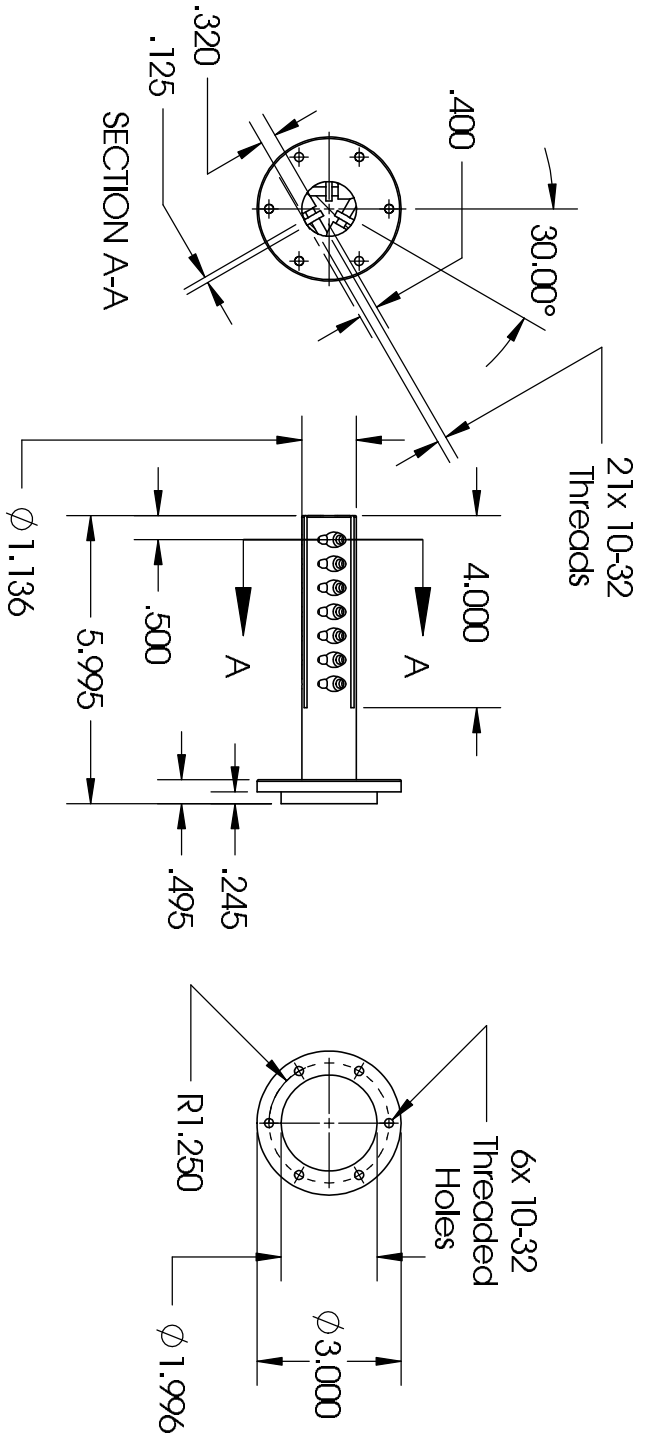
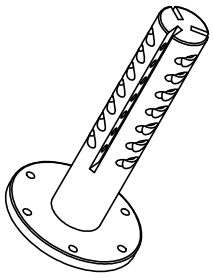
All Dimensions Are in Inches	
NAME	Allan Chen
DATE	10/11/2007
DRAWN	A
CHECKED	Artin Der Mirkossians
SCALE: 1:12	SHEET 1 OF 1





Base Plate

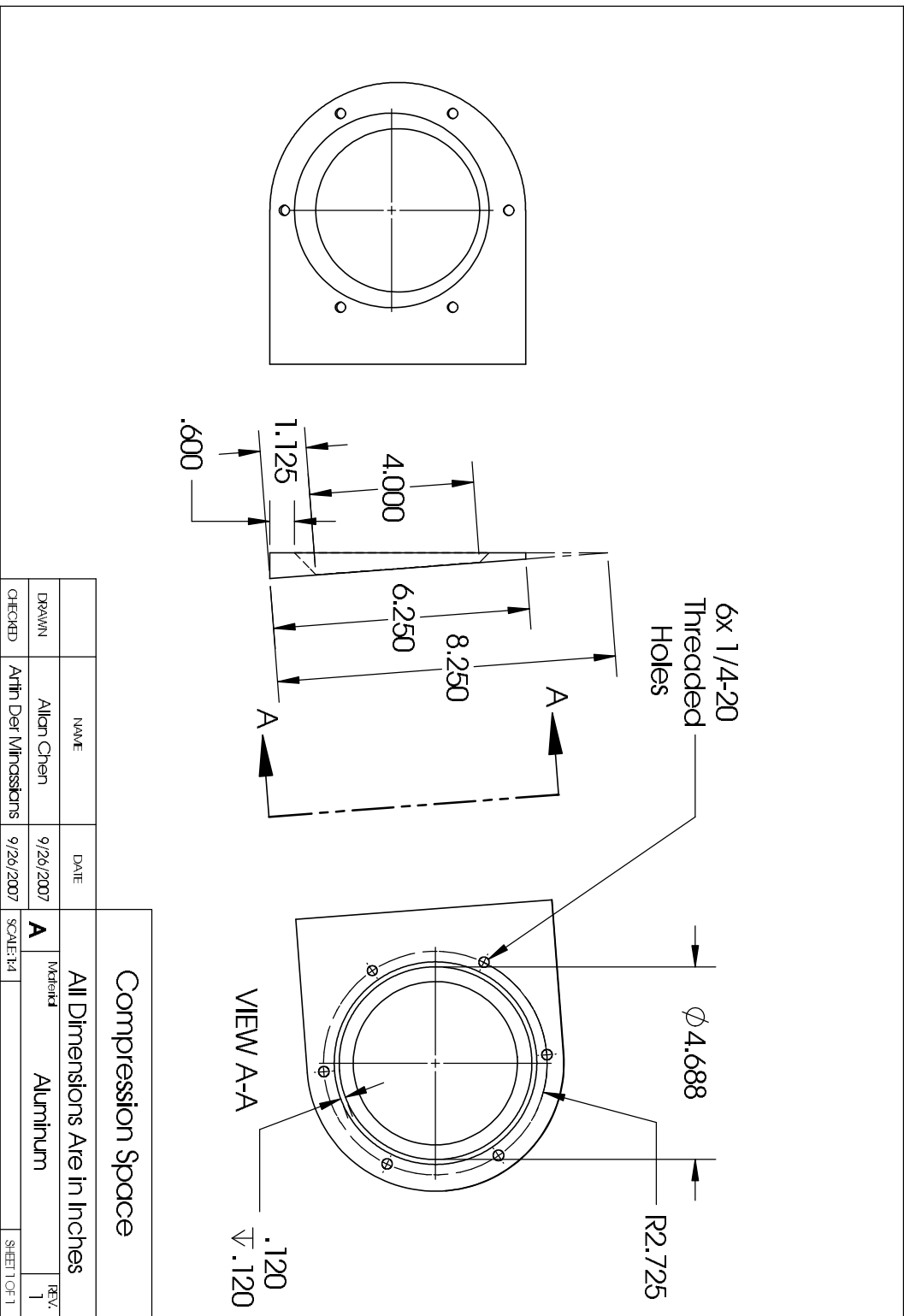
All Dimensions Are in Inches			
NAME	DATE	MATERIAL	REV.
Allan Chen	9/26/2007	Aluminum	1
CHECKED	Artin Der Mississians	SCALE: 1:12	SHEET OF 1

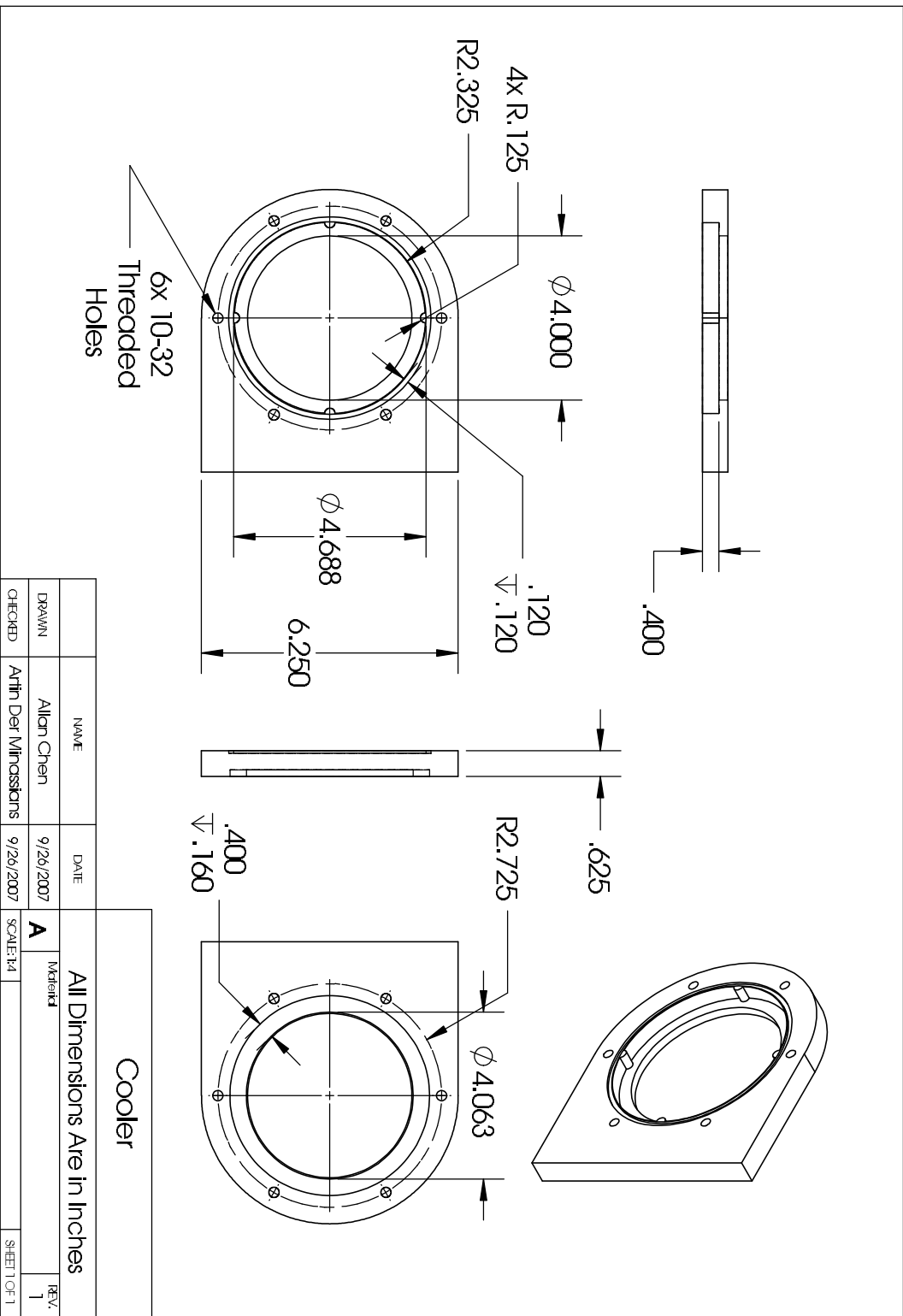


Center Post

All Dimensions Are in Inches

NAME	DATE	All Dimensions Are in Inches	
Allan Chen	9/26/2007	Material	Aluminum
Checked	9/26/2007	Scale: 1:1	REV. 1
Artin Der Missions			SHEET 1 OF 1

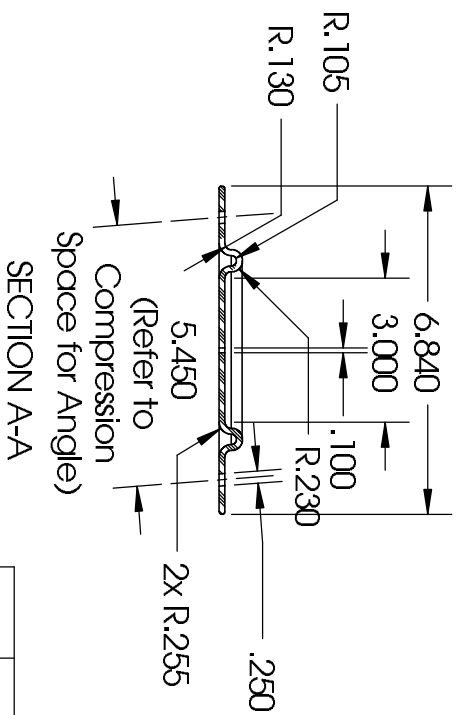
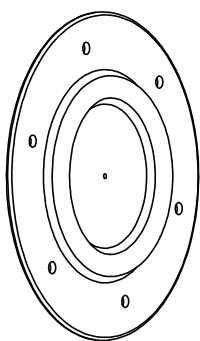
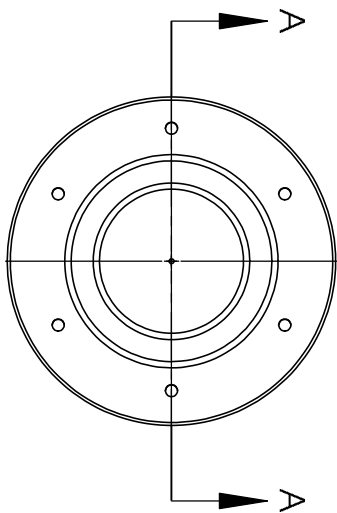




Cooler

All Dimensions Are in Inches

NAME	DATE	SCALE	SHEET
Alian Chen	9/26/2007	A	1
Artin Der Missions	9/26/2007	SCALE:1:1	1 OF 1

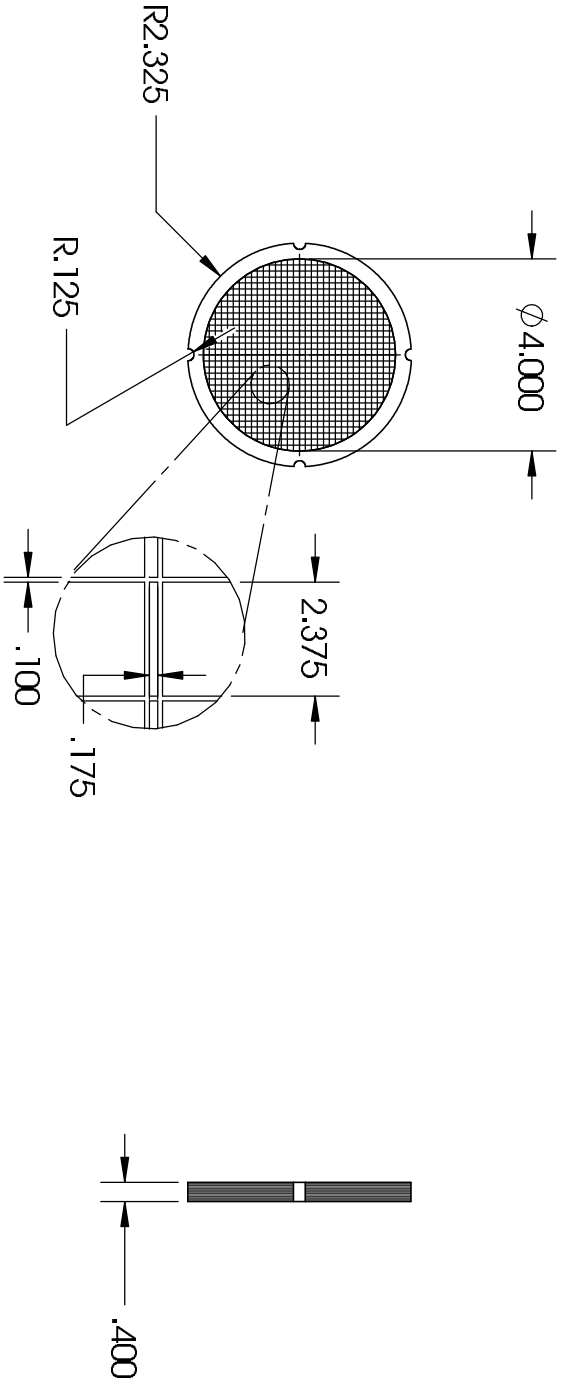


SECTION A-A

Diaphragm

All Dimensions Are in Inches

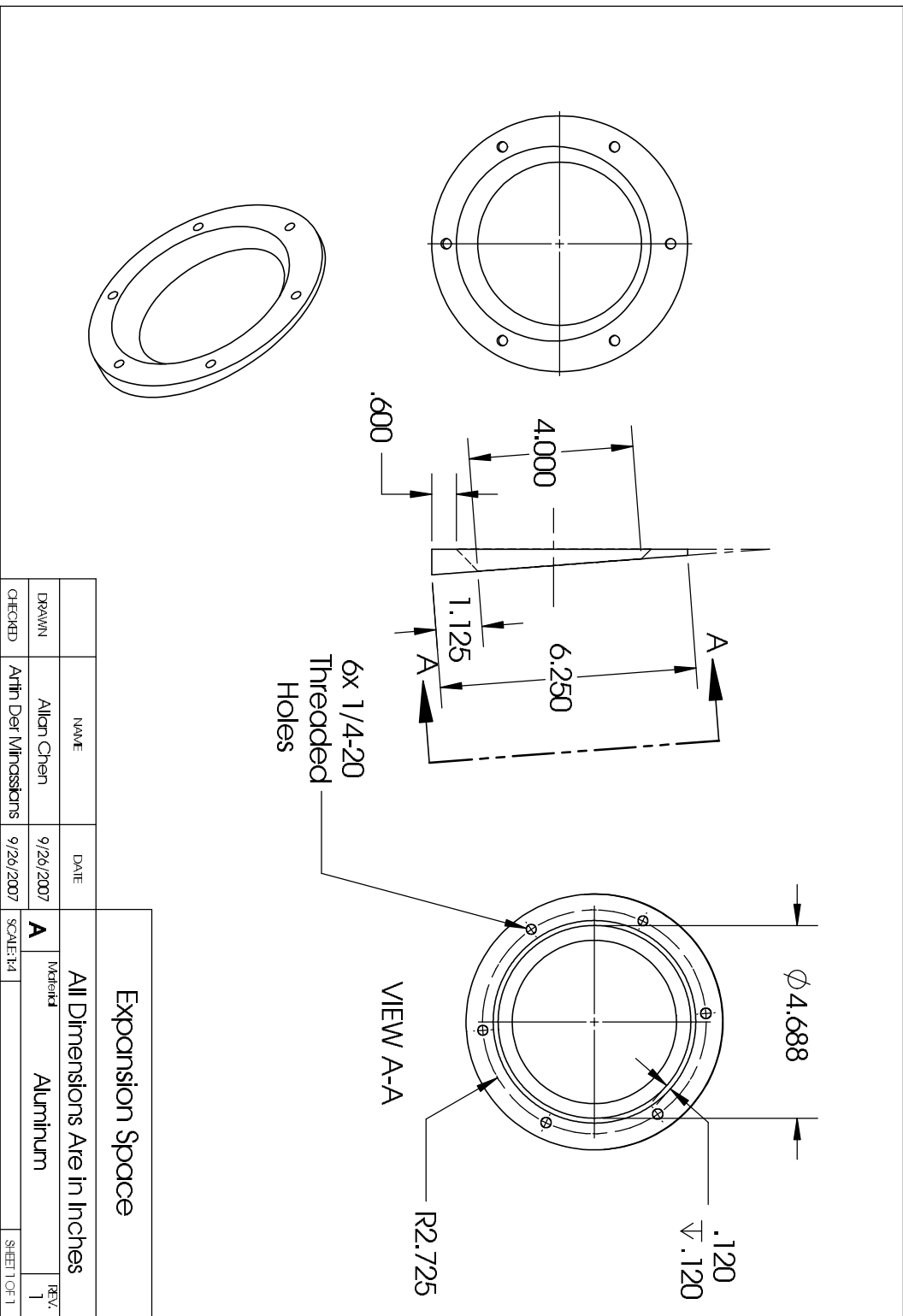
NAME	DATE	All Dimensions Are in Inches	
Alian Chen	9/26/2007	Material	REV.
Artin Der Missions	9/26/2007	Rubber/Polymer	1
CHECKED	SCALE: 1:1	SHEET 1 OF 1	

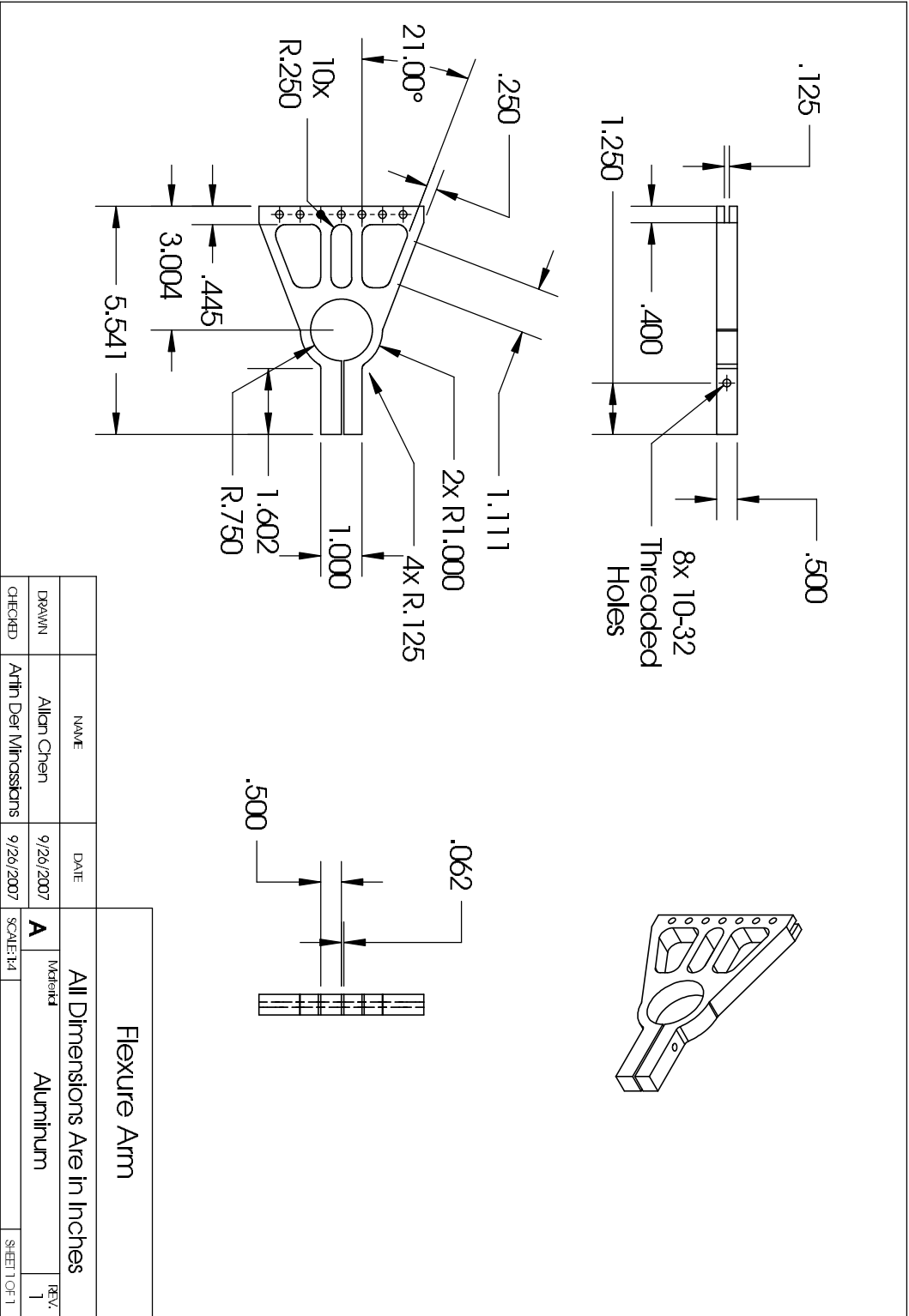


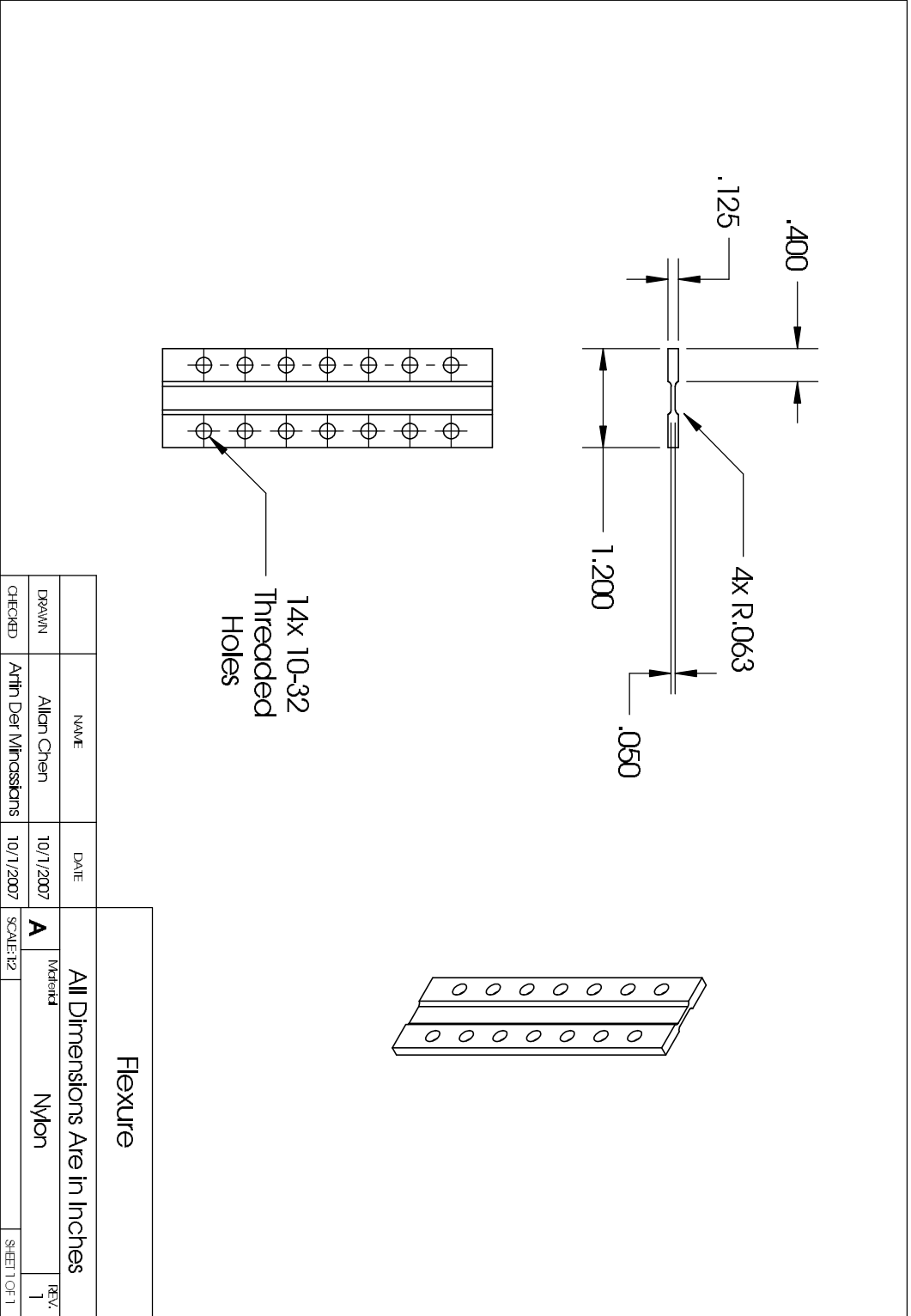
40 Sheets of 0.01 Thick Screens

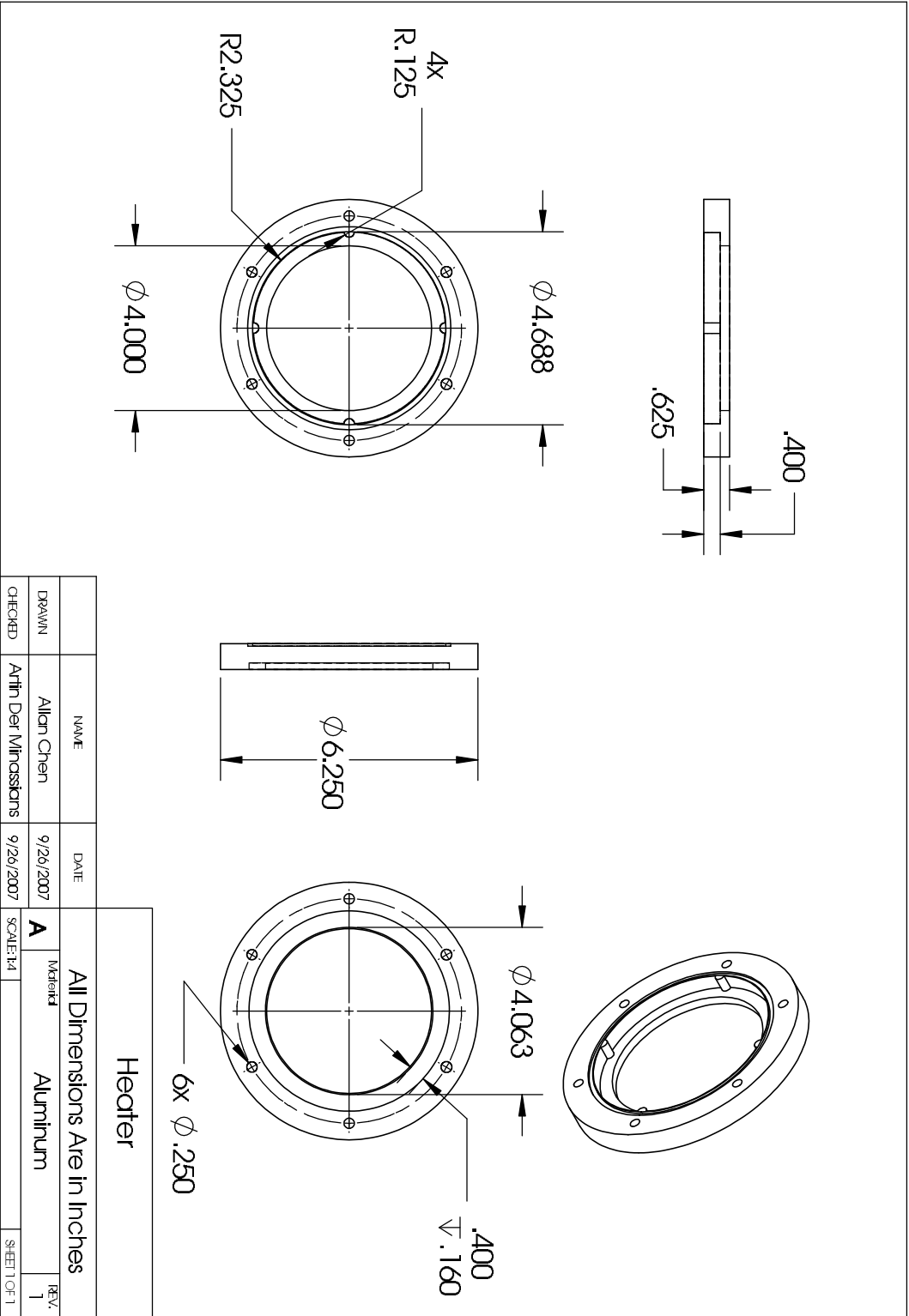
Note: Dimensions on detailed view is 10x the actual dimension.

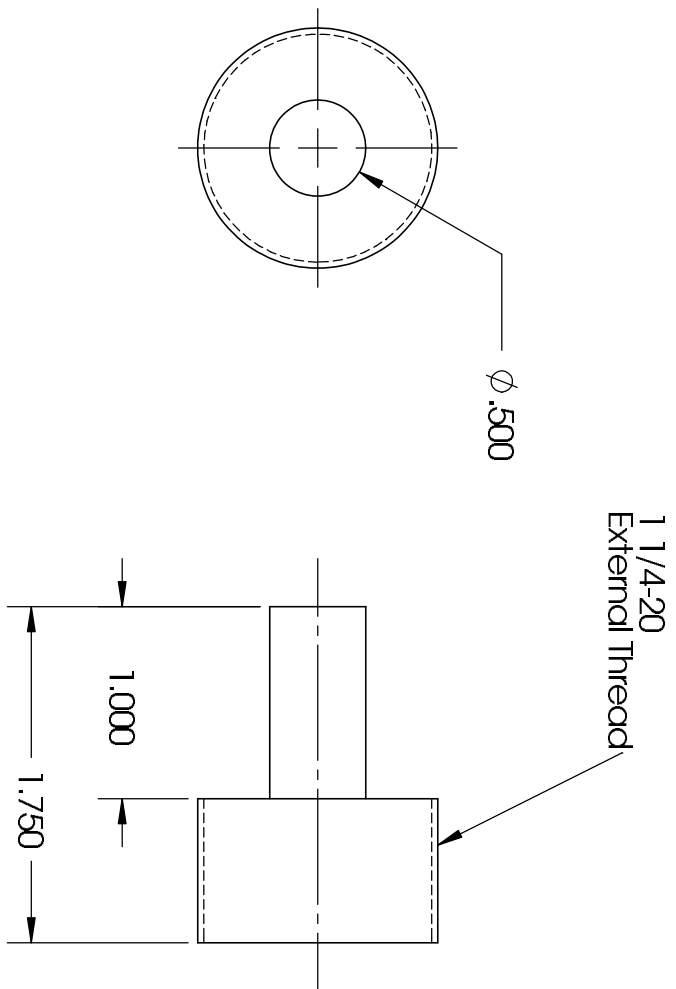
Etched Copper Screens		All Dimensions Are in Inches		REV.	
NAME	DATE	MATERIAL	SCALE: 1:1	1	
Allan Chen	10/11/2007	Copper			
DRAWN					
Artin Der Mississans	10/11/2007				
CHECKED					
				SHEET 1 OF 1	











Linkage Rod

All Dimensions Are in Inches			
NAME	DATE	MATERIAL	REV.
Allan Chen	9/26/2007	Aluminum	1
CHECKED	Artin Der Mississians	9/26/2007	SCALE: 1:1
			SHEET 1 OF 1